DYNAMICS, CONTROL, AND STABILITY OF FRUIT FLY FLIGHT

A Dissertation

Presented to the Faculty of the Graduate School

of Cornell University

in Partial Fulfillment of the Requirements for the Degree of

Doctor of Philosophy

by

Leif Gibbens Ristroph

May 2011

DYNAMICS, CONTROL, AND STABILITY OF FRUIT FLY FLIGHT

Leif Gibbens Ristroph, Ph.D.

Cornell University 2011

The flight of insects is a beautiful example of an organism's complex interaction with its physical environment. Consider, for example, a fly's evasive dodge of an approaching swatter. The insect must orchestrate a cascade of events that starts with the visual system perceiving information that is then processed and transmitted through neural circuits. Next, muscle actions are triggered that induce changes to the insect's wing motions, and these motions interact with fluid flows to generate aerodynamic forces. Though not as obvious to appreciate, simply flying straight and keeping upright require similarly complex events in order to overcome unexpected disturbances and suppress intrinsic instabilities. Here, I present recent progress in dissecting the many layers that comprise maneuvering and stabilization in the flight of the fruit fly, *D. melanogaster*. My emphasis is on aspects of flight at the interface of biology and physics, and I seek to understand how physical effects both constrain and simplify biological strategies.

This body of work roughly divides into three thrusts: the development of experimental and modeling methods, studies of actuation and control of maneuvering flight, and studies of control during flight stabilization. In Chapter 2, I discuss the experimental techniques we have developed for gathering many three-dimensional high-speed videos of insect flight. In addition, I outline our approach for automated extraction of body and wing motions from such videos. In Chapter 3, I show how experimental observations can be combined with aero-

dynamic models to reveal that fruit flies use paddling motions to drive forward flight. In Chapter 4, I review our work on turning maneuvers with an emphasis on how the wing motions themselves arise through an actuation mechanism. In Chapter 5, I outline a set of experimental and modeling techniques for understanding how insects recover from in-flight perturbations to their heading. In Chapter 6, I use a similar approach to analyze the intrinsic instability of body pitch and predict the reaction time needed to stabilize flight. In Chapter 7, I include work on the hydrodynamic interactions between flapping bodies in a fluid flow.

BIOGRAPHICAL SKETCH

Leif Ristroph was born on March 25, 1982 in Portland, Oregon to Robert M. Ristroph and Marie G. Ristroph. He is the sixth of eight children, and his siblings are Robert, Alice, Trygve, Einar, Ingrid, Gunnar, and Mickey. When Leif was a young child, the Ristroph family moved often, including stays in Casper, Wyoming and Picayune, Mississippi before settling in Pinehurst, Texas in 1988.

Leif embraces his place as one of the Ristrophs. He is number six. Leif is the son of Robert M. Ristroph, who taught him calculus at the park as well as how to bleed the brakes on a car. He is the son of Marie G. Ristroph, who nurtured his artistic side and handed down her persistence and optimism. As a brother, he is happy to count his siblings as his closest friends, so much so that they have developed common vocabulary and mannerisms that may be incomprehensible to others.

Leif attended public schools in Texas and graduated from Tomball High School in 2000. He then attended The University of Texas at Austin and graduated in 2005 with a Bachelor's of Science degree in physics. As part of his undergraduate work, Leif also studied abroad at Universität Würzbrg in Würzburg, Germany. Since, he has been a graduate student in physics at Cornell University in Ithaca, New York. In the summer of 2007, Leif was a visiting scholar to NYU's Courant Institute for Mathematical Sciences.

Over the years, Leif has had the pleasure of enjoying his studies and research, to the point that the word "work" does not feel appropriate. Outside of the classroom or laboratory, Leif might be found enjoying country music or sports, cooking or eating, or having coffee or beers with friends.

Dedicated to my father, Robert Michael Ristroph,
and in the memory of my mother, Marie Gibbens Ristroph.

ACKNOWLEDGEMENTS

Throughout the last five years, many people have helped me as I put together the work for this dissertation. I thank them all and recognize specific individuals below.

Itai Cohen, for being an optimistic and encouraging advisor and friend. Your enthusiasm provided the spark and kept these projects rolling along throughout. Also, thanks for letting me roam wild in my research at times and for reining me in at other times.

Jane Wang and John Guckenheimer, for their guidance and for providing the theoretical muscle in our collaboration. We have a special team here at Cornell, and I will try my best to emulate this in my future work.

Thanks to my other co-workers at Cornell who I have had the pleasure to work with: Umberto Pesavento, Gordon Berman, Attila Bergou, Sean Hackett, Sarah Iams, Song Chang, Acmae El Yacoubi, and Tsevi Beatus.

Special thanks to the undergraduates I have worked with: Witat Fakcharoenphal, Brad Lyon, Kirk Jensen, Katherine Coumes, Danqing Wang, Candy Reid, and Svetlana Morozova. I hope you all learned as much from me as I did from you.

Thanks to Professors Andy Ruina, Steve Strogatz, Ron Hoy, Jason Mezey, Andy Clark, Joe Fetcho, Cole Gilbert, Dan Ralph, Eric Siggia, Mike Dickinson, Kenny Breuer, Ty Hedrick, Tom Daniel, Bob Full, Robert Dudley, Mimi Koehl, and Noah Cowan. Our conversations steered me right for a number of projects and widened my perspective.

To the Cohen-heads: Mark Buckley, Sharon Gerbode, Rajesh Ganapathy, Jon McCoy, John Savage, John Mergo, Xiang Cheng, and Jesse Silverberg. Hanging out in and out of the lab provided the right mix of inspiration and relaxation.

To my undergraduate advisor, Harry Swinney, for taking me in during a tough time and setting me on the right path. And thanks to NYU's Jun Zhang, Mike Shelley, and Steve Childress for providing continuous inspiration.

To many friends I have run into over the last five years. Some that come to mind: Larsson Omberg, Johnny Gregoire, Matt Warkentin, Sharon Gerbode, Praveen Gowtham, Sumiran Pujari, Mark Buckley, Gordon Berman, Henrik van Lengerich, Seth Marvel, Tim Novikoff, Matt Farrar, Ravishankar Sundararaman, Attila Bergou, Hitesh Changlani, Ben Kreis, James Ledoux, John Savage, Ben Logsdon, Teis Schnipper, John Roberts, Saverio Spagnolie, Ben Smith, Robert Rodriguez, Lucas Koerner, and Stefan Baur.

Finally, thanks to my family and to Cécile Rey for their love and support.

TABLE OF CONTENTS

LIST OF TABLES

LIST OF FIGURES

CHAPTER 1

BACKGROUND AND OVERVIEW

1.1 Introduction

The flight of insects is a beautiful example of an organism's complex interaction with its physical environment. Consider, for example, a fly's evasive dodge of an approaching swatter. The insect must orchestrate a cascade of events that starts with the visual system perceiving information that is then processed and transmitted through neural circuits. Next, muscle actions are triggered that induce changes to the insect's wing motions, and these motions interact with fluid flows to generate aerodynamic forces. Though not as obvious to appreciate, simply flying straight requires similarly complex events in order to overcome unexpected disturbances and suppress intrinsic instabilities. Here, I present our recent progress in dissecting the many layers that comprise maneuvering and stabilization in the flight of the fruit fly, *D. melanogaster*. Our emphasis is on aspects of flight at the interface of biology and physics, and we seek to understand how physical effects both constrain and simplify biological strategies.

1.2 Is Flying Easy?

When searching for food, flies exhibit a stereotyped exploratory behavior in which straight flight paths are separated by rapid turns called *saccades* [12, 44]. Fruit flies turn when triggered by specific visual stimuli, and a typical saccade through 90° is completed in 50 milliseconds, or about 10 wing-beats. Given that

a blink of an eye is about 250 ms, these maneuvers are impressively fast. In reaching angular speeds of about 2000 °/s, these insects certainly out-perform what is capable in man-made aircraft. But is it difficult for a fly to perform a saccade?

Physically, one might address this question by comparing the torque needed to turn its body with the torque exerted simply to keep the body aloft. The turning torque is approximately $I\alpha \approx (10^{-13}\ \text{kg} \cdot\ \text{m}^2)(90°/(50\ \text{ms})^2) \approx 10^{-10}$ Nm. To hold its body weight up, the millimeter-scale wings must exert about $Mgr \approx (10^{-6}\ \text{kg})(10\ \text{m/s}^2)(1\ \text{mm}) \approx 10^{-8}$ Nm. This back-of-the-envelope calculation shows that remarkably weak torque is needed to turn, on the order of a few percent that needed to simply keep aloft. Counter-intuitively, even extreme flight maneuvers seem easy.

However, what appears to be effortless in terms of torque exertion is difficult in nearly all other respects. For example, the changes in wing motions needed to induce such a maneuver are also expected to be a few percent, which amounts to adjustments in wing orientation on the scale of a few degrees! What modulations to wing motions do insects make, and how small are these changes? Of course, such minuscule adjustments demand precise muscular actuation. How do muscle actions lead to subtle modulations of wing motions?

Further, the time-scales involved in such maneuvers are so fast that the turn is complete within the visual system reaction time [30]. How are these wing motions orchestrated if the insect is effectively blind during the maneuver?

Armed with knowledge of these force scales, one can now also appreciate the difficulty of simply maintaining straight flight. Air is a messy and unpredictable

environment, and small external torques will knock the insect off its intended path. In light of this, it seems that it is not difficult *to turn*, but rather it is difficult *to not turn*. How do fruit flies resist unwanted body rotations and keep on-course? What are the roles of sensory and neural systems in determining how flies respond to disturbances?

In this work, I take a tour through our investigations into some of these remarkable aspects of flight behavior of fruit flies. In the remainder of this opening chapter, I briefly review relevant areas of research related to the material in this thesis. Given the wide-ranging fields involved, I will largely summarize the current state of the field and point to specific papers that contain more thorough reviews of the literature. Below, I offer reviews of the experimental techniques and aerodynamic models and simulations used in understanding the wing motions, flows, and forces involved in insect flight. I then give summaries of the physical and biological aspects of flight control and stability in fruit flies. This background information will provide the context for the overview that ends the chapter.

1.3 Experimental Approaches

To the naked eye, as an insect darts through the air, its wings are only a blur. The curiosity of what's in that blur inspired the early investigations into insect flight. In fact, the French physiologist Étienne-Jules Marey invented high-speed cinematography in the mid-1800s in order to resolve the fast motions involved in animal locomotion [37]. In his studies of insect flight, Marey used high-speed cameras to capture the wing motions of insects under tethered conditions, that

is, held in place but free to beat their wings.

But it was not until 1956 that Jensen and Weis-Fogh performed the first serious study of insect flight with the express intent of understanding its aerodynamic basis [53, 52, 31]. They tethered locusts in a wind tunnel and used high-speed films to characterize the flapping wing motions. The goal was to see if conventional aerodynamic theory could account for the expected fluid forces generated, and the authors concluded that steady aerodynamics was indeed satisfactory.

Research in this tradition continued over the next several decades, with the work of Charlie Ellington serving as another hallmark. In 1984, Ellington published the results of an exhaustive study of the flapping motions of many freely-flying insects and suggested that there is some evidence to believe conventional aerodynamic theory may not work well for insect flight [16, 17, 18, 19, 20, 21]. The most recent study prior to the work presented here was that of Michael Dickinsons group [27, 28]. These authors examined turning and hovering flight in fruit flies using multiple high-speed video cameras, and suggested that much of the flight forces and torques could be estimated by conventional aerodynamic calculations.

The use of high-speed video continues to the present day, but this approach has generated precious few complete data sets that accurately describe the complete body and wing motions during free flight. Most data sets before 1980 correspond to tethered flight – see Weis-Fogh [52] and Vogel [48] as examples – and it is now clear that this restriction affects the wing kinematics employed. Most flight data also contain incomplete information due to limited number of camera views or inability to extract important parameters such as wing inclination

or angle of attack [54, 22].

Perhaps most importantly, we note that all studies prior to 2008 used manual motion tracking techniques to extract kinematic data from high-speed movies [27, 24, 29, 35, 49]. Manual tracking relies entirely on human input to get coordinate information and has uncharacterized errors. It also is tedious and slow, and the lack of automated methods for motion tracking has severely limited the number of data sets available.

Further, much of the insect flight investigations have been observational studies rather than true experiments. In such studies, insects simply fly as they wish and some aspects of flight behavior are recorded. In contrast to these observational studies, researchers interested in the visual system have examined the response of insects to moving patterns [47], but these insects were tethered and only a few aspects of the wing motions were measured [30]. Similarly, the response of insects to mechanical stimulation has been investigated by tethering insects within an arena that can rotate [11]. Fruit flies have been shown to exhibit stereotyped changes in wing motions in response to such rotations.

Unfortunately, I am not aware of a comprehensive review of experimental methods used insect flight studies. Two recent reviews seem to select topics of particular interest to the authors [32, 46]. Perhaps the best introduction to such methods can be found in Jane Wang's recent work [50], though experimental approaches are not the emphasis of this review.

Given that adjustments to wing motions are expected to be subtle, our experimental emphasis is on developing precision techniques for gathering large quantities of free flight data. In the following chapters, we present three exper-

imental advances needed to address flight maneuverability and stability. First, we show how to automate the high-speed video capture process in order to obtain many free-flight sequences. Second, we elicit specific behaviors by presenting insects with visual stimuli and by mechanically perturbing their flight. Third, we outline our algorithm for automatically extracting wing and body motion data from flight videos.

1.4 Flapping-Wing Aerodynamics

Historically, many insect flight studies have been motivated by the desire to understand whether the aerodynamic force generation mechanisms for flapping wings are fundamentally different from those of fixed wings. This question has good scientific grounding but, in the hands of the popular media, has become somewhat of an over-inflated ordeal. This is epitomized by the "bumblebees cannot fly" myth which purports that conventional aerodynamics does not account for sufficient force when applied to the insect wing. The myth appears to stem from a 1933 work by Magnan and Sainte-Laguë, though their calculations are at best order-of-magnitude estimates of the fluid forces [36]. Nonetheless, this motivation has driven seminal studies such as those of Jensen and Ellington, as mentioned above. Different studies have come out on different sides of the issue.

These early studies aimed at elucidating flapping-wing aerodynamic mechanisms likely came to different conclusions because of the many sources of error involved in animal experiments. However, the last 20 years has seen rapid progress in our understanding due to more refined approaches. The key ad-

vance in elucidating mechanisms of force generation has been to remove the insect either through dynamically-scaled flapping wing experiments or in computational flow simulations.

An experimental approach involves mechanized wings that allow one to prescribe flapping motions while measuring fluid forces and visualizing flow structures. In the 1970s, Bennett used a mechanized wing to show that rotation along its axis during translation could lead to elevated flight forces [6]. Dickinson and Goetz [13] and later Ellington *et al.* [23] used dynamically-scaled flapping wing experiments to reveal the influence of unconventional aerodynamic effects, and the most important effect involves the stable attachment of a vortex on the leading edge of the wing.

The novelty of the stable leading-edge vortex (LEV) is best appreciated by first considering the translation of a fixed wing, as in airplane flight [50]. At low angles of attack, a steady flow over the inclined wing leads to steady and predictable forces. At higher angles of attack, strong vorticity builds up on top of the wing and then sheds into the wake, leading to decreased forces and stall of the wing. For insect wings, which revolve about a root, the leading-edge vortex does not shed but remains attached even though angles of attack are quite large [23, 14, 9]. The stable LEV acts as a low-pressure region that elevates fluid forces. Though the attachment mechanism is not completely understood, it is clear that the stable LEV enhances forces for low-aspect ratio wings under revolution at insect-like Reynolds numbers [34].

Further, unsteady effects associated with wing rotation and wake interference can significantly influence aerodynamic forces. Both influences are clearly shown in the study of Dickinson *et al.* [14]. However, we note that the motions

used in these mechanical wing experiments appear to exaggerate the importance of the wings rotation about its long axis. Nonetheless, rotation during translation does enhance lift. Wing-wake interference is an inherently unsteady effect present when a wing reverses into its own wake. Unfortunately, there appears to be no clear consensus as to the degree of this influence for different wing motions. Certainly, wing-wake interference would appear to be more important for short amplitude motions [2].

Similar flow and force features have now been reproduced in computational fluid dynamics (CFD) simulations that also allow one to prescribe motions, measure forces, and visualize flows [40]. Interestingly, even 2D simulations of flapping wings seem to show good agreement with 3D mechanical wing experiments despite the apparent 3D nature of the stable LEV [51]. It may be that LEV stability due to wing revolution is not so crucial since the wings flip over before the vortex is shed anyway [50].

An interesting alternative to the mechanical wing experiments and simulations is to examine passive systems that nonetheless exhibit rich aerial behaviors. Falling paper provides an everyday example of unsteady aerodynamics [38, 4, 3]. By capturing video of the fluttering and tumbling dynamics of a descending plate, Pesavento et al. extracted the fluid forces and torques that must be acting on the plate without the need to measure forces directly. Falling plates have been used to reveal the importance of unconventional mechanisms such as rotational lift, and these data have been used to formulate a quasi-steady force model for complex motions at intermediate Reynolds numbers.

A quasi-steady model approximates the fluid forces in a form that depends only on the state variables for the wing, that is, its orientation, velocity, and

acceleration [16]. Thus, any history-dependence of the flow is lost in such an approximation. Flapping wing and falling paper experiments have revealed that such models capture stroke-averaged fluid forces to within about 10% [4, 42]. Despite the intermediate Reynolds numbers associated with insect flight ($Re = 10^1 - 10^4$), these studies indicate that the high Re law in which forces are quadratic in velocity serves as a good approximation.

Different quasi-steady models have been formulated by different groups, but all share a few essential ingredients [4, 42]. First, high Reynolds number lift and drag provide the largest contribution to the fluid forces. The models incorporate the effect of the LEV by simply increasing the lift and drag coefficients on the velocity-squared force laws. Thus, although the LEV stability is complex, its net effect is predictable and leads to increased forces. Second, the effect of added mass is included, which accounts for the acceleration of the mass of air near the wing. Third, the effect of wing rotation is modeled by adding a rotational lift term that is proportional to wing speed times rotation rate. For 3D motions, the blade-element approach is used: 2D forces are integrated along the length of the wing.

For recent reviews on the aerodynamics of insect flight, see those by Sane, Lehmann, and Wang [41, 33, 50].

Previous efforts from the Wang group have been devoted to the formulation of a quasi-steady model for the aerodynamics of flapping wings. Please see the dissertations of G. J. Berman and A. J. Bergou for further modeling details [8, 7]. The works reviewed here show that such models can be used to make general predictions that capture trends in maneuvering flight of actual insects.

1.5 Physical Aspects of Stability and Control

Since well before the Wright brothers, stability and control have been central issues in flight [1]. The stability of a physical system refers to its behavior near a point of equilibrium. For example, the damped pendulum is stable about its down position since it tends to return to that position when perturbed, while the inverted position is unstable. Stability can be evaluated by mathematical techniques if a description of the system can be formulated in terms of differential equations.

How do we define stability for insect flight? Physical stability refers to the tendency to return to a given flight state if wing motions remain fixed. Given that flapping flight is intrinsically unsteady, stability might be generalized to refer to a return to a periodic orbit that describes the body motion.

Alternatively, conventional stability can be analyzed if flight dynamics can be approximated by systems of differential equations. Recent works, including several of the papers comprising this thesis, have taken the first steps toward showing that reduced-order mathematical models capture much about insect flight dynamics and stability. These models average wing forces over each wing-beat and couple these forces to the body motion using the Newton-Euler equations of motion. Several groups are converging on this approach as a tractable route toward understanding insect flight.

Is insect flight intrinsically stable? Theoretical work indicates that, for some specific cases, flight is not stable. In particular, the works of Sun, Deng, and Humbert all suggest that different species of hovering insects possess an intrinsic instability in body pitch orientation [43, 25, 26, 10]. We present similar

findings for the fruit fly in our evaluation of the pitch stability.

Can we use actual insects to experimentally evaluate the intrinsic physical stability of flight? It seems unlikely. No quantitative stability experiment can be conducted, because insects have sensory-neural control loops that will surely lead to adjustments in the wing motions. Thus, animal experiments not only reflect physical stability or instability but also active control.

For insect flight, the physical essence of active control is how changes in wing motions lead to changes in flight forces. What types of changes have been observed in insects? Taylor's 2001 review summarizes these findings in an exhaustive search of the literature [45]. For fruit flies, it has been shown that many aspects of the wing motions are modulated, though most of these observations are qualitative, anecdotal, and have been witnessed under conditions of tethered flight. Zanker observed some free-flight wing modulations in fruit flies but was unable to measure the wing angles of attack [54]. The work of Fry *et al.* showed that flies modulate wing amplitude and stroke-plane angle [27], though the central results of this paper have since come under some question. In short, prior to the works presented here, there was precious little data on how fruit flies modulate wing motions during free-flight maneuvering or stabilization.

Our understanding of the stability and control of insect flight is progressing rapidly, and reviews that contain the most recent progress do not exist. For an introduction see Taylor's now-outdated 2001 review of some aspects of flight mechanics [45].

1.6 Biological Aspects of Stability and Control

Flight represents an extreme behavior that is accompanied by a host of interesting adaptations. Much research has focused on the muscular, anatomical, neural, and sensorial adaptations that determine how wings beat. Here, I review some of the highlights from these studies, and suggest how the framework of control theory can combine these biological aspects of stability and control with the physical ones described above.

The calculation that opens this chapter indicates that a tiny torque is needed to maneuver in comparison to that needed to stay aloft. The musculature of the fly reflects these different demands through a remarkable division of labor into large power muscles and fine control muscles [12, 15].

Power is supplied by two sets of large muscles that drive deformations of the thorax which in turn lead to the gross flapping motions of the wings. The muscle action communicates to the wing through an immensely complex hinge. The anatomy of the hinge has been somewhat mapped out, but at present there is no consensus on what are the relevant features that comprise the mechanism. We can only say that the hinge is a complex transmission system that transforms muscular inputs into wing motions.

Many groups of tiny "steering" muscles inject directly at the base of the wing and subtly modulate these motions. Thus, when probing wing modulations during maneuvering and stabilization, we are probably witnessing the action of these steering muscles.

At a deeper level, the fly uses sensory feedback to direct the muscles that

give rise to the wing motions. Vision in insects is well studied and dictates many fascinating flight behaviors [47]. In addition to a host of other sensory systems, the fruit fly possesses curious mechanosensory organs called halteres [39]. The halteres are a pair of tiny knob-shaped structures that are vestigial hind wings. In flight, halteres flap up and down at the same frequency as the wings. When the insect body is rotated, the motion of each haltere is altered, leading to strains at its base. The deformations are sensed and provide the fly with information about the rate of rotation of its body. Evidence from rotational experiments on tethered flies suggests that the halteres are fast-acting in comparison to vision [11].

In this work, we will show how these different levels of control and stability can be united using the framework of dynamical systems or control theory [5]. A central idea is that information flow can be organized as following a loop: sensors to neurons to muscles to hinge to wing motions to aerodynamic forces to body dynamics and back to sensors and so on. Our contribution will focus on applying ideas from dynamical systems to formulate mathematical models of maneuvering and stabilization of flight.

1.7 Overview

In this work, we take a tour through some of these remarkable aspects of flight behavior of fruit flies. We will analyze flight behavior at several levels and from the outside inward. First, we review our recent developments in techniques for motion tracking of flying insects. We then apply these tools to understanding how subtle adjustments to wing motions drive sideways, forward, and turn-

ing maneuvers. For turning flight, we touch on results that indicate how muscle action is communicated through the wing hinge biomechanics to generate wing motions. We then examine the fruit fly's "autostabilizer", a sensory-neural scheme that uses feedback to maintain body orientation during straight flight. Next, we show that insects' neural response times are tuned to handle a fast flight instability in body pitch orientation.

Additionally, we include a chapter on the fluid-mediated interactions between flapping flags. I conducted this project in the summer 2007 when I visited NYU's Courant Institute. This work is inspired by schooling of fish, and we use flapping flags as a model system to understand the interactions of flapping bodies in a flowing fluid.

Each of the following six chapters correspond to a paper that is published or will be submitted soon for publication. In the order of the chapters, these papers include:

- **L. Ristroph**, G. J. Berman, A. J. Bergou, Z. J. Wang, I. Cohen, *Automated hull reconstruction motion tracking (HRMT) applied to sideways maneuvers of free-flying insects*, Journal of Experimental Biology **212**:1324-1335 (2009).
- **L. Ristroph**, A. J. Bergou, J. Guckenheimer, Z. J. Wang, I. Cohen, *A paddling mode of forward flight in insects*, accepted for Physical Review Letters (2011).
- A. J. Bergou, **L. Ristroph**, J. Guckenheimer, Z. J. Wang, I. Cohen, *Fruit flies modulate passive wing pitching to generate in-flight turns*, Physical Review Letters **104**:148101 (2010).
- **L. Ristroph**, A. J. Bergou, G. Ristroph, K. Coumes, G. J. Berman, J. Guckenheimer, Z. J. Wang, I. Cohen, *Discovering the autostabilizer of fruit flies by*

inducing aerial stumbles, Proceedings of the National Academy of Sciences **107**:4820-4824 (2010).

- **L. Ristroph**, G. Ristroph, S. Morozova, A. J. Bergou, J. Guckenheimer, Z. J. Wang, I. Cohen, *Small, sleek, and in control: The body plan, neural control, and flight stability of insects*, to be submitted (2011).
- **L. Ristroph**, J. Zhang, *Anomalous hydrodynamic drafting of interacting flapping flags*, Physical Review Letters **101**:194502 (2008).

Additionally, in finishing up this thesis, I have written a review of insect flight dynamics and co-written a paper on the effect of center-of-mass location on flight stability:

- **L. Ristroph**, A. J. Bergou, G. J. Berman, J. Guckenheimer, Z. J. Wang, I. Cohen, *Dynamics, control, and stability of turning flight of fruit flies*, accepted for IMA Series (2011).
- S. Morozova, **L. Ristroph**, G. Ristroph, J. Guckenheimer, Z. J. Wang, I. Cohen, *Center-of-mass location and the stability of insect flight*, to be submitted (2011).

BIBLIOGRAPHY

[1] M. J. Abzug and E. E. Larrabee. *Airplane Stability and Control: A History of the Technologies That Made Aviation Possible*. Cambridge University Press, Cambridge UK, 2002.

[2] D. L. Altshuler, W. B. Dickson, J. T. Vance, S. P. Roberts, and M. H. Dickinson. Short-amplitude high-frequency wing strokes determine the aerodynamics of honeybee flight. *PNAS*, 102:18213–18218, 2005.

[3] A. Andersen, U. Pesavento, and Z. J. Wang. Analysis of transitions between fluttering and tumbling plates. *J. Fluid Mech.*, 541:91–104, 2005.

[4] A. Andersen, U. Pesavento, and Z. J. Wang. Unsteady aerodynamics of fluttering and tumbling plates. *J. Fluid Mech.*, 541:65–90, 2005.

[5] J. Bechhoefer. Feedback for physicists: A tutorial essay on control. *Rev. Mod. Phys.*, 77:783–836, 2005.

[6] L. Bennett. Insect flight: Lift and the rate of change of incidence. *Science*, 167:177–179, 1970.

[7] A. J. Bergou. *A quantitative analysis of wing pitching in insect flight*. PhD thesis, Cornell University, 2009.

[8] G. J. Berman. *Optimization, control, and flies: Quantitative studies of insect flight*. PhD thesis, Cornell University, 2009.

[9] J. Birch and M. H. Dickinson. Spanwise flow and the attachment of leading-edge vortices on insect wings. *Nature*, 412:729–733, 2001.

[10] X. Deng, L. Schenato, and S. S. Sastry. Flapping flight for biomimetic insects: part ii - flight control design. *IEEE Trans. Robotics*, 22:789–803, 2006.

[11] M. H. Dickinson. Haltere-mediated equilibrium reflexes of the fruit fly, drosophila melanogaster. *Phil. Trans. R. Soc. Lond. B*, 354:903–916, 1999.

[12] M. H. Dickinson. The initiation and control of rapid flight maneuvers in fruit flies. *Integr. Comp. Biol.*, 45:274–281, 2005.

[13] M. H. Dickinson, F.-O. Lehmann, and K. G. Goetz. The active control of wing rotation by drosophila. *J.Exp. Biol.*, 182:173–189, 1993.

[14] M. H. Dickinson, F.-O. Lehmann, and S. Sane. Wing rotation and the aerodynamic basis of insect flight. *Science*, 284:1954–1960, 1999.

[15] M. H. Dickinson and M. S. Tu. The function of dipteran flight muscle. *Comp. Biochem. Physiol. A*, 116:223–238, 1997.

[16] C. P. Ellington. The aerodynamics of hovering insect flight. i. the quasi-steady analysis. *Phil. Trans. R. Soc. Ser. B*, 305:1–15, 1984.

[17] C. P. Ellington. The aerodynamics of hovering insect flight. ii. morphological parameters. *Phil. Trans. R. Soc. Ser. B*, 305:17–40, 1984.

[18] C. P. Ellington. The aerodynamics of hovering insect flight. iii. kinematics. *Phil. Trans. R. Soc. Ser. B*, 305:41–78, 1984.

[19] C. P. Ellington. The aerodynamics of hovering insect flight. iv. aerodynamic mechanisms. *Phil. Trans. R. Soc. Ser. B*, 305:79–113, 1984.

[20] C. P. Ellington. The aerodynamics of hovering insect flight. v. a vortex theory. *Phil. Trans. R. Soc. Ser. B*, 305:115–144, 1984.

[21] C. P. Ellington. The aerodynamics of hovering insect flight. vi. lift and power requirements. *Phil. Trans. R. Soc. Ser. B*, 305:145–181, 1984.

[22] C. P. Ellington. Measuring the angle of attack of beating insect wings: robust three-dimensional reconstruction from two-dimensional images. *J. Exp. Biol.*, 200:2693–2704, 1997.

[23] C. P. Ellington, C. van den Berg, A. P. Willmott, and A. L. R. Thomas. Leading-edge vortices in insect flight. *Nature*, 384:626–630, 1996.

[24] A. R. Ennos. The kinematics and aerodynamics of the free flight of some diptera. *J. Exp. Biol.*, 142:49–85, 1989.

[25] I. Faruque and J. S. Humbert. Dipteran insect flight dynamics. part 1: Longitudinal motion about hover. *J. Theor. Biol.*, 264:538–552, 2010.

[26] I. Faruque and J. S. Humbert. Dipteran insect flight dynamics. part 2: Lateral-directional motion about hover. *J. Theor. Biol.*, 265:306–313, 2010.

[27] S. N. Fry, R. Sayaman, and M. H. Dickinson. The aerodynamics of free-flight maneuvers of drosophila. *Science*, 300:495–498, 2003.

[28] S. N. Fry, R. Sayaman, and M. H. Dickinson. The aerodynamics of hovering flight of drosophila. *J. Exp. Biol.*, 208:2303–2318, 2005.

[29] T. L. Hedrick and T. L. Daniel. Inverse problems in the flight control of the hawkmoth manduca sexta. *J. Exp. Biol.*, 209:3114–3130, 2006.

[30] M. Heisenberg and R. Wolf. The sensory-motor link in motion-dependent flight control of flies. In *Visual Motion and its Role in the Stabilization of Gaze*, pages 265–283, Amsterdam, 1993. Elsevier.

[31] M. Jensen. Biology and physics of locust flight. iii. the aerodynamics of locust flight. *Phil. Trans. R. Soc. Ser. B*, 239:511–552, 1956.

[32] G. V. Lauder and P. G. A. Madden. Advances in comparative physiology from high-speed imaging of animal and fluid motion. *Ann. Rev. Physiol.*, 70:143–163, 2008.

[33] F.-O. Lehmann. The mechanisms of lift enhancement in insect flight. *Naturwissenschaften*, 91:101–122, 2004.

[34] D. Lentink and M. H. Dickinson. Rotational accelerations stabilize leading edge vortices on revolving fly wings. *J. Exp. Biol.*, 212:2705–2719, 2009.

[35] Y. Liu and M. Sun. Wing kinematics measurement and aerodynamics of hovering droneflies. *J. Exp. Biol.*, 211:2014–2025, 2008.

[36] A. Magnan and A. Sainte-Lague. La vol au pointe fixe. *Actualities Sci. Ind.*, 60, 1933.

[37] E.-J. Marey. *Movement*. William Heinemann, London UK, 1895.

[38] U. Pesavento and Z. J. Wang. Falling paper: Navier-stokes solutions, model of fluid forces, and center of mass elevation. *Phys. Rev. Lett.*, 93:144501, 2004.

[39] J. W. S. Pringle. The gyroscopic mechanism of the halteres of diptera. *Phil. Trans. R. Soc. Lond. B*, 233:347–384, 1948.

[40] R. Ramamurtri and W. C. Sandberg. A three-dimensional computational study of the aerodynamic mechanisms of insect flight. *J. Exp. Biol.*, 205:1507–1518, 2002.

[41] S. P. Sane. The aerodynamics of insect flight. *J. Exp. Biol.*, 206:4191–4208, 2003.

[42] S. P. Sane and M. H. Dickinson. The aerodynamic effects of wing rotation and a revised quasi-steady model of flapping flight. *J. Exp. Biol.*, 205:1087–1096, 2002.

[43] M. Sun and Y. Xiong. Dynamic flight stability of a hovering bumblebee. *J. Exp. Biol.*, 208:447459, 2005.

[44] L. F. Tammero and M. H. Dickinson. The influence of visual landscape on the free flight behavior of the fruit fly drosophila melanogaster. *J. Exp. Biol.*, 205:327–343, 2002.

[45] G. K. Taylor. Mechanics and aerodynamics of insect flight control. *Biol. Rev.*, 76:449–471, 2001.

[46] G. K. Taylor, M. Bacic, R. J. Bomphrey, A. C. Carruthers, J. Gillies, S. M. Walker, and A. L. R. Thomas. New experimental approaches to the biology of flight control systems. *J. Exp. Biol.*, 211:258–266, 2008.

[47] G. K. Taylor and H. G. Krapp. Sensory systems and flight stability: What do insects measure and why? *Adv. Insect. Physiol.*, 34:231–316, 2007.

[48] S. Vogel. Flight in drosophila ii. variation in stroke parameters and wing contour. *J. Exp. Biol.*, 46:383–392, 1967.

[49] H. Wang, L. Zeng, H. Liu, and C. Yin. Measuring wing kinematics, flight trajectory and body attitude during forward flight and turning maneuvers in dragonflies. *J. Exp. Biol.*, 206:745–757, 2003.

[50] Z. J. Wang. Dissecting insect flight. *Annu. Rev. Fluid Mech.*, 37:183–210, 2005.

[51] Z. J. Wang, J. Birch, and M. H. Dickinson. Unsteady forces in hovering flight: computation vs experiments. *J. Exp. Biol.*, 207:449, 2004.

[52] T. Weis-Fogh. Biology and physics of locust flight. ii. flight performance of the desert locust (schistocerca gregaria). *Phil. Trans. R. Soc. Ser. B*, 239:459–510, 1956.

[53] T. Weis-Fogh and M. Jensen. Biology and physics of locust flight. i. basic principles of insect flight. a critical review. *Phil. Trans. R. Soc. Ser. B*, 239:415–458, 1956.

[54] J. M. Zanker and K. G. Goetz. The wingbeat of drosophila ii. dynamics. *Phil. Trans. R. Soc. Lond. B*, 327:19–44, 1990.

CHAPTER 2

AUTOMATED VIDEOGRAPHY AND HULL RECONSTRUCTION MOTION TRACKING

2.1 Summary

Flying insects perform aerial maneuvers through slight manipulations of their wing motions[1]. Because such manipulations in wing kinematics are subtle, a reliable method is needed to properly discern consistent kinematic strategies used by the insect from inconsistent variations and measurement error. Here, we introduce a novel automated method that accurately extracts full, three-dimensional body and wing kinematics from high-resolution films of free-flying insects. This method combines visual hull reconstruction of the insect, principal components analysis, and geometric information about the insect to recover time series data of positions and orientations. The technique has small, well-characterized errors of under 3 pixels for positions and 5 degrees for orientations. To show its utility, we apply this motion tracking to the flight of fruit flies, *D. melanogaster*. We find that fruit flies generate sideways forces during some maneuvers and that strong lateral acceleration is associated with differences between the left and right wing angle of attack. Remarkably, this asymmetry can be induced by simply altering the relative timing of flips between the right and left wings, and we observe that fruit flies employ timing differences as high as 10% of a wing beat period while accelerating sideways at 40% g.

[1]The work presented in this chapter is modified with permission from Ristroph *et al.*, *J. Exp. Biol.*, **212**, 1324-1335 (2009).

2.2 Introduction

The swimming of fish and the flight of insects are impressive feats of nature. These locomotor displays are the collective result of genetic, evolutionary, neurological, sensorial, and biomechanical influences and, when quantified, provide a window into the inner workings of these animals. Behavioral studies generally follow one of two approaches [24]. In the first, organisms are put in artificial environments and given a small number of choices in response to a stimulus, sacrificing richness of behavior for added experimental control. In the second, the animal is observed "in the wild", in which case a broad spectrum of behavior can be observed but not easily characterized due to limited measurement capabilities. For investigations of insect flight, this dichotomy is exemplified by studies of wing motions in tethered and wild insects. Tethered flight allows for detailed measurement of kinematics but does not allow for studying maneuvers. Studies of insects in the wild allow for studying complex behaviors but sacrifice control and measurement capabilities. Missing is an approach that would marry the beneficial aspects of these methods and would allow for recording of complex behaviors while giving full access to the locomotor metrics. Such an approach would significantly increase the range of behaviors that can be investigated quantitatively.

State-of-the-art approaches for capturing the motion of locomoting animals involve high-speed, three-dimensional videography combined with digitization of the captured sequences [18]. Most present techniques for extracting three-dimensional body and wing kinematics of flying animals rely on manual motion tracking. One approach involves positioning a computer model of an organism so that it overlays the image of the filmed organism [13, 14, 19]. Another method

requires tracking through time the position of representative marker features on the organism [17, 20, 29, 16, 26, 5, 23, 15]. Unfortunately, these techniques demand significant human input, resulting in poorly characterized or uncharacterized errors, limited throughput, and red-eyed researchers. More automated methods, similar to those developed for motion tracking of cockroaches and fish [22, 11], require development of morphologically-appropriate wing and body models when applied to flying animals [12]. Thus, there remains a need for accurate, automated, and versatile methods that do not require morphological inputs.

The study of insect flight in particular stands to benefit from high throughput and accurate tracking techniques. Asymmetries in flight kinematics appear to be quite subtle, even for wing motions that bring about extreme maneuvers. For instance, it has been reported that fruit flies execute rapid changes in yaw, or saccades, by inducing differences between the amplitude of the left and right wings of about 5 degrees and shifting the stroke plane by about 2 degrees [13]. Further exploration of the myriad maneuvers performed by insects will require large data sets that allow for identification of slight kinematic manipulations. In addition to addressing maneuverability, such data would offer insight into the roles of aerodynamics, efficiency, control, and stability in insect flight [27].

Here, we outline a novel approach to motion capture of flying insects. Rather than restricting the flight behavior, we film the rich free-flight repertoire of insects. This, by necessity, sacrifices much of our control over the maneuvers the insects perform. However, by automating our apparatus and recording many such events, we can identify common strategies used in similar maneuvers. Most importantly, our experimental arrangement is designed to yield films that

contain time-resolved, three-dimensional information about the motion of the insect body and wings during flight. In this work, we focus on a novel motion tracking technique we term Hull Reconstruction Motion Tracking (HRMT). We demonstrate that subtle, yet statistically-significant, differences in flight modes can be clearly discerned using this method. More specifically, we examine sideways flight of fruit flies, and show that the generation of lateral acceleration is associated with changes in the timing of the rapid flipping of the wings. Overall, this approach is a key step toward a quantitative description of the rich flight behavior of insects.

2.3 Materials and Methods

Generally, an analysis of insect flight requires a method for recording the flight events and a method for recovering the flight kinematics. Here, we describe techniques that allow for the automation of both high-speed videography and motion tracking.

2.3.1 High-speed, three-dimensional videography

We have assembled an automated, versatile system for capturing many video sequences of flying insects. The apparatus is composed of three high-speed cameras focused on a cubical filming volume contained within a large plexiglas flight chamber (Fig. 1A). The cameras are orthogonally-arranged using precision rails mounted on an optical table. We use Phantom v7.1 CMOS digital cameras (Vision Research, Wayne, New Jersey, USA) that are sensitive to visi-

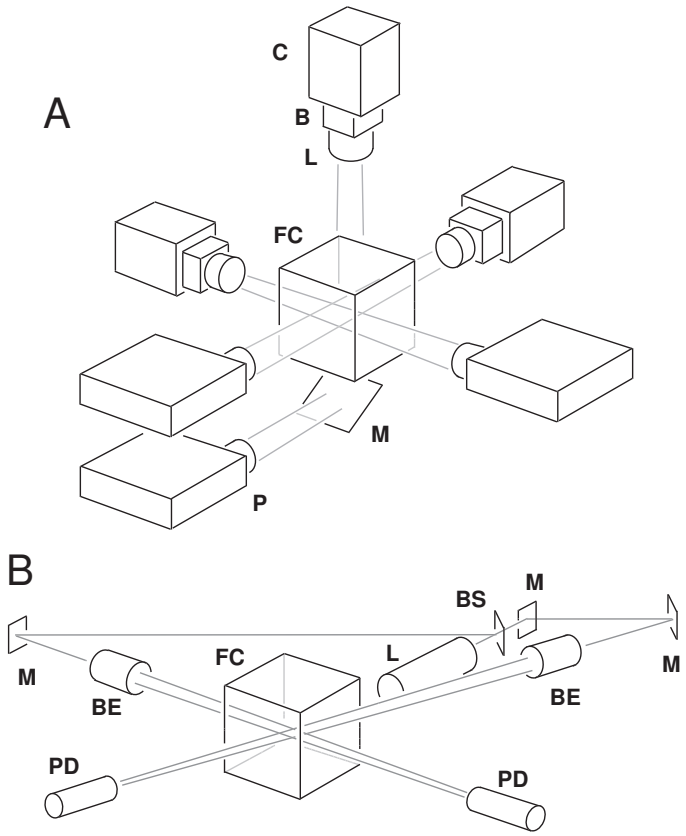

Figure 2.1: An experimental assembly for filming free-flying insects. (A) Three orthogonal cameras C aim toward a focal volume in a flight chamber FC, magnifying the image with bellows B and zoom lens L. Opposite each camera is a film slide projector P that illuminates the chamber. (B) The cameras are triggered to begin filming when crossed laser beams are broken by the flying insect. A laser L emits a beam that diverges at a beam-splitter BS and is re-routed by mirrors M to intersect through the flight chamber. Beam expanders BE inflate the beam to the size of the focal volume, and photodiodes PD detect the beam breakage. Simultaneous breakage of the beams initiates filming via a modified Schmitt trigger switching circuit (not shown).

ble light. We find that filming at 8,000 frames per second (fps) at a resolution of 512×512 pixels is a suitable compromise in temporal and spatial resolution. At this rate, we capture about 30-35 wing orientations per wing-stroke of the fruit fly (*D. melanogaster*), which beats its wings approximately 250 times per second. The cameras are event-triggered, as described below, and are synchronized electronically. In our experiments, the cameras automatically save the

images on an internal memory buffer. Once a recording sequence is finished, the cameras dump the images onto an external computer hard drive and then become available for recording more flight events.

Because fruit flies are small, measuring about 3 mm in body length, we magnify with an optical bellows (Nikon PB-5, Nikon USA, Melville, New York, USA) and a zoom lens (Nikon Macro-Nikkor, 28-105 mm) attached to each camera, as shown in Fig. 1A. The bellows can be expanded or contracted to achieve varying magnification and thus accommodate different-sized filming volumes. For *D. melanogaster*, typical cubical volumes described in this paper measure 1.5 cm in side length. This filming arrangement insures that perspective distortion between the near and far portions of the chamber is less than 5%.

Achieving crisp images of fruit flies in flight requires short exposure times ($< 30\mu$s), high magnification, and large depth-of-field (high f-stop values). These requirements all reduce the light available for filming. To avoid heating the filming volume, we use three slide projectors (Kodak Ektagraphic series, Kodak, Rochester, New York, USA) that provide infrared-filtered intense white light. Each lamp is directed toward its opposing camera, as in Fig. 1A. Thus, our films consist of silhouettes or shadows of the flying insect (Fig. 2A).

2.3.2 Variable sensitivity event-triggering

When released in the flight chamber, flies rarely enter the filming volume, which corresponds to only 0.05% of the chamber. To capture films only when a fly is in the volume, we assembled an optical detection system [21, 8, 9]. A schematic of this system is shown in Fig. 1B. A laser (red HeNe, Thorlabs, Newton, New

Jersey, USA) emits a 2 mm-diameter beam that is split and re-routed to intersect the filming volume through the sides of the flight chamber. Each beam passes through a Galilean expander, crosses the filming volume, and impinges on a photodiode. The photodiodes are connected to a custom-made switching circuit that signals to the cameras when both beams are simultaneously intercepted. This triggers the cameras to initiate recording.

The beam expanders in our assembly allow us to match the triggering volume to the filming volume, thereby maximizing the number of captured flight sequences. This versatility also accommodates filming of insects of varying sizes. We generally expand the beam to 1-2 cm in diameter. Since the fly body area is on the order of 2 mm^2, our circuit is designed to reliably trigger on beam intensity disturbances of only a few percent.

In a typical experiment, we release between one and 20 flies in the filming chamber. When interested in flight statistics, we release up to 20 flies and film for up to three hours. In these experiments we obtain up to 10 events per hour. The flight chamber measures 13 cm on each side, so the flies are more than 20 body lengths from the nearest wall, indicating that the walls have negligible influence on the aerodynamics.

2.3.3 Automated tracking of flight kinematics

In order to analyze the vast amounts of data collected with our apparatus, we have developed a method for automatically extracting the wing and body positions from flight films. This method is accurate, fast, model-independent, and broadly applicable. Our tracking algorithm neatly divides into four steps: im-

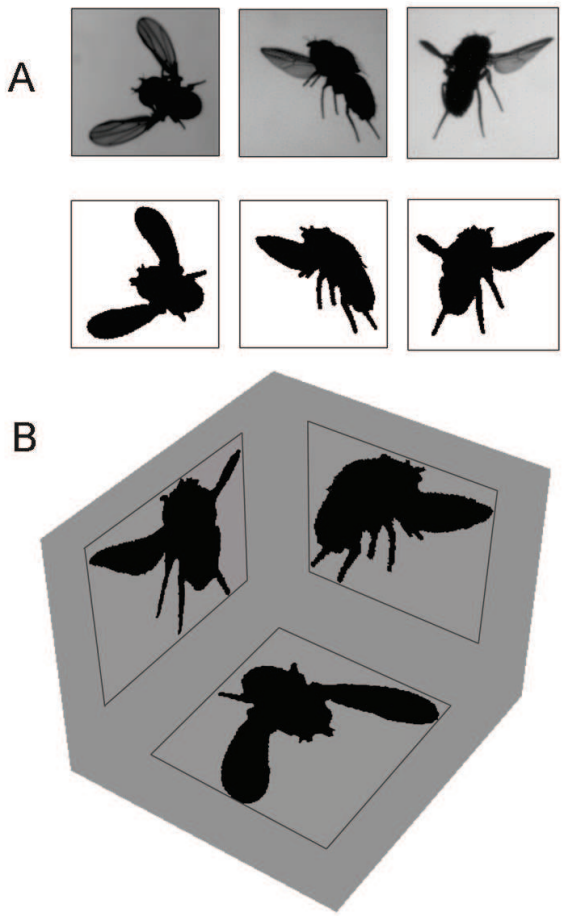

Figure 2.2: Aligned silhouettes are rendered by image processing and registration. (A) The three orthogonal cameras provide images of a fruit fly in flight (top). To obtain silhouettes from these raw images, a background picture is subtracted and the resulting image is thresholded (bottom). (B) Because the cameras are not perfectly aligned, the pixel coordinates in different views may not correspond to the same spatial coordinate. In order to register the images, we form a minimal bounding rectangle around the shadow in each view and then shift and scale the images such that the rectangle corners are consistent between views.

age processing and registration, hull reconstruction, "dissection" of the hull reconstruction into a body and two wings, and extraction of positions and orientations. We implement all stages using custom-written MATLAB code that is available as supplementary material.

Our hull reconstruction method requires crisp silhouettes of the flies and accurate registration of the pixels in the images. To achieve registration, we first precisely align the cameras by fine adjustment of translation stage mounts. This procedure positions the center of each camera view to within a few pixels of a common point in space and also establishes the global, orthogonal coordinate system employed throughout this work. The procedure achieves equal magnification to better than 1%, as measured by imaging a ruled microscope slide that also determines the pixel-to-distance conversion. Next, we use the images from each flight movie itself to more precisely adjust the alignment and magnification. To obtain image silhouettes, we first subtract a background image from each picture. The resulting image is thresholded so that the insect shadow appears black on an otherwise white background (Fig. 2A, bottom). In order to calibrate the pixels so that their coordinates are aligned and properly scaled, we use a registration algorithm. We first enclose the silhouette from each view in the minimal bounding rectangle (Fig. 2B). We then scale and translate the images so that the pixel coordinates of the bounding rectangle corners match. For example, to register the pixels along the vertical direction, we shift and scale images from one of the horizontal cameras such that its vertical coordinate is consistent with images from the second, reference horizontal camera. We vertically shift the image from the first view such that the top of its bounding rectangle has the same vertical coordinate value as that of the reference view. Then, we scale the image from the first view such that the bottom of its bounding rectangle has the same vertical coordinate as that of the reference view. The same procedure is used to register the other image coordinates. Typically we find that the images need to be scaled by less than 1% and shifted by about 5 pixels to achieve registration. To insure consistent registration for each movie, we find

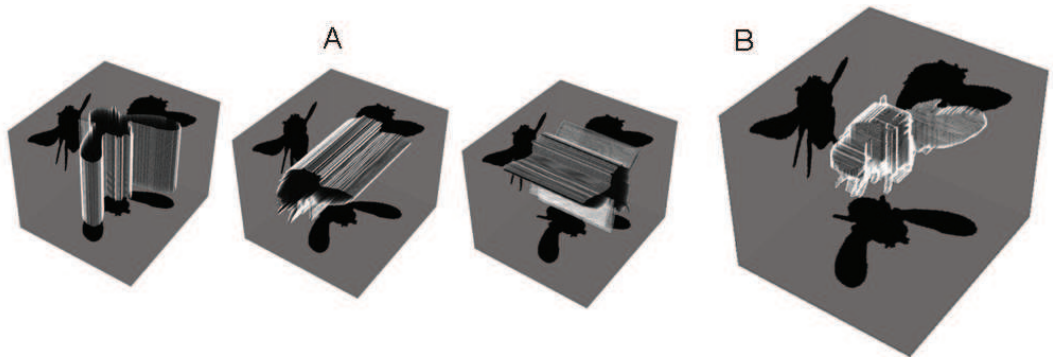

Figure 2.3: Visual hull reconstruction forms a 3D shape that is consistent with the three silhouettes. Our implementation seeks 3D volume pixels, voxels, that project onto the silhouette in each view. Hull reconstruction is equivalent to the exercise of first forming extended 3D shadows from the silhouettes (A), and then finding the intersection in space of these extended shadows (B). The resulting object is the visual hull of the insect, the largest volume shape that is consistent with the three silhouettes. The hull data consists of an array of voxel coordinates.

the average shift and scale values for the entire image sequence and apply these values to all images. The resulting thresholded and registered image sequences are fed into the hull reconstruction algorithm.

In the context of our experiments, the method of visual hull reconstruction [1] entails using the three sets of 2D silhouettes to construct a 3D shape. Specifically, our algorithm identifies volume pixels, or voxels, in 3D whose 2D projections map onto black pixels in all three images. More intuitively, this procedure is equivalent to the geometric exercise of placing the images on three adjacent sides of a rectangular prism and extending each shadow in a direction perpendicular to the image (Fig. 3A). Here, simple extension of each shadow is justified by the rather small perspective distortion. In this scenario, the hull volume corresponds to the intersection of the 3D extended shadows. An example of the resulting shape is shown Fig. 3B. This collection of voxels forms a convex volume that envelops the 3D shape corresponding to the real insect. We show that,

by using three cameras to image the insect, we obtain a visual hull that is sufficiently close in shape to the real insect so that wing and body positions and orientations can be extracted.

To identify the hull, the reconstruction algorithm must systematically scan through and analyze voxels in the filming volume. For typical images, the bounding rectangle side length is only one-fifth of the image side length. Consequently, this procedure is sped up one hundred fold by only considering voxels corresponding to pixels located within the bounding rectangles [4]. In addition, we find that a coarse-graining optimization leads to an additional factor of four reduction in the run time [4] while maintaining accurate coordinate extraction, as assessed in the next section. This procedure entails grouping sets of eight unit voxels into coarse-grained voxels each of size 2 pixels $\times$ 2 pixels $\times$ 2 pixels. A subsampling routine is used to determine whether the coarse-grained voxel should be included in the hull. Two of the eight voxels are randomly picked and analyzed to determine whether their projections are contained within all three shadows. If both sampled voxels correspond to shadows, the coarse-grained voxel is included in the hull. The final output of these procedures is a collection of coordinates specifying the coarse-grained voxels that are part of the visual hull (Fig. 3B). We find that using MATLAB on a desktop computer, our implementation of this algorithm rapidly constructs a 3D hull (see supplementary code).

Portions of the hull that correspond to the body, right wing, and left wing form well-defined groups of voxels. To collect voxels that are near one another, we use a k-means clustering algorithm with a Euclidean distance metric (MATLAB). We find that identifying four clusters ($k = 4$) neatly isolates two separate

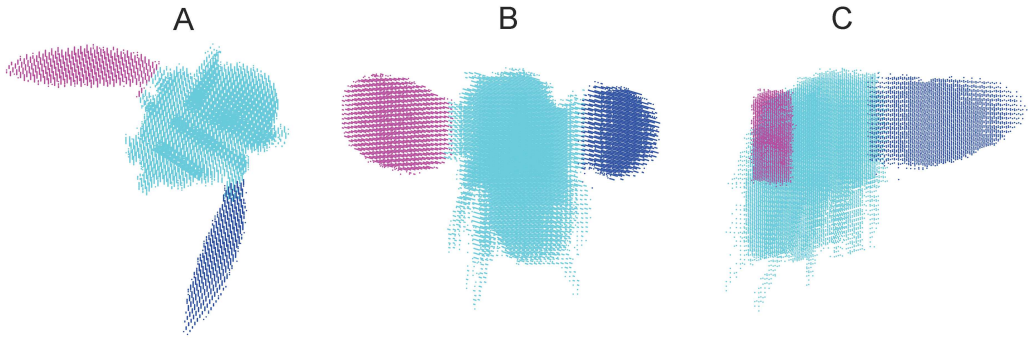

Figure 2.4: The body, right wing, and left wing of the insect are identified by applying a clustering algorithm. The top view, (A), and two side views, (B) and (C), show that the right (red) and left (dark blue) wings are well distinguished from the body (light blue).

groups of voxels corresponding to the left and right wings and two additional larger groups of voxels that correspond to the anterior and posterior of the insect body. These two larger clusters are merged to identify all the voxels corresponding to the body, and the smaller clusters correspond to the wings. In Fig. 4, the wing voxels are shown slightly separated from the body voxels in order to illustrate how well these groupings are identified.

From these voxel groupings, we recover the positions and orientations of the body and wings using a combination of centroid determination, principal components analysis (PCA), and geometric information about the insects. The centroids of the body, right wing, and left wing correspond to the mean of the voxel coordinates in each grouping. PCA finds each voxel grouping orientation by determining the principal axis of the moment of inertia (MATLAB). Performing PCA on the body voxels, we extract the principal body axis vector, $\hat{A}$, that identifies the Euler angles for the body pitch, β, and yaw, ψ (Fig. 5A). To determine the third Euler angle for the body roll, ρ, we perform a second round of clustering on the body voxels with $k = 3$ and find three clusters, corresponding to the head, thorax, and abdomen (Fig. 5B). The centroids for these clusters con-

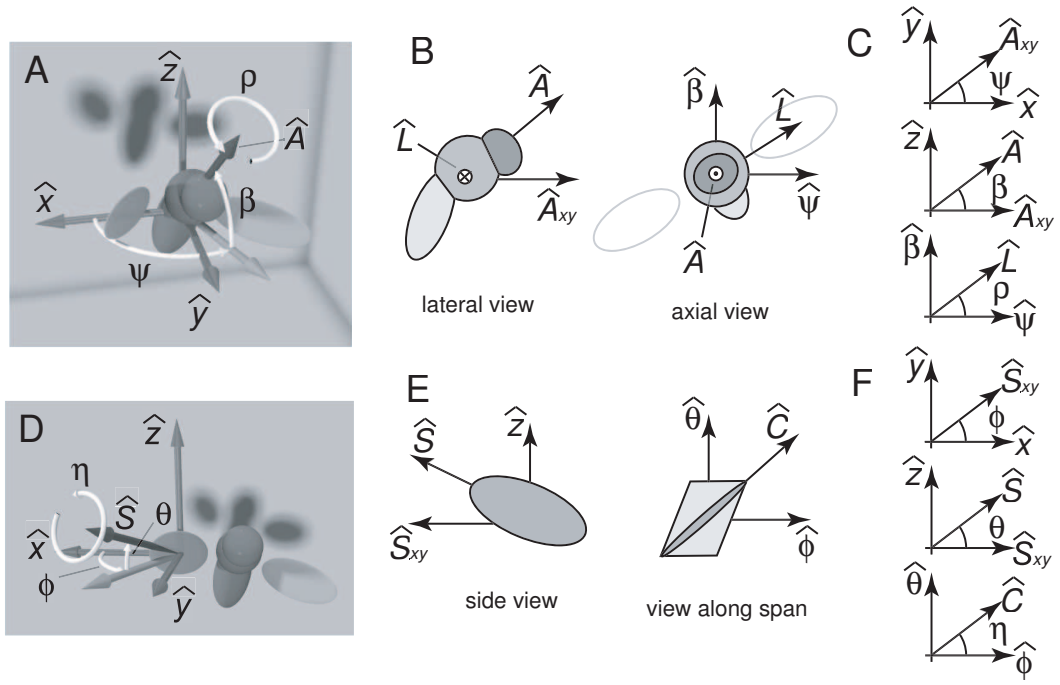

Figure 2.5: The positions and orientations are extracted for each the body, right wing, and left wing. The centroid is defined to be the mean of the voxel coordinates for each respective grouping. (A) and (B) To identify the three Euler angles of the body, we define two vectors on the body. The first is the axial unit vector, $\hat{A}$, which is found by applying principal components analysis (PCA) to the body voxel coordinates and gives the yaw angle, ψ, and the pitch angle, β. The second is the lateral unit vector, $\hat{L}$, that runs from the insect's right to left and is identified as the normal to the plane formed by the centroids of the head, thorax, and abdomen clusters. (C) The roll angle, ρ, is the angle between $\hat{L}$ and the unit yaw vector, $\hat{\psi}$. (D) For each wing, the span vector, $\hat{S}$, is identified by PCA and gives the stroke angle, ϕ, and the stroke deviation angle, θ. (E) The chord vector, $\hat{C}$, is parallel to the longest diagonal of the parallelogram cross-section of the wing hull. (F) The wing pitch, η, is the angle between $\hat{C}$ and unit stroke vector, $\hat{\phi}$. We note that this choice body and wing orientation angles are similar to conventional spherical coordinates. For the wing, for example, ϕ defines azimuth, θ elevation, and η rotations about the long axis.

stitute three points that define the plane of bilateral symmetry for the body. We take the roll ρ to be the angle between the normal vector to this plane, $\hat{L}$, and $\hat{\psi}$. The definitions of these body orientation angles are shown in Fig. 5C.

Because each wing is thin, rigid, and often occluded in one camera view by the insect body, its visual hull resembles a parallelepiped whose long axis is parallel to the wing span vector, $\hat{S}$. To determine $\hat{S}$, we apply PCA to the wing hull voxels. This vector allows for determining the Euler angles for the stroke, ϕ, and deviation, θ (Fig. 5D). The hull cross-sections perpendicular to $\hat{S}$ form parallelograms (Fig. 5E, right). The wing chord vector, $\hat{C}$, is parallel to the longer diagonal of the parallelograms. The third Euler angle for each wing is the pitch angle, η, and is defined to be the angle between $\hat{C}$ and the unit stroke vector, $\hat{\phi}$. To determine $\hat{C}$, hull voxels near the mid-span (within 2 voxel side lengths) are projected onto a plane normal to $\hat{S}$, and the chord is the vector connecting the two voxel projections with the greatest separation. The definitions of all wing orientation angles are detailed in Fig. 5F.

These procedures lead to a full kinematic description consisting of 18 coordinates: three centroid coordinates and three Euler angles each for the body, right wing, and left wing. These coordinates are computed independently for each time step in the movie and checked visually for mistakes. Together, these techniques constitute a Hull Reconstruction Motion Tracking (HRMT) method for extracting 3D kinematics from several 2D views of a flying insect. While the data in this paper pertain to insect flight, this method is applicable with suitable modifications for a variety of three-dimensional motion studies of other complex-shaped, moving objects in space.

2.3.4 Assessing errors of the HRMT method

Discerning subtle differences in flight modes requires clear knowledge of errors in the data recovery method. Such errors cannot be determined from the movies of insects alone, since the actual kinematics are not known beforehand. Instead, we estimate the measurement error by running HRMT on a computer-generated model insect and comparing the extracted positions and orientations of the body to those we impose. The model of the insect consists of five ellipsoids: three for the head, thorax, and abdomen and one for each wing (Fig. 6A). We orient the ellipsoids in a given configuration, use a ray tracing algorithm to determine the three orthogonal shadows, and run our analysis routine to extract the positions and orientations of the body and wings. Compared with the model insect volume, the hull volume is larger and contains extra protrusions that vary in size and location for different insect orientations. These protrusions arise because of occluded regions that are blocked from the view of all three cameras. The protrusions ultimately cause errors in the recovered coordinates, and these errors depend on the orientation of the body and the positions and orientations of the wings. Thus, though validating HRMT using such simulated data does not account for image registration errors, it does account for occlusion defects, which appear to be the primary source of error for the method. However, determining the error dependence on all relevant coordinate variables is not feasible. Since fruit flies typically assume a limited set of orientations and use a typical wing-stroke pattern for flight, we perform an analysis that determines errors for realistic insect configurations. Our synthetic data corresponds to a fixed body and thirty-four wing configurations obtained by applying a manual tracking program to a single stroke from a movie of a hovering fruit fly. Our manual tracking software relies on overlaying images of a virtual fly and is similar to

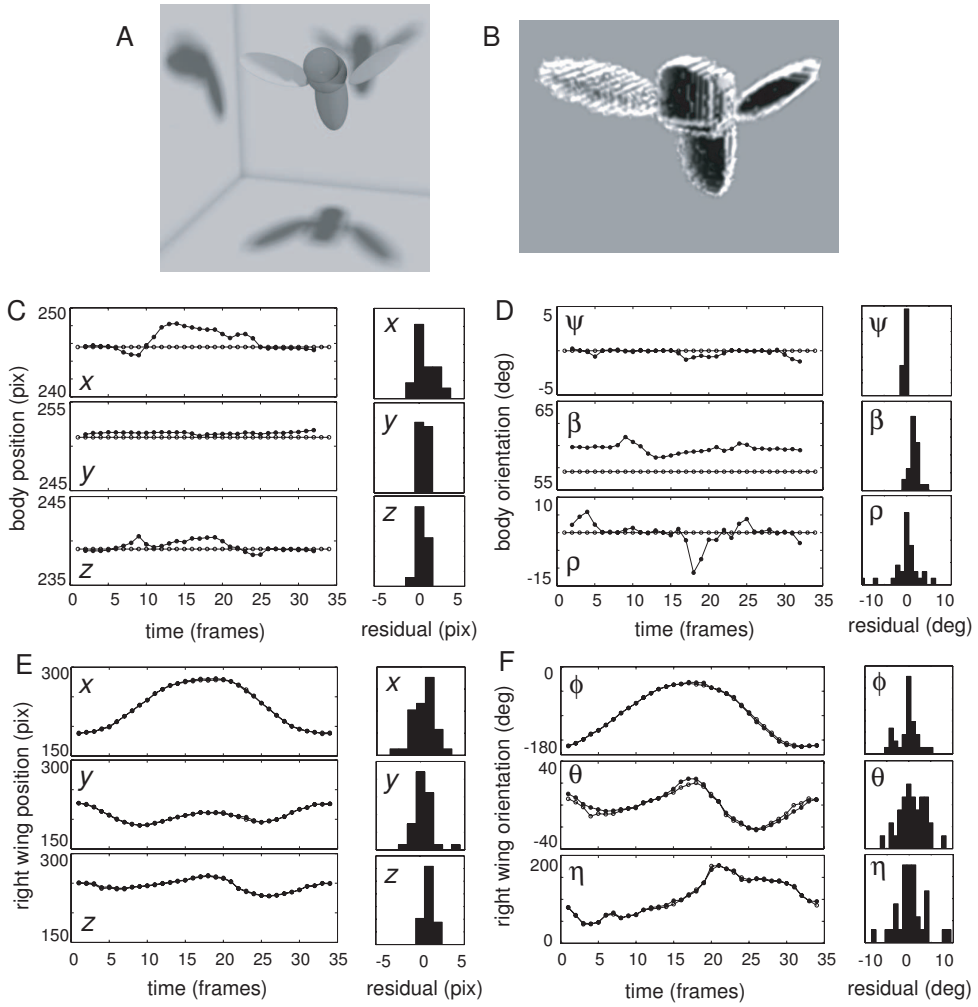

Figure 2.6: A test of the automated tracking algorithm on a computer model of a flapping fly. (A) A morphologically-appropriate model fly consists of five ellipsoids. Three ellipsoids form the head, thorax, and abdomen of the body, and two flat plates represent wings. The wings act as three degree-of-freedom hinges that rotate about a point on the surface of the thorax. (B) Measured flapping motions are imposed on the wings of this model fly, the shadows in each of three views are generated, and finally the tracking algorithm is run on these shadows. For this case, the body is held fixed at a typical orientation of $(\psi, \beta, \rho) = (0, 59, 0)$ degrees. (C) A comparison of the imposed body position (open circles) and the measured position (filled circles) for the centroid (x, y, z). A histogram of the residuals, measured value less the actual value, is shown to the right for each coordinate. The reconstruction method measures the body centroid to within the voxel size of 2 pixels. (D) A similar comparison for the body orientation angles reveals an accurate recovery, with errors of a few degrees. (E) The right wing centroid is recovered to within 2 pixels. (F) The right wing orientation angles can be resolved to better than five degrees. The left wing shows similar statistics.

other implementations [13, 19]. We estimate errors for all wing positions within this stroke as well as the errors associated with viewing this stroke from different angles.

To obtain measurement errors for a typical viewing configuration, we fix the virtual fly body in an orientation of $(\psi, \beta, \rho) = (0, 59, 0)$ degrees and plot the imposed time series data (white dots) and measured values (black dots) for body and wing positions and orientation angles (Fig. 6C-F). The errors for each variable are concisely displayed as a histogram of the residual, defined as the difference between the measured value and the imposed value. For both the body and wing centroids, errors are within the coarse-grained voxel size of 2 pixels. The body orientation is also accurately recovered, generally to within a few degrees. The wing orientation angles and associated residuals for the right wing are shown in Fig. 6F, and the errors for the left wing have similar statistics. Errors for the wing orientations are typically under 5°.

The time series and residual data of Fig. 6 reveal several features of the hull reconstruction method. Most of our measurements average over the voxels in the hull and thus result in subvoxel resolution. Also, the residuals are nearly always centered around zero, indicating that there are only small systematic deviations. Further, the residuals have standard deviations of less than 2 pixels in the positions and 4° in the orientations.

Furthermore, we find that in nearly all the cases we have examined, the mean residuals remain under 3 pixels and under 5°, regardless of both wing position during the stroke and viewing configuration. To summarize the dependence on wing position during the stroke, we plot the residuals for ϕ, θ, and η as a function of stroke angle in the body frame of reference, ϕ_b, for 16 different

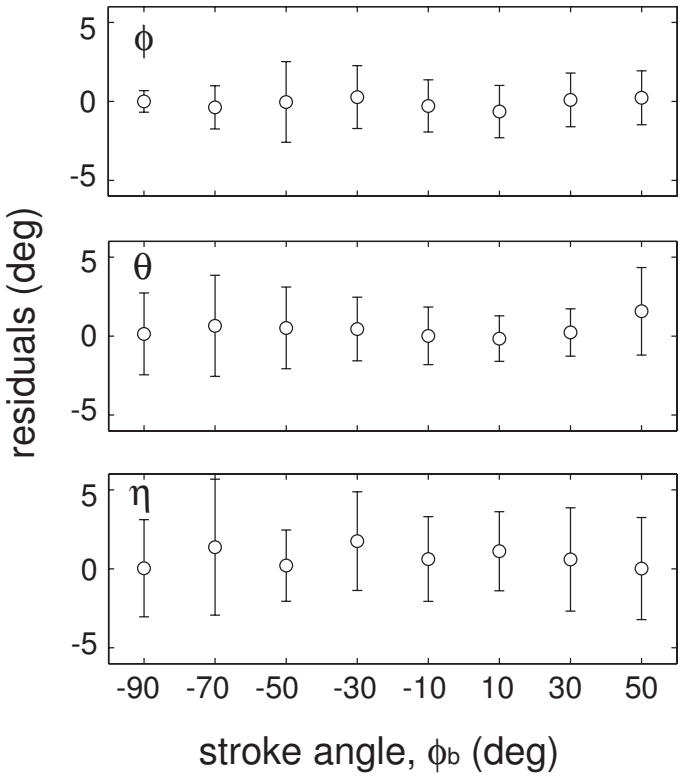

Figure 2.7: Errors in the wing angles are nearly independent of phase in the wing-stroke. To arrive at the displayed mean and standard deviation of residuals, we orient the model fly, impose wing motions, and measure errors in each wing orientation angle. Left and right wing residuals are similar, so we lump these data together. Residuals in each angle are plotted as a function of the imposed stroke angle. The stroke angle ϕ_b is measured in the body frame such that $\phi_b = -90^\circ$ at the dorsal flip and ϕ_b 50° at ventral flip.

viewing configurations (Fig. 7). The configurations range in ψ from 0° to 45°, in β from 54° to 90°, and in ρ from 0° to 60°. In total, this analysis comprises 544 different postures of the insect, and the use of a single wing-stroke in the analysis is justified by the fact that the basic wing motion varies in subtle ways even during extreme maneuvers (Fry et al., 2003). The residuals show no obvious trend with ϕ_b and all have standard deviations of less than 5°.

To summarize the dependence on viewing configuration, we plot the residuals averaged over an entire stroke as a function of body orientation (ψ, β, ρ)

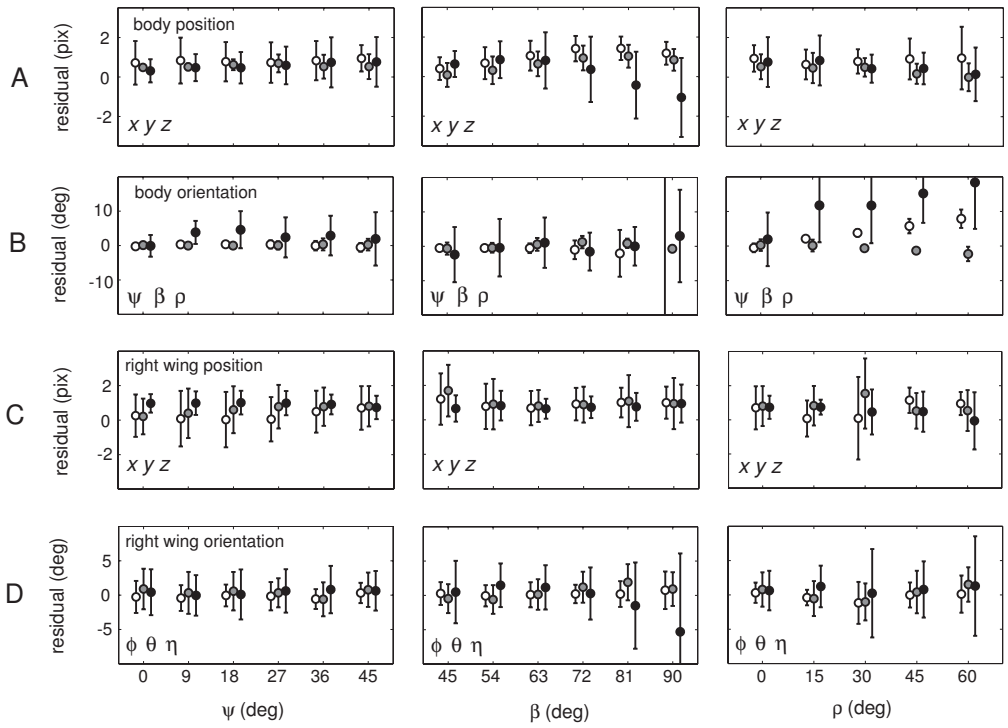

Figure 2.8: Errors in the recovered coordinates depend on the body orientation relative to the cameras. To reveal this dependence, we set the model fly of Fig. 6A in various orientations and measure the residuals in all coordinates. (A) Dependence of body position error on typical values of ψ, β, and ρ. The errors show little dependence on orientation and are generally smaller than the voxel size of 2 pixels. (B) Errors in body orientation as a function of orientation. The body roll ρ is more difficult to resolve than ψ and β and becomes particularly error-prone when the body is rolled considerably. As might be expected, heading ψ is highly inaccurate when the insect is pitched up vertically near $\beta = 90°$. (C) The right wing position is generally resolved to within 2 pixels. (D) The right wing orientation is accurate to within 3 degrees for most typical orientations of the body. For high pitch β and high roll ρ, the wing pitch, η, is not as well resolved. The left wing has similar error statistics.

relative to the viewing configuration (Fig. 8). The residuals for the body and wing positions are all centered within two pixels of zero (Fig. 8A,C). With the exception of highly pitched (β 90°) or highly rolled ($\rho > 15°$) body orientations, the residuals for body and wing orientation angles are also centered within 2° of zero. The increased errors at high β and ρ are not expected to affect most aerodynamic analyses since the fluid force is generated almost entirely by the wings, whose motions are very accurately resolved. Thus, because HRMT tracks each of the body, right wing, and left wing independently in the lab frame of reference, the accuracy of coordinate extraction in any one component is independent of any other. Collectively, these results indicate that HRMT is an accurate method for motion capture of flying insects.

2.4 Results

In order to show the utility of the HRMT method, we apply it to two different recorded maneuvers that exemplify how insects use lateral forces in flight. In particular, we emphasize aspects of these maneuvers performed by insects that differ from similar maneuvers performed by fixed-wing aircraft. In fixed-wing flight, lateral forces are usually generated by rolling or banking the aircraft and inducing a horizontal component to the lift force on the wings. This force enables an airplane or a helicopter to make a turn [10]. Insects on the other hand, could take advantage of the unique features of flapping flight to generate lateral motions. Here, we present an analysis that shows fruit flies can indeed manipulate their wing strokes to generate lateral forces in a manner that is different from simple banking. In addition, we propose a simplified mechanism describing how these kinematic manipulations contribute to the lateral force

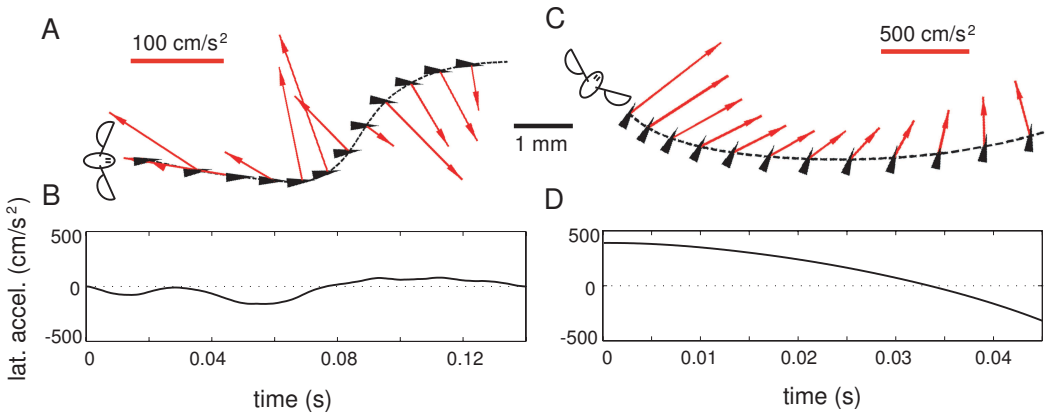

Figure 2.9: Fruit flies undergo lateral acceleration during two maneuvers. Lateral acceleration is the horizontal component of acceleration that is pointed perpendicular to the insect yaw direction. (A) Top view of a "dodge" maneuver. The fly yaw orientation is indicated by the black arrowheads, and the horizontal component of acceleration is shown as the red vectors. During the dodge, the insect moves from one forward trajectory to a nearly parallel forward trajectory. (B) To execute the dodge maneuver, the fly accelerates leftward and then rightward while moving forward. (C) and (D) In this "sashay" maneuver, the fly initially generates a large rightward acceleration that switches to become leftward near the end of the maneuver. Here, the lateral acceleration is as large as 0.4 g. Lateral acceleration is calculated from the body position and orientation data using a window-averaging method for differentiating noisy data (Bergou et al., manuscript in preparation).

production. This mechanism takes advantage of several features of flapping flight, including the large arc-like trajectory of the wings and the independent control of the left and right wing rotation.

2.4.1 Measurement of flight kinematics

In Fig. 9A,C, we show top views of trajectories of two maneuvers. In the first, a fly performs a "dodge" maneuver in which its yaw orientation remains nearly constant while it moves from one straight trajectory to another parallel trajectory (Fig. 9A). In the second trajectory, a fly performs a "sashay" maneuver in

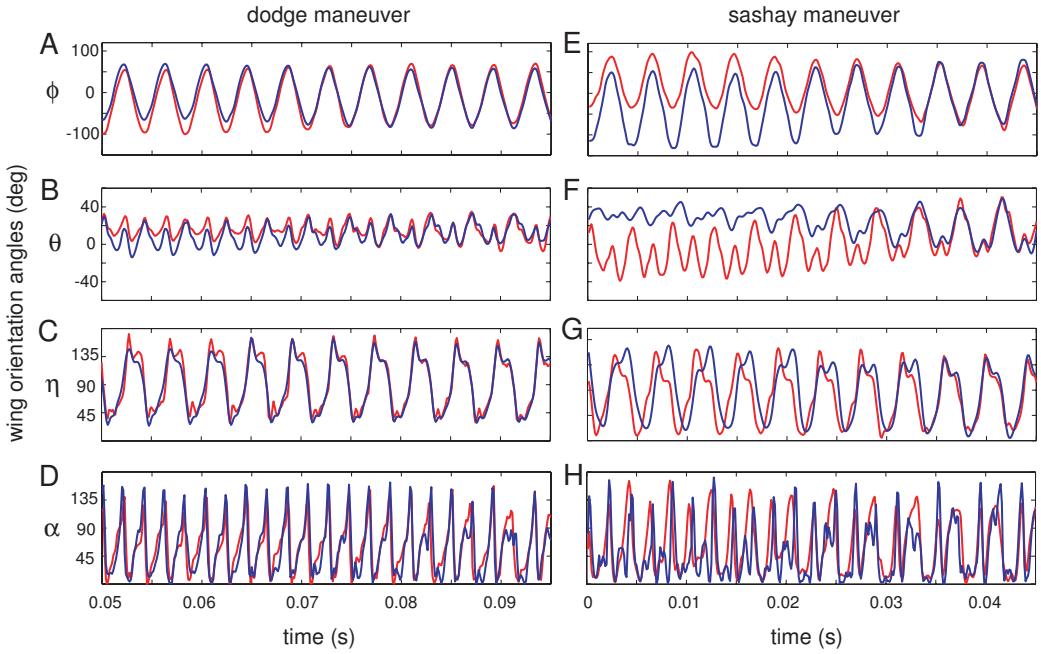

Figure 2.10: Wing orientation angles for two maneuvers. In both cases, the lateral acceleration crosses through zero, and we display wing orientations near such a transition. For the dodge maneuver, the lateral acceleration is leftward before time t 0.075 s and rightward thereafter. For the sashay maneuver, the lateral acceleration is rightward before t 0.033 s and leftward thereafter. (A), (B), and (C) The time course of ϕ_b, θ, and η for the dodge. In order to facilitate comparison of the right and left wings, we have plotted the body frame stroke angle, ϕ_b. (E), (F), and (G) The time course of ϕ_b, θ, and η for the sashay. In both maneuvers, the kinematic data reveal that the wing motion consists of a flipping motion of the wings superposed on the flapping back-and-forth. Asymmetries in the right (red) and left (blue) wing motions are associated with lateral acceleration. (D) and (G) These asymmetries lead to differences in the aerodynamic angle of attack, α, the angle between the chord and the instantaneous wing velocity. This angle is calculated from the other wing orientation angles and has typical errors of 5 to 8 degrees.

which it continuously reorients to face the inside of a turn (Fig. 9C). For this sashay, the body velocity is nearly perpendicular to the yaw direction of the insect. In both of these recorded maneuvers, we see that the insects undergo significant lateral acceleration, that is, the insects produce forces perpendicular to the yaw direction (Fig. 9B,D). See supplementary materials for movies of these two maneuvers.

These forces originate from the detailed wing motions. In Fig. 10 we plot the stroke angle, ϕ, the deviation angle, θ, and the wing pitch angle, η, *versus* time for the left (blue) and right (red) wings throughout the maneuvers. The flapping wing-stroke consists of an upstroke and a downstroke, which are separated by rapid flipping of the wing at stroke reversal. During the downstroke, the wings move roughly horizontally in the lab frame and toward the head of the insect, and during the upstroke the wings move backward. Thus, the motion of the wings is primarily back-and-forth, so ϕ is a nearly sinusoidal function with high amplitude (Fig. 10A,E). Deviation from the horizontal is captured in the angle θ. Because the wings tend to rise slightly at both stroke reversals, θ has two peaks per wing-stroke (Fig. 10B,F). Throughout this motion the wings also rotate about the span axis. The wing pitch angle, η, captures this rotation. During the downstroke, the wing moves forward and η 45°. At stroke reversal, η rapidly increases to nearly 180°. During the upstroke, the wing moves backwards and η 135°. Finally, at the rear stroke reversal, η rapidly decreases to nearly 0° before returning to the downstroke angle of 45° (Fig. 10C,G).

This general flapping and flipping motion is maintained throughout the flight for both maneuvers. We observe symmetric wing motion when the fly undergoes no lateral acceleration, near t 0.075 s for the dodge and t 0.033 s for the sashay (Fig. 9B,D). When the fly accelerates sideways, however, asymmetries appear between the motion of the left and right wings. Maximal sideways acceleration is about 15% g for the dodge and 40% g for the sashay, and all orientation angles exhibit measurable differences between the wings during this lateral force generation. These asymmetries lead to differences in both the trajectory of the wing tips as well as in the wing angles of attack, α, an important variable in determining aerodynamic forces. We define α as the angle between

the chord of the wing and the instantaneous wing velocity and calculate it from the wing orientation angles, (ϕ, θ, η). We plot α *versus* time for the right (red) and left (blue) wings for each maneuver in Fig. 10D,H. In general, the time course of α is marked by periods of relative constant values near 45 degrees at mid-stroke punctuated by rapid increases and decreases as the wing flips at each stroke reversal. Just as for the orientation angles, we observe asymmetries in α for the left and right wings when lateral accelerations are large.

2.4.2 A lateral force generation mechanism

The generation of sideways forces can be rationalized by considering how differences in the motions of the right and left wings lead to asymmetric fluid forces. For example, in both maneuvers, when the fly generates rightward force, the left wing stroke deviation angle, θ_L, is greater than the right wing stroke deviation angle, θ_R. Likewise, for leftward accelerating flight, $\theta_R > \theta_L$. These observations are consistent with the generation of lateral force by sideways tilting the wing stroke planes, in much the same way as a helicopter executes a banked turn. In essence, the lift force, which is normal to wing velocity, is redirected to have a horizontal component. To estimate the magnitude of the lateral acceleration from the redirected lift, we make the approximation that the vertical acceleration is about g and this is redirected by an angle $|\theta_R - \theta_L|/2$. For the dodge maneuver, this calculation yields that the redirected lift force accounts for about 8% g, or about half of the lateral acceleration. For the sashay, a similar calculation shows that lift accounts for 30% g, or about 70% of the lateral acceleration. These estimates suggest that the mechanism of lateral force production is not entirely due to the redirected lift force on the wings. An additional mechanism

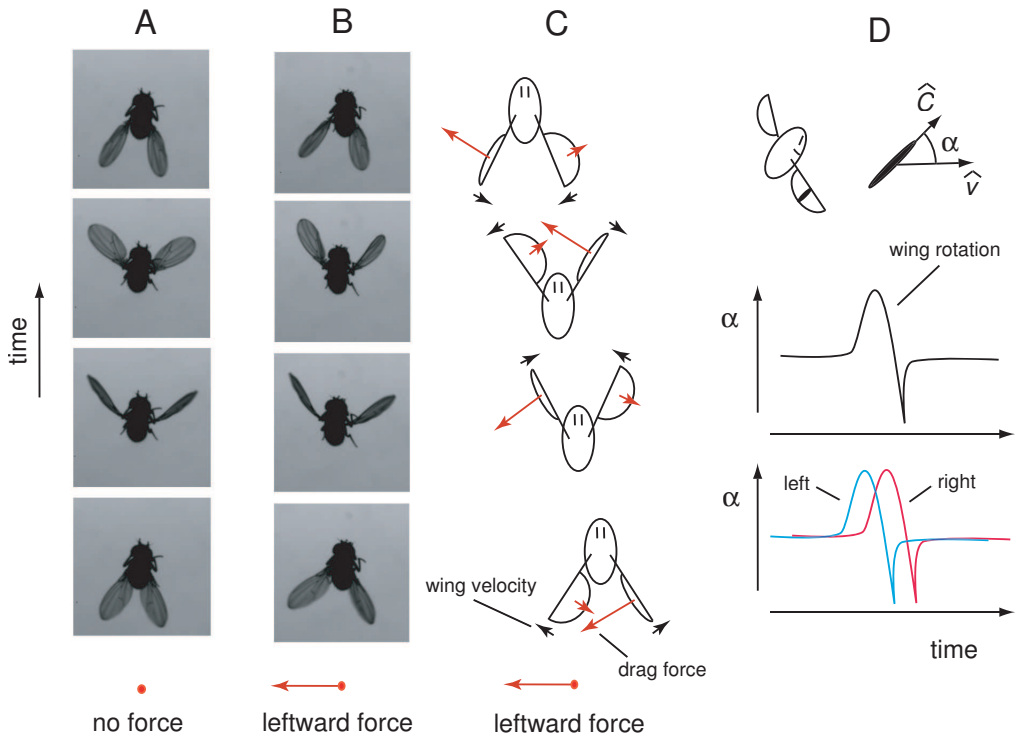

Figure 2.11: A drag-based mechanism of lateral force generation. Fruit flies primarily flap their wings back-and-forth with the upstroke and downstroke separated by rapid wing flips at the stroke reversal. (A) Four snapshots of the wing orientations near stroke reversal for flight with no lateral acceleration. When no lateral force is produced, the wing motions are nearly symmetric between left and right wings. (B) When the insect is accelerating to its left, the right and left wings have different angles of attack, as evidenced by the different projected areas of the wings in this top view. (C) An idealized representation of the wing motion that generates leftward force. By selecting different angles of attack for the two wings near stroke reversal, asymmetric drag forces lead to a lateral force imbalance. (D) This asymmetry can be simply actuated by having the left wing rotate prior to the right, consistent with the timing difference observed in the angle of attack data for laterally accelerating fruit flies. Angle of attack is wing inclination relative to wing velocity.

for producing lateral forces may be associated with the consistent asymmetries in the wing angles of attack.

Generating lateral forces from asymmetries in α can be understood by considering the time-lapsed top view images in Fig. 11A,B. In these images, the

angle of attack is related to the projected area of each wing. Since the wings are primarily moving in the horizontal plane, a large projected area in the top view corresponds to a low angle of attack and a small projected area is associated with a large angle of attack. The nearly horizontal, arc-like wing motion suggests that the drag forces, which act anti-parallel to wing velocity, have a significant lateral component. This is consistent with the fact the wings sweep out a large arc in ϕ, and thus have a lateral component to their trajectories near stroke reversals. When the wings move symmetrically, these drag forces cancel out (Fig. 11A). For motions with asymmetric angles of attack near stroke reversal, the wing with the larger a generates a larger drag force. This imbalance in drag forces induces a lateral acceleration (Fig. 11B).

A schematic representation of the asymmetric wing motion is shown in Fig. 11C. The bottom image shows the fly at the beginning of a downstroke. As the wings begin to move forward, the projected area of the right wing is smaller indicating that α_R is greater than α_L. This asymmetry results in a net drag force that points to the left. Similarly, leftward drag forces are induced near the end of the downstroke where $\alpha_L > \alpha_R$, at the start of the upstroke where $\alpha_R > \alpha_L$, and at the end of the upstroke where $\alpha_L > \alpha_R$. Remarkably, as the schematic in Fig. 11D shows, this seemingly complicated sequence of events can be generated simply by having identical curves for α_L and α_R that are shifted in time. In fact, we do observe timing differences in the measured curves for α_L and α_R for both the dodge and sashay maneuvers (Fig. 10D,H). These observations indicate that such time shifts in wing rotation are important for lateral force generation.

To quantify this idea, we determine the time shift by calculating the correlation integral $I(\Delta t) = \int_0^T \mathrm{d}t \alpha_R \alpha_L (t - \Delta t)$ over a wing beat period, T, and choosing

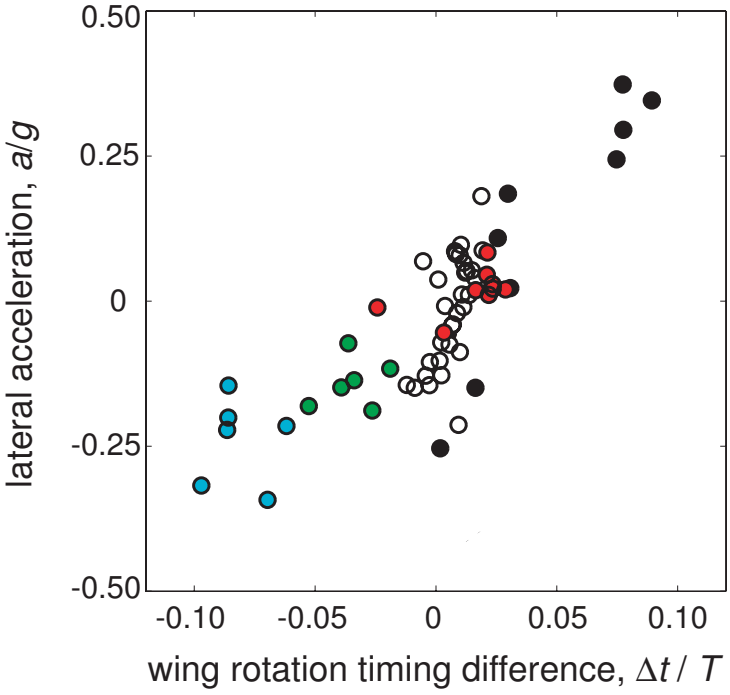

Figure 2.12: Lateral acceleration is correlated with the timing difference in the angle of attack of the right and left wings. Each point represents a single wing-stroke during the dodge (open circles), sashay (solid circles), and three additional sideways flight maneuvers (other symbols). The timing difference, Δt, is the shift in time between the right and left wing angles of attack, α_R and α_L, and has been normalized by the flapping period, T. The value of the lateral acceleration, a, is the average during each wing-stroke and has been normalized by gravitational acceleration, g.

the Δt that maximizes $I(\Delta t)$. We plot lateral acceleration *versus* the normalized $\Delta t/T$ in Fig. 12 and find that these variables are strongly correlated and that larger time shifts correspond to more extreme lateral accelerations. Included in the plot are individual wing-strokes from the dodge and sashay maneuvers discussed above, as well as kinematic data from three additional captured sequences of sideways flight. In total, over 70 wing-strokes and 45,000 individual kinematic measurements were extracted. Remarkably, we find a strong overlap in the data for these maneuvers. This indicates that the timing difference between right and left wing rotation may be a general feature in the mechanism

of lateral force generation of fruit flies.

Finally, we note that that the steep functional form of a near stroke reversal allows slight timing differences to generate large differences in angle of attack. For example, in the dodge maneuver, a time shift of 0.1 ms (2% T) is associated with an instantaneous angle of attack difference of up to 20 degrees. In the sashay maneuver, a time shift of 0.5 ms (10% T) corresponds to an a difference of up to 60 degrees. This suggests that lateral forces are particularly sensitive to slight manipulations of wing rotation timing.

2.5 Discussion

We introduce a new method called Hull Reconstruction Motion Tracking (HRMT) for automated, fast, and accurate extraction of kinematic data from films of flying insects. In particular, we show that with appropriate morphological considerations, three camera views of each flight event are sufficient for extracting the full wing and body kinematics. Our implementation of HRMT is a unique form of motion tracking that combines and builds on image registration, hull reconstruction, clustering, and several geometric and analytic techniques. The main source of error associated with the technique arises from regions outside the fly that are included in the hull because they are blocked from all camera views. Despite these occluded regions, we find that when we test the accuracy of this method by running the algorithm on synthetic data, errors are very small, on the order of 1-3 pixels for centroid positions and 1-5 degrees for the orientation angles.

The HRMT system has many directions for future improvements. For exam-

ple, increasing the number of viewing directions will increase accuracy. Currently the analysis does not make use of intensity differences that can be used to differentiate between various components of an object. The analysis algorithms can be sped up through optimization, exporting portions of the code to programming languages which are faster than MATLAB, and making the code parallel. Also, our implementation does not resolve the roll of the body well, a notoriously difficult task due to the symmetry of the insect body. To better resolve roll, HRMT may be supplemented with marker-based feature tracking or with the imposition of a morphologically-appropriate body model [11]. Further, our current implementation of HRMT uses a simple image registration procedure that takes advantage of the orthogonal filming arrangement and low distortion due to perspective. Calibration of images from more general camera orientations and larger distortions due to perspective would require the use of more general photogrammetric techniques, such as the Camera Calibration Toolbox available for MATLAB. The small errors associated with HRMT for coarse-grained reconstruction also suggests that our method will remain accurate for arrangements that would require such modifications to the registration procedure. Finally, our current implementation does not quantify wing deformations. For *D. melanogaster* such deformations are small. We estimate that the wing camber is largest at stroke reversal and measures about 15%. Such deformations, however, are known to be significantly more prominent in larger insects and are important for understanding aeroelasticity [5]. In order to adapt HRMT to aeroelastic studies, the implementation described in this paper could be combined with other photogrammetric techniques in order to better resolve such deformations [25].

Overall, however, HRMT offers several improvements over present motion

capture techniques. Automation eliminates the need for a researcher to manually perform motion tracking. This allows errors to be characterized in a reliable way, and we show that these errors are small and generally have no systematic dependence on relevant variables. Also, our implementation is fast, easy to implement, and not memory-intensive; it can be run on a commonly-available personal computer. This allows for rapid extraction of flight data and determination of statistically-significant trends. Because the kinematic data are measured entirely in the lab frame of reference, the recovered coordinates are also directly suited for aerodynamic analyses such as computational fluid flow solvers or numerical force models. Finally, HRMT is versatile and may be readily modified for other locomotion studies in which the motion of many components important.

To illustrate the utility of this technique, we use the HRMT method to perform a comprehensive analysis of sideways flight maneuvers of fruit flies. Because our automated filming apparatus was used to capture hundreds of free-flight movies, we were able to then select five films showing unambiguous sideways flight. The HRMT method was used to automatically recover 45,000 kinematic measurements for over 70 wing-strokes. By having access to all of these data, we show that flies are able to generate lateral forces in a manner that takes advantage of the unique features of flapping flight. In particular, we show that sideways-flying insects induce differences in the right and left wing angles of attack near stroke reversal. Based on these data, we propose a model for generating lateral forces by accounting for unbalanced drag due to the difference between the wing angles of attack. Our simplified model predicts that asymmetries in the drag forces can be generated by having identical curves for α_L and α_R that are shifted in time relative to one another. This mechanism is consis-

tent with measurements in dynamically-scaled flapping wing experiments that showed drag is extremely sensitive to the timing of wing rotation at stroke reversal [7]. To test this model, we use the HRMT method to analyze many fruit fly wing-strokes associated with different values of lateral acceleration. We find that there is a strong correlation between the measured lateral acceleration and the measured time shift between the curves for α_R and α_L (Fig. 12). These observations indicate that free-flying fruit flies alter wing rotation timing during maneuvers. This manipulation may be actively controlled by steering muscles [6] or passively influenced by fluid, inertial, or elastic forces [2]. Future studies may elucidate the fluid force generation mechanism in more detail, perhaps using dynamically-scaled experiments [7], fluid force models [3], or computational fluid dynamics algorithms [28]. Irrespective of the detailed force mechanism, our free-flight data suggest manipulation of wing rotation timing is a robust way to control forces during flapping flight. Exotic aerial maneuvers might be implemented in flapping, flying robots using such simple actuation strategies.

2.6 Appendix: Comparison of HRMT to a manual tracking method

Since we present HRMT as an automated alternative to manual tracking techniques, it is important to compare the two approaches. To make this comparison, we first designed a graphical user interface program in MATLAB that has the user position a model insect so that its shadows overlay on the movie images of the actual insect. Our manual tracking program is similar to that of other

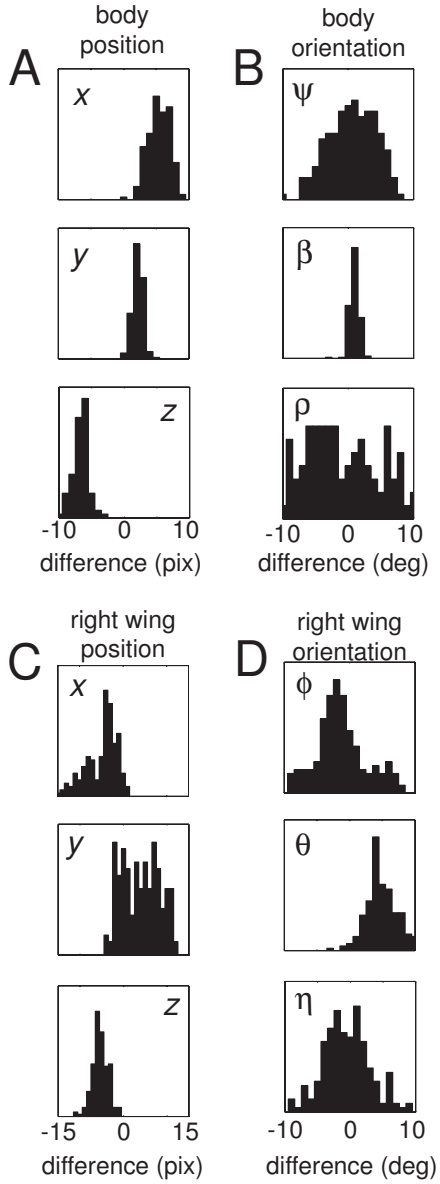

Figure 2.13: Comparison of coordinates tracked by the HRMT method and a manual method. Over 200 frames from the dodge sequence are tracked by both methods, and the differences in the measured coordinates are plotted as a histogram. Comparisons are displayed for the body centroid position (A), the body orientation (B), the right wing centroid position (C), and the right wing orientation (D). The left wing shows similar statistics to the right wing. The mean differences in position coordinates are as high as eight pixels. With the exception of the roll angle, orientation angles recovered by the two approaches are similar, with no mean difference greater than four degrees.

groups [13, 19]. We then performed manual tracking for over 200 frames of a flight sequence. The particular flight sequence captures the dodge maneuver that is discussed in detail above. We also ran HRMT on the same frames and computed the differences between the coordinates extracted by each method (Fig. A1). In general, we find a strong similarity in the two methods, with all mean differences in position coordinates less than eight pixels and all mean differences in angular coordinates less than five degrees. There are small, but systematic differences in the two methods. The differences are likely due in part to inaccuracy in the morphology and connectivity of the model insect needed for manual tracking. There may also be additional occlusion errors in the HRMT method due to morphological differences between the real and model flies. Nonetheless, the similarity of the results obtained by HRMT and by the manual tracking program suggests that both methods are capturing the key features of the wing and body motion.

BIBLIOGRAPHY

[1] B. G. Baumgart. *Geometric modeling for computer vision*. PhD thesis, Stanford University, 1974.

[2] A. J. Bergou, S. Xu, and Z. J. Wang. Passive wing pitch reversal in insect flight. *J. Fluid. Mech.*, 591:321 –337, 2007.

[3] G. J. Berman and Z. J. Wang. Energy minimizing kinematics in hovering insect flight. *J. Fluid. Mech.*, 582:153 –168, 2007.

[4] G. K. M. Cheung. *Visual hull construction, alignment and refinement for human kinematic modeling, motion tracking and rendering*. PhD thesis, Carnegie-Mellon University, 2003.

[5] S. A. Combes and T. L. Daniel. Into thin air: Contributions of aerodynamic and inertial-elastic forces to wing bending in the hawkmoth manduca sexta. *J.Exp. Biol.*, 206:2999–3006, 2003.

[6] M. H. Dickinson, F.-O. Lehmann, and K. G. Goetz. The active control of wing rotation by drosophila. *J.Exp. Biol.*, 182:173–189, 1993.

[7] M. H. Dickinson, F.-O. Lehmann, and S. Sane. Wing rotation and the aerodynamic basis of insect flight. *Science*, 284:1954–1960, 1999.

[8] C. P. Ellington. The aerodynamics of hovering insect flight. iii. kinematics. *Phil. Trans. R. Soc. Ser. B*, 305:41–78, 1984.

[9] A. R. Ennos. The kinematics and aerodynamics of the free flight of some diptera. *J. Exp. Biol.*, 142:49–85, 1989.

[10] Federal Aviation Administration (FAA). *Rotorcraft Flying Handbook*. Aviation Supplies and Academics, 2001.

[11] E. Fontaine. *Automated visual tracking for behavioral analysis of biological model organisms*. PhD thesis, California Institute of Technology, 2008.

[12] E. Fontaine, D. Lentink, S. Kranenbarg, U. K. Mueller, J. L. van Leeuwen, A. H. Barr, and J. W. Burdick. Automated visual tracking for studying the ontogeny of zebrafish swimming. *J. Exp. Biol.*, 211:1305–1316, 2008.

[13] S. N. Fry, R. Sayaman, and M. H. Dickinson. The aerodynamics of free-flight maneuvers of drosophila. *Science*, 300:495–498, 2003.

[14] S. N. Fry, R. Sayaman, and M. H. Dickinson. The aerodynamics of hovering flight of drosophila. *J. Exp. Biol.*, 208:2303–2318, 2005.

[15] T. L. Hedrick and T. L. Daniel. Inverse problems in the flight control of the hawkmoth manduca sexta. *J. Exp. Biol.*, 209:3114–3130, 2006.

[16] T. L. Hedrick, B. W. Tobalske, and A. A. Biewener. Estimates of circulation and gait change based on a three-dimensional kinematic analysis of flight in cockatiels (nymphicus hollandicus) and ringed turtle-doves (streptopelia risoria). *J. Exp. Biol.*, 205:1389–1409, 2002.

[17] M. Jensen. Biology and physics of locust flight. iii. the aerodynamics of locust flight. *Phil. Trans. R. Soc. Ser. B*, 239:511–552, 1956.

[18] G. V. Lauder and P. G. A. Madden. Advances in comparative physiology from high-speed imaging of animal and fluid motion. *Ann. Rev. Physiol.*, 70:143–163, 2008.

[19] Y. Liu and M. Sun. Wing kinematics measurement and aerodynamics of hovering droneflies. *J. Exp. Biol.*, 211:2014–2025, 2008.

[20] W. Nachtigall. Die kinematik der schlagfliigelbewegungen von dipteren. methodische und analytische grundlagen zur biophysik des insektenflugs. *Z. vergl. Physiol.*, 52:155211, 1966.

[21] D. J. S. Newman. *The functional wing morphology of some Odonata*. PhD thesis, University of Exeter, 1982.

[22] S. Revzen, D. E. Koditschek, and R. J. Full. Testing feedforward control models in rapid running insects using large perturbations. *Integr. Comp. Biol.*, 45:1061, 2005.

[23] D. B. Russell. *Numerical and experimental investigations into the aerodynamics of dragonfly flight*. PhD thesis, Cornell University, 2004.

[24] G. J. Stephens, B. Johnson-Kerner, W. Bialek, and W. S. Ryu. Dimensionality and dynamics in the behavior of c. elegans. *PLoS Comput. Biol.*, 4:e1000028, 2008.

[25] Thomas A. L. R. Walker, S. M. and G. K. Taylor. Photogrammetric reconstruction of high-resolution surface topographies and deformable wing kinematics of tethered locusts and free-flying hoverflies. *J. Roy. Soc. Interface*, 6:351–366, 2008.

[26] H. Wang, L. Zeng, H. Liu, and C. Yin. Measuring wing kinematics, flight trajectory and body attitude during forward flight and turning maneuvers in dragonflies. *J. Exp. Biol.*, 206:745–757, 2003.

[27] Z. J. Wang. Dissecting insect flight. *Annu. Rev. Fluid Mech.*, 37:183–210, 2005.

[28] S. Xu and Z. J. Wang. A 3d immersed interface method for fluidsolid interaction. *Comput. Methods Appl. Mech. Engrg.*, 197:2068–2086, 2008.

[29] J. M. Zanker. he wing beat of drosophila melanogaster. i. kinematics. *Phil. Trans. R. Soc. Ser. B*, 327:1–18, 1990.

CHAPTER 3

A PADDLING MODE OF FORWARD FLIGHT IN FRUIT FLIES

3.1 Summary

By analyzing high-speed video of the fruit fly, we discover a swimming-like mode of forward flight that is characterized by paddling motions of the wings[1]. These insects generate drag-based thrust by slicing their wings forward at a low angle of incidence and pushing backwards at a higher angle. We use fluid force models and computer simulations to show that the law for flight speed is determined by these wing motions but is insensitive to material properties of the fluid. Thus, paddling locomotion is as effective in air as in water and represents a common strategy for propulsion through aquatic and aerial environments.

3.2 Swimming and Flying

We do not typically think of fish as flying underwater or insects as swimming through the air. However, flapping fins in water generate thrust from lift as effectively as flapping wings in air [12, 3], and a broad class of swimming and flying animals use their appendages as hydro- or air-foils during lift-based propulsion [21, 18]. Here, we present a complementary convergence for a drag-based propulsion mode that has previously been associated with swimming [4, 21] but now must be included among the strategies for flight. We combine experimental observations of flying insects and fluid force modeling to reveal a mode of insect flight in which the wings operate as paddles that push off the air.

[1]The work presented in this chapter has been submitted for publication to *Phys. Rev. Lett.*

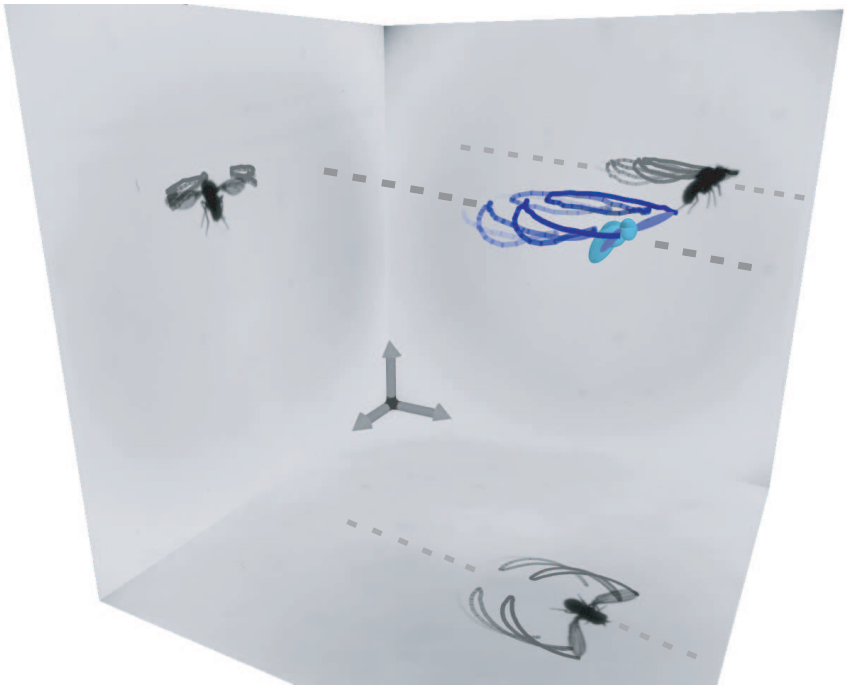

Figure 3.1: Reconstruction of forward flight of a fruit fly (body length 2.5 mm). The sequence is recorded using three high-speed video cameras, and snapshots from each camera are displayed on the side panels. The positions and orientations of the insect body and wings are extracted, and these data are displayed on the reconstructed insect for a single frame. The wings beat in horizontal arcs about the body, and wing-tip trajectories for several wing-beats are shown in dark blue.

3.3 Forward Flight in Fruit Flies

We use three orthogonal high-speed video cameras to capture many flight sequences of the fruit fly, *D. melanogaster* [17]. We then select sequences of forward flight and use a motion tracking algorithm to extract the time-resolved, three-dimensional motions of the body and wings. Images selected from one flight sequence are shown on the side panels of Fig. 3.1, and the measured posture of the insect is visualized by the computer-generated reconstruction. To determine the aerodynamic basis of the thrust generation, we analyze the flapping motions of its wings. Previous studies of forward flight in insects have empha-

sized the nose-down tilting of the wing stroke planes [21, 6, 19, 20, 8, 9, 26], a mode in which thrust is generated by re-direction of lift. In addition to this lift-based mode, we discover a new mode in which the wings primarily beat in a horizontal plane, as during hovering. The wing-tip trajectories of Fig. 3.1 show that the wings beat back-and-forth as they progress with the forward motion of the insect body. To drive flight at different speeds, the insects make adjustments to these wing motions.

These adjustments can be discerned by contrasting the wing motions associated with low- and high-speed flight. In both cases, each wing sweeps along a globe centered about its root on the body [Fig. 3.2(a)]. The wing motions are visualized by the stroke diagrams associated with hovering flight [Fig. 3.2(b)] and fast forward flight [Fig. 3.2(c)]. These diagrams show that both slow and fast flight are characterized by a horizontal stroke plane with the forward and backward sweeps separated by rapid wing flips. These kinematics can also be quantified by the time-course of three orientation angles: the stroke angle measured in the horizontal plane, the vertical deviation angle, and the pitch angle. In Fig. 3.2(d-f), we compare the measured angular data for sequences at flight speeds of 2 cm/s (blue) and 43 cm/s (red). Differences can be seen for the time-course of all three angles, suggesting that all three degrees of freedom may contribute to the thrust generation.

3.4 Modulation of Wing Pitch

Recent studies of fruit flies have shown that changes in wing pitch play an important role in generating turning maneuvers [16, 1]. In the case of forward

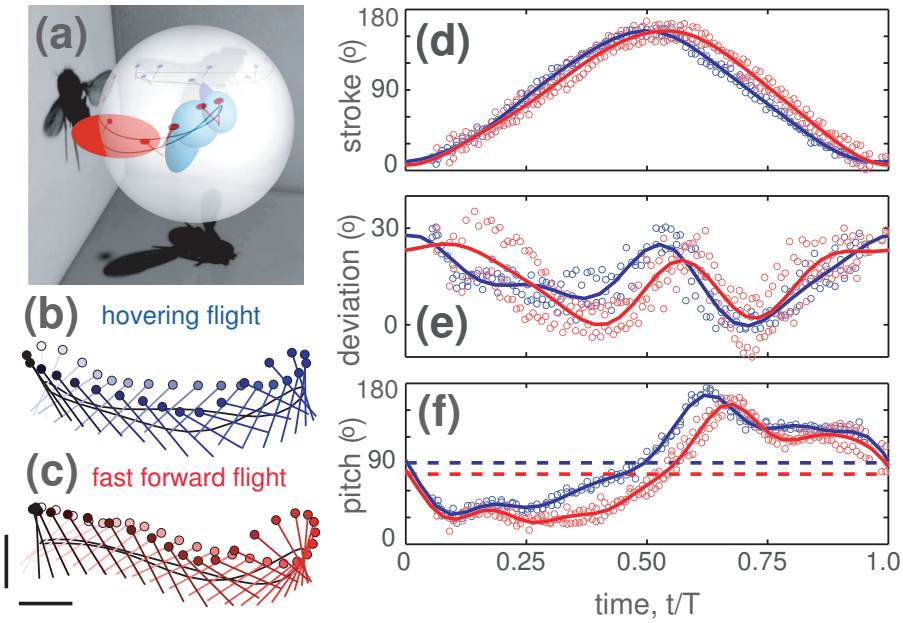

Figure 3.2: Comparison of wing motions for hovering (forward body speed $u = 2$ cm/s) and fast forward flight ($u = 43$ cm/s). (a) Each wing sweeps a path along a globe centered about its root on the body. (b and c) The motions are unwrapped in wing-stroke diagrams which represent the wing as a line segment with a ball at the leading edge (scale bars, 30°). Beginning with the forward sweep, the wings are colored darker with time and displayed at the camera acquisition rate of 8000 Hz. (d-f) Wing orientation angles for hovering (blue, wing-beat period $T = 4.0$ ms) and forward flight (red, $T = 4.8$ ms). Stroke angle is measured in the horizontal plane, deviation angle is the vertical excursion, and pitch angle is measured between the wing chord and the horizontal plane. Experimental measurements (circles) are phase-averaged, and right and left wing data are pooled and used to form the Fourier fits (solid lines). Mean values of wing pitch are shown as dashed lines in (f).

flight, we also observe changes in pitch for flight at different speeds. In particular, the curve for pitch during fast flight is shifted downward relative to pitch during slow flight [(Fig. 3.2(f)]. This downward shift can be rationalized by considering its effect on aerodynamic forces on the wings. During the forward stroke, the low value of wing pitch indicates the wing is more horizontal and thus slices through the air. During the backward stroke, the low value of pitch indicates the wing is more vertical, in effect pushing off the air with a broad

area exposed to the flow. Thus, a uniform decrease in wing pitch angle generates rowing or paddling motions that propel the insect forward.

To determine the degree to which the forward motion is generated by paddling, we use a computational simulation that determines the body motion from aerodynamic forces on the wings [1]. Flapping wing motions are prescribed, a quasi-steady model is used to compute wing forces, and the body motion is calculated from the thrust produced. Computed flight velocities are typically within 10 cm/s of the measured values [Fig. 3.3(a)]. To systematically evaluate the relative importance of the measured changes in the stroke, deviation, and pitch angles, we use the simulation to determine the flight speed for hybrid wing motions. In Fig. 3.3(b), we compare the simulations of the complete hovering (blue) and fast flight (red) kinematics to simulations in which the wing kinematic angles are selected from a mix of these two data sets. For example, the color scheme blue-red-blue indicates that the stroke, deviation, and pitch angles are taken from the hovering sequence, the fast flight sequence, and the hovering sequence, respectively. Simulations of the six possible hybrid kinematics divide into two distinct groups according to speed. Slow flight speeds are associated with kinematics in which the wing pitch is selected from the hovering sequence, regardless of the sources of the stroke and deviation angles. Conversely, high speeds are associated with pitch selected from the fast flight sequence. These results indicate that the changes in wing pitch of Fig.3.3(f) are crucial to determining flight speed.

Further, we find that the *mean value of pitch* in particular correlates with flight speed. When the complete hovering kinematics are modified only by shifting the curve for pitch downward so as to have the same mean as that of the fast

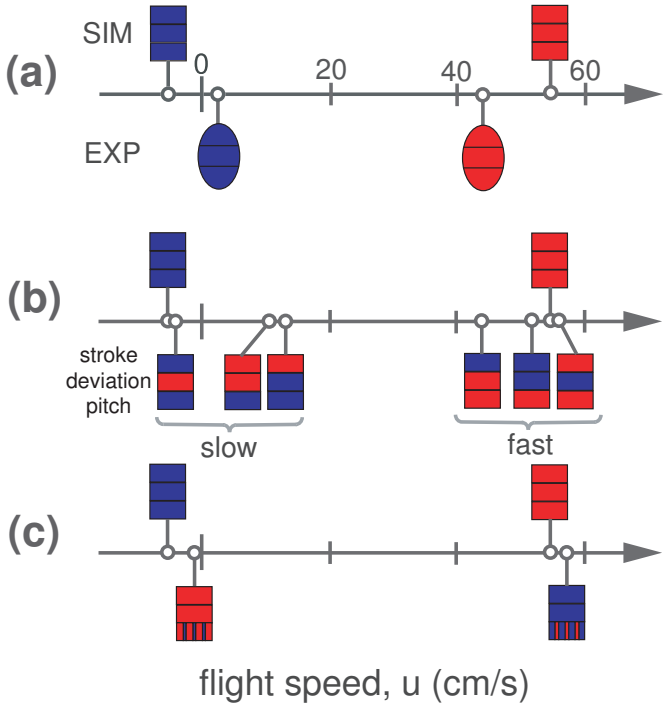

Figure 3.3: Dependence of flight speed on wing orientation angles. (a) When the measured wing motions for hovering (blue) and fast flight (red) are played in simulation (top), the computed speeds are comparable to experimental values (bottom). (b) Simulations of hovering and fast flight kinematics (top) are compared to hybrid kinematics (bottom). For hybrid simulations, wing motions are formed by selecting each orientation angle – stroke, deviation, and pitch – from either the hovering or fast flight data sets. Slow speeds are associated with pitch from the hovering sequence, and high speeds are associated with pitch from the fast flight sequence. (c) Simulations of hovering and fast flight kinematics (top) are compared to simulations in which the mean values of pitch have been swapped (bottom). For example, blue stripes on the otherwise red kinematics indicate that the fast flight kinematics have been modified *only* by shifting the pitch curve upward so as to have the hovering sequence's mean value (dashed line of Fig. 2f).

flight sequence, the simulation yields a speed close to that of the fast flight simulation [Fig. 3.3(c)]. Conversely, shifting the wing pitch for fast flight upward causes the speed to slow to near zero. Thus, although the wing motions are complex, much of this flight mode is accounted for by the stroke-averaged value of wing pitch.

3.5 Aerodynamic Model of Paddling Flight

These findings inspire a minimal model that includes only changes in average pitch to drive flight at different speeds. In this model, each wing sweeps forward and backwards at constant speed w relative to the insect body. In hovering, both wings are inclined symmetrically during the forward and backward strokes, with angles of attack between the wing chord and its velocity of $\alpha_F = \alpha_B = \alpha_0 = 45°$ [Fig. 3.4(a)]. The wing drag, which points opposite to the wing velocity at any instant, cancels over each complete wing-beat, and the insect hovers. Forward flight results from asymmetric attack angles, $\alpha_F = \alpha_0 - \Delta\alpha$ and $\alpha_B = \alpha_0 + \Delta\alpha$, and the insect flies faster by increasing the wing paddling angle $\Delta\alpha$ [Fig.3.4(b)]. For these idealized paddling motions, $\Delta\alpha$ corresponds to the downward shift in pitch relative to 90°. Physically, paddling causes larger wing drag for the backward sweep than for the forward sweep [21, 2], and this unbalanced drag propels the insect forward. As the insect progresses forward, the wing velocities relative to air are modified, causing a resistive drag. Eventually, the drag arising from paddling balances drag due to the forward motion, and the insect achieves a speed u.

To quantify these dynamics, we average drag over a wing-stroke and ap-

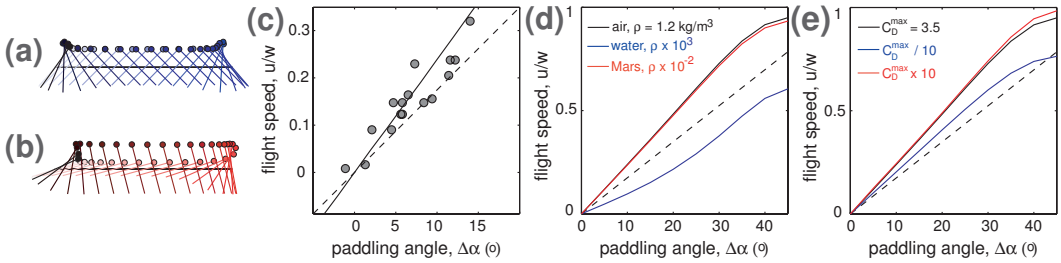

Figure 3.4: Paddling wing motions drive forward flight. (a) During idealized hovering, each wing assumes equal inclination relative to the flow for the forward and backward sweeps. (b) During idealized paddling forward flight, the wing inclination is adjusted by uniformly shifting the pitch downward by the paddling angle $\Delta\alpha$ (here, 30°). (c) The flight speed u, normalized by wing speed w, correlates with paddling angle for 16 sequences of forward flight (circles). The trend is consistent with predictions of a simple aerodynamic model (Eq. **??**, dashed line) and simulation (solid line). Simulations confirm that the relation between flight speed and paddling angle is insensitive to changes in the density of the fluid (d) and the drag coefficient (e).

proximate the coefficient of drag, $C_D(\alpha) \approx C_D^{max} \sin^2(\alpha)$ [5]. For a wing of area S moving at speed v relative to a fluid of density ρ, the high Reynolds number pressure drag law is $D = \rho S C_D(\alpha) v^2/2$ [12, 3], and the steady-state force balance for a pair of wings moving with the body is:

$$D = \frac{1}{2}\rho S\,[-C_D(\alpha_F)\cdot(w+u)^2 + C_D(\alpha_B)\cdot(w-u)^2] = 0. \tag{3.1}$$

As each wing sweeps forward, wing speed relative to air is large but the attack angle, and thus C_D, is small. As each wing sweeps backward, its airspeed is small but C_D is large. To derive a control law for flight speed, we assume small $\Delta\alpha$ and thus linearize the drag coefficient about α_0, $C_D(\alpha) \approx C_D(\alpha_0)\cdot(1 + 2\cdot\Delta\alpha/\tan(\alpha_0))$, which for $\alpha_0 = 45°$ becomes $C_D(\alpha) \approx C_D^{max}\cdot(1 + 2\cdot\Delta\alpha)/2$. For slow body speeds, second-order terms $(u/w)^2$ are negligible, and we use Eq. 3.1 to derive a law that relates forward flight speed to wing speed and paddling angle:

$$u = w\cdot\Delta\alpha. \tag{3.2}$$

Thus, flight speed is expected to depend strongly on the degree of wing pad-

dling.

To validate this control law, we gather flight sequences with predominantly forward motion, steady motion (acceleration $< 0.15g$), and a horizontal stroke (stroke-plane angle $< 5°$). For each movie, we measure the full wing kinematics [17] and then extract the paddling angle, the mean speed of the wings, and the mean forward speed of the body. In Fig. 3.4(c), we plot the ratio of the body speed to wing speed versus the paddling angle for 16 sequences of paddling flight. The prediction of the minimal model is shown by the dashed line that is in qualitative agreement with the overall trend in the data but somewhat under-predicts the expected flight speed. Playing idealized wing-strokes in simulation (solid line) also captures the trend. Collectively, these physically-based models and experimental observations confirm that wing paddling produces drag-based thrust in this flight mode.

3.6 Paddling in Air and Water

The minimal model, which assumes steady wing and body motions within a wing-beat, predicts that flight speed during paddling does not depend on the fluid medium. In particular, fluid density and drag coefficient do not appear in the law of Eq. 3.2. To evaluate the influence of unsteady effects on the flight speed law, we again simulate idealized paddling strokes [Fig. 3.4(a,b)], vary the fluid density and coefficient of drag, and measure the resulting flight speed. Fig. 3.4(d) summarizes the dependence of flight speed on $\Delta\alpha$ for different density fluids. Paddling in air (black curve) and in lower density fluids such as the Martian atmosphere (red) give rise to similar flight speeds. Paddling in water

(blue), which is a thousand times denser than air, leads to a slightly slower speed. Thus, changing the fluid density, and hence the fluid forces, by 5 orders of magnitude leads to changes in flight speed of only about 50%. Similarly, increasing or decreasing the drag coefficient by a factor of 10 leads to modest changes in the speed law [Fig. 3.4(e)].

These simulations indicate that the changes in speed for varying densities and force coefficients result from unsteady wing and body oscillations. Nonetheless, the simple law of Eq. 3.2 provides a good rule-of-thumb for estimating body speed over a wide range of fluid densities and force coefficients. This insensitivity of locomotion speed to material properties typically stems from a common physical origin of the driving and resisting forces [4, 21]. In the case of flapping flight, these forces are associated with pressure drag on the wings. Doubling the density, for example, doubles both the propulsive and resistive forces, leaving the velocity at which force balance is achieved unchanged. Thus, paddling locomotion is as effective in air as in water.

3.7 Implications

Because of its prevalence among swimmers – from ciliated micro-organisms [12, 3] to semi-aquatic birds and mammals [10] and fish that use pectoral fins [22] – paddling has largely been viewed as an aquatic phenomenon [4, 21]. However, recent work indicates drag is important in hovering flight of some insects [23, 24], and our experimental observations and aerodynamic simulations suggest that drag-based paddling propulsion may be common among flyers. We have highlighted pure paddling flight in the fruit fly, and more generally

forward flight is driven by both lift and drag which are associated with stroke-plane tilting and wing pitching, respectively. Though considered less effective than lift-based locomotion [21, 2, 22], pure paddling offers several advantages for forward flight. It requires no re-orientation of the body and is dictated by a linear relation (Eq. 3.2) that could simplify the flight speed control strategy [11] and actuation of wing motions [1]. Perhaps most importantly, paddling recruits drag for thrust while largely maintaining the lift needed to support body weight.

The use of common mechanisms for locomotion in different media suggests that swimmers and flyers share similar adaptations for generating and controlling movement [4]. The similarities between locomotion in water and in air may also shed light on the very origin of flight in insects. One evolutionary theory contends that the aerodynamic function of flapping appendages emerged from their use in underwater ventilation or swimming [25, 14]. However, the seemingly great differences between swimming and flying have previously been viewed as evidence against this theory [6, 7]. Instead, we interpret the use of common strategies as offering physical plausibility to the swimming-to-flying transitional scenario. In particular, the characteristics adapted for swimming could have been readily co-opted for use in flight, and swimming would provide a context to evolve flapping appendages without the demands of weight support and stability. The physical plausibility of this transition is also supported by observations of insects that use their wings for both swimming and flying [13, 15] as well as by insects that row their wings while skimming on the surface of water [14].

BIBLIOGRAPHY

[1] A. J. Bergou, L. Ristroph, J. Guckenheimer, I. Cohen, and Z. J. Wang. Fruit flies modulate passive wing pitching to generate in-flight turns. *Phys. Rev. Lett.*, 104:148101, 2010.

[2] R. W. Blake. Mechanics of drag-based mechanisms of propulsion in aquatic vertebrates. *Symp. Zool. Soc. Lond.*, 48:29–52, 1981.

[3] S. Childress. *Mechanics of Swimming and Flying*. Cambridge University Press, Cambridge, 1981.

[4] M. W. Denny. *Air and Water: The Biology and Physics of Life's Media*. Princeton University Press, Princeton, 1993.

[5] M. H. Dickinson, F.-O. Lehmann, and S. P. Sane. Wing rotation and the aerodynamic basis of insect flight. *Science*, 284:1954–1960, 1999.

[6] R. Dudley. *The Biomechanics of Insect Flight: Form, Function, Evolution*. Princeton University Press, Princeton, 2000.

[7] R. Dudley, G. Byrnes, S. P. Yanoviak, B. Borrell, R. M. Brown, and J. A. McGuire. Gliding and the functional origins of flight: Biomechanical novelty or necessity? *Annu. Rev. Ecol. Evol. Syst.*, 38:179–201, 2007.

[8] R. Dudley and C. P. Ellington. Mechanics of forward flight in bumblebees. i. kinematics and morphology. *J. Exp. Biol.*, 148:19–52, 1990.

[9] R. Dudley and C. P. Ellington. Mechanics of forward flight in bumblebees. ii. quasi-steady lift and power requirements. *J. Exp. Biol.*, 148:53–88, 1990.

[10] F. E. Fish. Transitions from drag-based to lift-based propulsion in mammalian swimming. *Amer. Zool.*, 36:628–641, 1996.

[11] S. N. Fry, N. Rohrseitz, A. D. Straw, and M. H. Dickinson. Visual control of flight speed in drosophila melanogaster. *J. Exp. Biol.*, 212:1120–1130, 2009.

[12] M. J. Lighthill. *Mathematical Biofluiddynamics*. SIAM, Philadelphia, 1975.

[13] H. Lubbock. On two aquatic hymenoptera, one of which uses its wings in swimming. *Trans. Linn. Soc. Lond.*, 24:135–141, 1863.

[14] J. H. Marden and M. G. Kramer. Surface-skimming stoneflies: a possible intermediate stage in insect flight evolution. *Science*, 266:427, 1994.

[15] R. Matheson and C. R. Crosby. Aquatic hymenoptera in america. *Ann. Entomol. Soc. Am.*, 5:65–71, 1912.

[16] L. Ristroph, A. J. Bergou, G. Ristroph, K. Coumes, G. J. Berman, J. Guckenheimer, Z. J. Wang, and I. Cohen. Discovering the flight autostabilizer of fruit flies by inducing aerial stumbles. *PNAS*, 107:4820, 2010.

[17] L. Ristroph, G. J. Berman, A. J. Bergou, Z. J. Wang, and I. Cohen. Automated hull reconstruction motion tracking (hrmt) applied to sideways maneuvers of free-flying insects. *J. Exp. Biol.*, 212:1324, 2009.

[18] G. K. Taylor, R. L. Nudds, and A. L. R. Thomas. Flying and swimming anaimals cruise at a strouhal number tuned for high power efficiency. *Nature*, 425:707, 2003.

[19] S. Vogel. Flight in drosophila. i. flight performance of tethered flies. *J. Exp. Biol.*, 44:567, 1966.

[20] S. Vogel. Flight in drosophila. ii. variations in stroke parameters and wing contour. *J. Exp. Biol.*, 46:383, 1967.

[21] S. Vogel. *Life in Moving Fluids*. Princeton University Press, Princeton, 1994.

[22] J. A. Walker and M. W. Westneat. Kinematics, dynamics, and energetics of rowing and flapping propulsion in fishes. *Integr. Comp. Biol.*, 42:1032–1043, 2002.

[23] Z. J. Wang. Two dimensional mechanism for insect hovering. *Phys. Rev. Lett.*, 85:2216–2219, 2000.

[24] Z. J. Wang. The role of drag in insect hovering. *J. Exp. Biol.*, 207:4147–4155, 2004.

[25] V. B. Wigglesworth. Evolution of insect wings and flight. *Nature*, 246:127, 1973.

[26] A. P. Willmott and C. P. Ellington. The mechanics of flight in the hawkmoth manduca sexta. i. kinematics of hovering and forward flight. *J. Exp. Biol.*, 200:2705–2722, 1997.

CHAPTER 4

PADDLING DRIVES YAW TURNING MANEUVERS

4.1 Summary

Flying insects execute aerial maneuvers by subtly modulating the flapping motions of their wings[1]. Here, we examine how such changes in wing motions lead to body motion and also how the wing motions themselves arise. We elicit free-flight turning maneuvers of fruit flies, capture these events using high-speed video cameras, and use a new motion tracking algorithm to extract the wing and body motions through time. We find that these insects generate drag-based torque by adjusting wing inclination to push off or slice through the air. We use aerodynamic models to show how these paddling wing motions determine the rotational dynamics of the body. Further, we present a biomechanical model that shows how these motions arise from the interaction of active modulation and passive dynamics.

4.2 Turning Flight as a Paradigm of Complex Behavior

When searching for food, flies display a characteristic foraging behavior: straight flight paths are separated by rapid changes in heading called *saccades* [5]. For fruit flies, a typical saccadic turn is through 90 degrees and is complete in about 50 ms, or 10 wing-beats. Since Collett and Land first investigated saccades in detail in 1975 [4], these flight maneuvers have emerged as an archetype

[1]The work presented in this chapter is modified with permission from Bergou, Ristroph *et al.*, *Phys. Rev. Lett.*, **104**, 148101 (2010) and includes portions based on material published in Ristroph *et al.*, *PNAS*, **107**, 4820-4824 (2010).

of complex animal behavior. The primary goal of these investigations has been to dissect the many layers to such maneuvers. This approach seeks to understand how the sensory, neural, and muscular systems interact with aerodynamics in orchestrating the turn.

The earliest studies of in-flight turns involved preparations in which the insects were tethered or fixed in place. Though these insects cannot physically turn, they can be made to generate yaw torque by presentation of visual stimuli [8]. For example, a tethered fly flapping its wings will attempt to turn along with a rotating pattern of stripes. This gaze stabilization response serves to eliminate optical flow in the visual field of the insect. Though such studies have been important in showing this stereotyped and robust behavior, they do not allow for a full understanding of turning behavior.

As a next step, some researchers developed loose-tether preparations. One involves the tethering of flies to a loose fiber, allowing for some rotation [11]. A second involves a magnetic tether, in flies are held in place but allowed to swivel about a magnetic pin [1]. However, for both such approaches, the distribution of turning angles shows a marked difference from that seen in free-flying insects [14]. This suggests that loose-tether preparations influence flight behavior.

In 2003, the Dickinson group studied free-flight turns in fruit flies [7]. Saccades were filmed with three high-speed cameras aimed near a vinegar-laced dark cylinder. Attracted by the smell, flies approach the cylinder and perform collision avoidance turns. By measuring the complete wing and body kinematics, this study aimed to rationalize the aerodynamic basis of the generated yaw torque. To do so, the wing kinematics were replayed on a dynamically-scaled mechanical flapping wing. The researchers found that the wing motions indeed

generated sufficient yaw torque to drive the turn, and they implicated changes of about 2° in stroke-plane angle and 5° in wing-beat amplitude. The central conclusion of the study indicates that the torque associated with these changes in wing motions primarily has to overcome inertia of the insect body.

Here, we revisit free-flight turns in fruit flies. We show two key results that are at odds with these previous findings. First, the modulation of wing inclination or angle of attack is an important parameter in driving yaw turns. Second, the torque generated must not only overcome body inertia but also an effective damping of body rotations due to aerodynamic forces on the flapping wings. In addition, we show that high quality kinematic data can even be used to elucidate how the wing motions arise from an interaction of actuation biomechanics and aerodynamics.

4.3 Eliciting and Capturing Turning Maneuvers

To elicit free-flight turns, we take advantage of the gaze stabilization response of flies. We display a rotating striped pattern of lights that induces saccade-like turns in the direction of rotation. The apparatus used is shown in Fig. 4.1. Three high-speed cameras aim toward the central point in a clear flight chamber [12]. Inside the chamber and just above the filming volume is a ring of panels that are covered in an array of light-emitting diodes. A micro-controller is used to play computer-generated patterns on the arrays. In these experiments, we light up alternate panels and have this striped pattern rotate when a fly breaks two-crossed laser beams. The breakage trips a circuit that initiates rotation and signals the cameras to record.

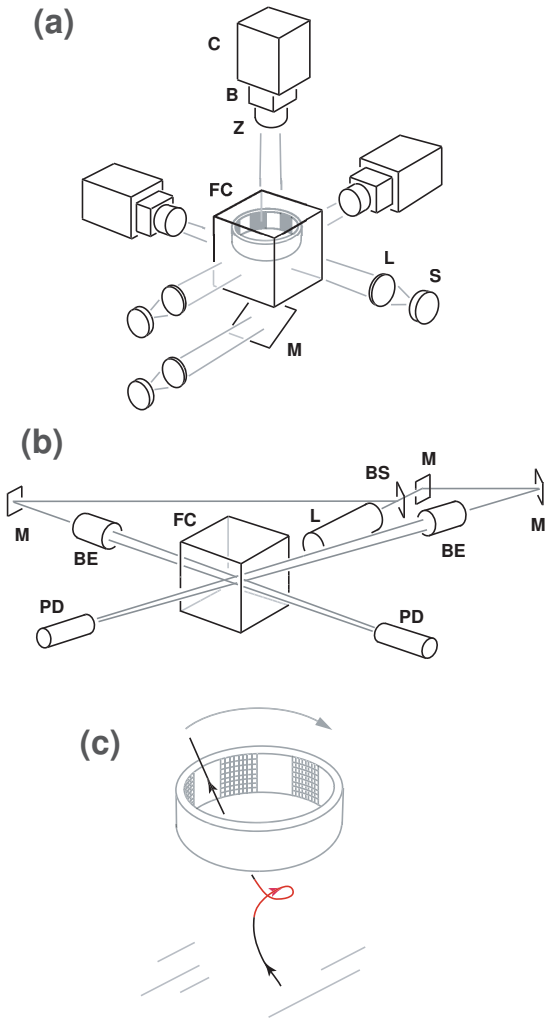

Figure 4.1: Schematic of the apparatus used to elicit and capture video of turning maneuvers. (a) Three high-speed cameras (C) focus on a cubic volume (2 cm side length) in a larger plexiglas flight chamber (FC). The chamber contains a panel of light-emitting diode arrays in which patterns of light can be played. Each camera is fitted with a magnifying bellows (B) and a zoom lens (Z), and each view is back-lit by a bright red light-emitting diode source (S) that is focused using a simple convex lens (L). (b) An optical triggering system detects the presence of an insect in the filming volume and signals the cameras to record and a striped pattern of lights to rotate. A red laser (L) emits a beam that is divided by a beam splitter (BS), re-routed by mirrors (M), passed through Galilean beam expanders (BE) and the chamber, and focused on photodiodes (PD). When an insect flies through the intersection of the beams, it is detected by the photodiodes, and a triggering circuit (not shown) initiates recording. (c) As an insect flies through the beams, the cameras capture the portion (red) of its trajectory that includes the insect's response to the rotating pattern.

4.4 Turning Kinematics

To rationalize the physical basis of turning maneuvers, we analyze an extreme turn in detail. In Fig. 4.2(a), we display several snapshots taken from a saccade through about 120 degrees. The insect starts from hovering on the right, rapidly changes yaw or heading while drifting leftward, and then flies forward and away. The turn is complete in about 80 ms or 15 wing-beats. We use our motion tracking program to extract the wing and body positions and orientations over time, and we display the configuration of the insect for several snapshots during the maneuver.

The motion of each wing is described by the time-course of three Euler angles [Fig. 4.2(b)]. The stroke angle describes the orientation in the horizontal plane. Because the wings continually flap back-and-forth, the stroke angle is similar to a sinusoidal function of time, as shown in Fig. 4.2(c). The deviation angle describes the vertical excursion of the wing. The small oscillations in deviation correspond to heaving motions up and down [Fig. 4.2(d)]. Finally, the pitch angle is the inclination of the wing relative to the forward horizontal. The wing pitch is near 45 deg for the forward sweep of the wings, flips over, and then is near 135 deg for the backward, flips over again, and repeats. The time course of wing pitch is shown in Fig. 4.2(e).

During the turn, these flapping and flipping motions are maintained but modified with respect to all three Euler angles. In seeking the aerodynamic basis of turns, we first look for differences between the motions of the right and left wings. Because differences appear in all angles, we make use of an insect flight simulation to evaluate the relative importance of these changes [2]. First,

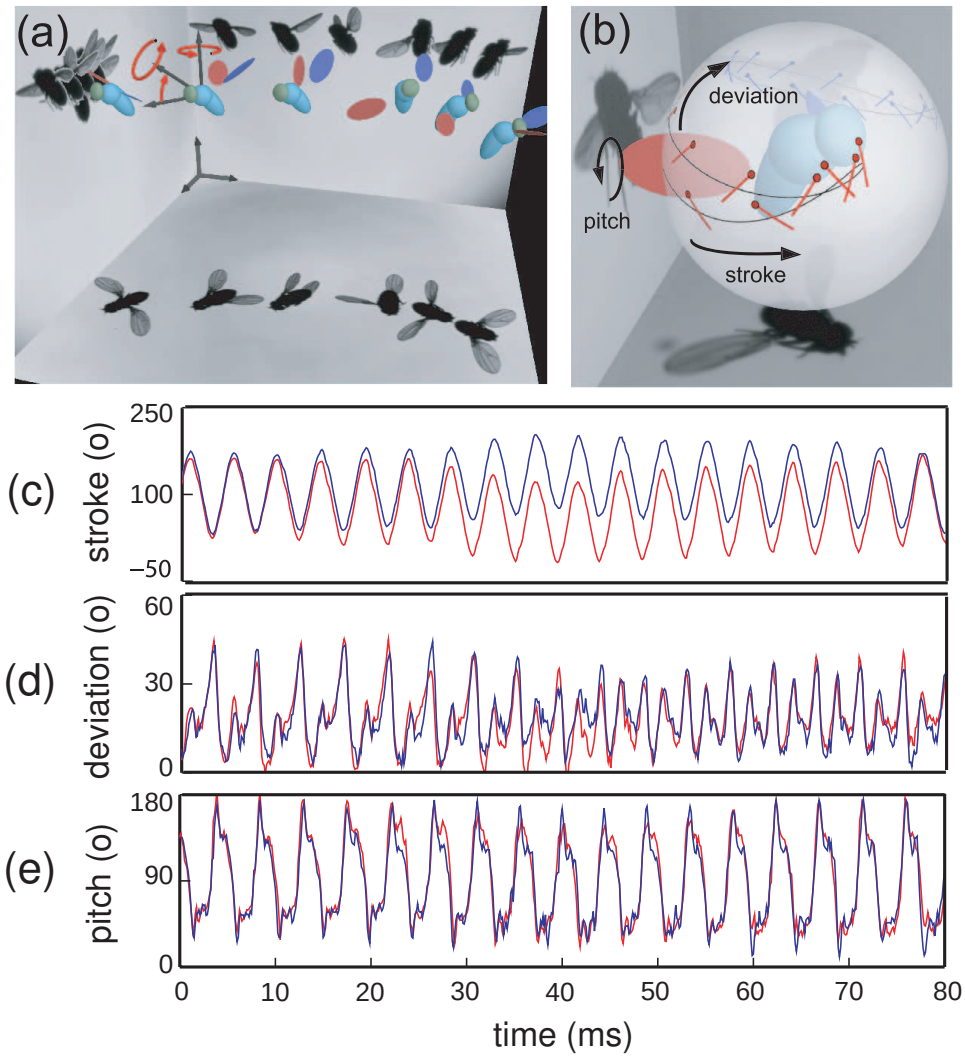

Figure 4.2: Body and wing motions during an extreme turning maneuver. (a) Reconstruction of the turn. The wing and body configuration for the fruit fly are captured by the three high-speed cameras, and selected snapshots are displayed on the side panels. We use a motion tracking algorithm to extract the wing and body posture for each frame, and these data are used to render the model insect. The insect is initially hovering on the right, and performs a rightward turn through about 120° while drifting to the left in this image. (b) Representation of wing motion. Each wing sweeps a path along a globe centered about its root on the body. (c-e) Wing orientation angles throughout the maneuver. Stroke angle is measured in the horizontal plane, deviation angle is the vertical excursion, and pitch angle is measured between the wing chord and the horizontal plane.

we use the simulation to compute the average torque during the initial wingbeats of the turn. We compare this torque to those generated by symmetrized kinematics. Two of three Euler angles are symmetrized to their right-left average, thus isolating the asymmetry in the third angle. This procedure indicates that changes in wing pitch account for the yaw torque generated to within about 10%.

To physically interpret how changes in pitch lead to yaw torque, we first note that the curve for right wing pitch is shifted upward relative to that of the left wing during the turn [(Fig. 4.2(e)]. This upward shift can be rationalized by considering its effect on aerodynamic forces on the right wing. During the forward stroke, the high value of wing pitch indicates the wing is more vertical and thus pushes off the air with a broad area exposed to the flow. During the backward stroke, the higher value of pitch indicates the wing is more horizontal, in effect slicing through the air. Thus, a uniform shift in wing pitch angle generates rowing or paddling motions that rotate the insect body.

4.5 Minimal Model of Turning Flight

We construct a physics-based model of turning dynamics. Combining all relevant yaw torques, the body rotational dynamics are described by

$$I\ddot{\psi} = N_{\text{aero}} \tag{4.1}$$

where I is the yaw moment of inertia of the insect body and N_{aero} is the aerodynamic torque on the insect. For wings that beat in a horizontal stroke plane, only the aerodynamic drag on the wings contributes to yaw torque. In general, the drag on each wing is proportional to the wings drag coefficient, $C_{\text{D}}(\alpha)$, times

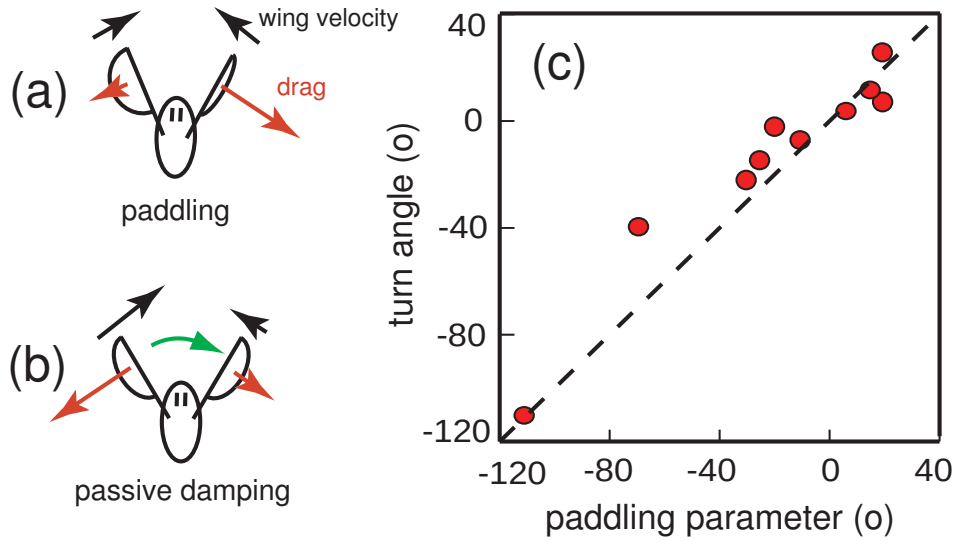

Figure 4.3: Minimal model of turning dynamics. (a) Paddling drives turns. In this top view schematic, a fly turns rightward by inclining its wings at different angles, thus generating differential drag (red arrows) on its wings. (b) Passive damping resists body rotations. As the wings beat during body rotation, their airspeeds are modified and thus induce a resistive drag on the wings. (c) Testing the model. The model predicts that the body turn angle is equal to the paddling parameter, a quantity related to the wing motions. By measuring the wing and body motions for 10 maneuvers, we verify the model. See text for model details.

the square of its speed relative to air. We consider the general case in which the right and left wing angles of attack may be different, and each wing beats with mean angular speed ω relative to the body. For an insect body rotating at angular velocity $\dot{\psi}$, the stroke-averaged net aerodynamic torque is found by summing each wings contribution:

$$N_{\text{aero}} \sim -C_{\text{D}}(\alpha_{\text{L}})\cdot(\omega+\dot{\psi})^2+C_{\text{D}}(\alpha_{\text{R}})\cdot(\omega-\dot{\psi})^2 \approx -C_{\text{D}}(\alpha_0)\cdot 4\omega\cdot\dot{\psi}+C'_{\text{D}}(\alpha_0)\cdot\omega^2\cdot\Delta\alpha. \quad (4.2)$$

Here, we have kept leading order terms in $\dot{\psi}$ and taken advantage of the linearity of the coefficient dependence on attack angle [6]: $C_{\text{D}}(\alpha) \approx C_{\text{D}}(\alpha_0)+C'_{\text{D}}(\alpha_0)\cdot(\alpha-\alpha_0)$, where $\alpha_0 = 45°$ and $C'_{\text{D}}(\alpha_0)$ is the slope at α_0. This aerodynamic torque has two components. The first is a damping torque, and it is proportional to the yaw velocity $\dot{\psi}$ with a damping coefficient β that depends on aerodynamic proper-

ties of the wings. The second is the torque due to the asymmetric wing motions, $N_{\text{fly}} = \gamma \cdot \Delta\alpha$, and it is proportional to $\Delta\alpha$ with a second aerodynamic constant γ. Combining Eqs. 4.1 and 4.2, we arrive at the yaw dynamical equation

$$I\ddot{\psi} = -\beta\dot{\psi} + \gamma \cdot \Delta\alpha. \tag{4.3}$$

Thus, the active torque exerted by the fly must act in concert with aerodynamic damping and inertia to generate body rotation.

As the insect drives the turn, its wings beat asymmetrically, as shown in Fig. 4.3(a), and torque is generated from unbalanced drag on the wings. For example, to turn rightward, the fly employs a higher average attack angle α on the right wing for the forward stroke and a higher α on the left wing for the backward stroke [2]. These rowing motions generate differential drag on the wings and thus produce the yaw torque, N_{fly}, that drives the body rotation. To stop the rotation, the insect need not apply an active counter-torque. If the wings beat symmetrically, $\Delta\alpha = 0$, so that $N_{\text{fly}} = 0$. The induced body rotation, however, introduces a difference in the wing velocities and hence a difference in the drag forces acting on the wings [13, 9, 10], as illustrated in Fig. 4.3(b). Then Eq. 4.3 reduces to $I\ddot{\psi} = -\beta\dot{\psi}$. Thus, an induced yaw rotation exponentially decays with a characteristic damping time of about two wing-beat periods, $I/\beta \approx 2T$.

4.6 Testing the Model

To provide a general test of the aerodynamic model, we ask how the paddling wing motions relate to the rotation of the body. In particular, to derive the total

turn angle of the body, we integrate Eq. 4.3 over the entire turn.

$$I \cdot \Delta\dot{\psi} = -\beta\Delta\psi + \gamma \int \mathrm{d}t\Delta\alpha \tag{4.4}$$

Here, the symbol Δ indicates the net change in each quantity. Once the maneuver is complete, the change in yaw velocity $\Delta\dot{\psi} = 0$. Solving Eq. 4.4 for the total angle through which the body turns yields

$$\Delta\psi = \frac{\gamma}{\beta} \int \mathrm{d}t\Delta\alpha = \omega \int \mathrm{d}t\Delta\alpha, \tag{4.5}$$

where ω is mean angular speed of the wings relative to the body. Thus, the model predicts that the stronger the paddling and the longer such motions are applied, the greater the body rotates.

To test this prediction, we use our videography apparatus to capture many instances of saccadic turns. We then use our motion tracking algorithm to extract the complete wing and body kinematics for 10 such sequences, and use these data to distill the paddling parameter, $\omega \int \mathrm{d}t\Delta\alpha$, during turns and the body turn angle, $\Delta\psi$. In Fig. 4.3, we plot the body turn angle against the paddling parameter and find that the model captures the overall trend in the relationship. This indicates that paddling and damping are the key physical factors in the dynamics of turning maneuvers.

4.7 Paddling Actuation Mechanism

At a level deeper, we next investigate how the paddling wing motions themselves arise. The following analysis was performed by Attila Bergou [2], and we point to our paper for modeling details. To address this, we combine our measurements of the wing pitching motion, an aerodynamic force model, and

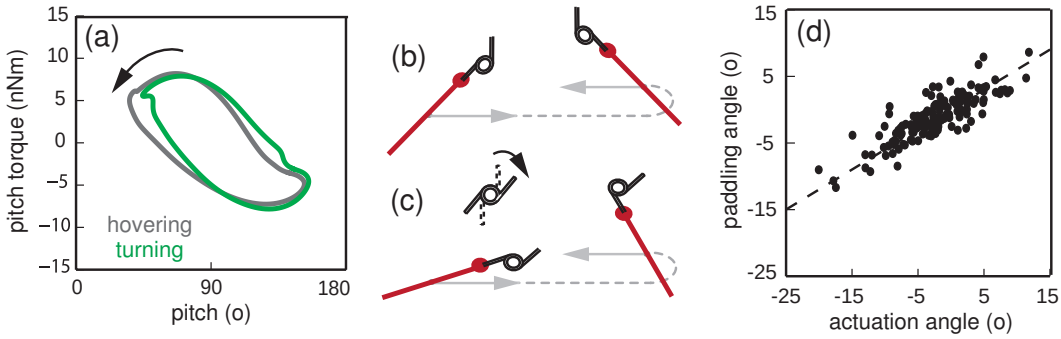

Figure 4.4: A biomechanical model of wing actuation. (a) Stress-strain relation for wing pitch. The pitch torque that the insect exerts is plotted against the pitch angle itself. During both hovering and turning flight, the torque exerted by the insect primarily acts like a viscoelastic brake that resists flipping due to inertial and aerodynamic forces. During turning, the mean pitch angle is biased to a pitch angle greater than 90°. (b-c) Biomechanical interpretation. The wing hinge or musculature acts like a viscoelastic (damped torsional spring) element that is biased to generate paddling motions. (d) The degree of paddling varies with the bias applied. The paddling angle is approximately one-half the bias angle (dashed line).

the Newton-Euler equations for the wing in order to extract the torque that the insect must exert to pitch its wing. As an analogy to a stress-strain curve for a material, this torque can be plotted against the pitch angle itself, as in Fig. 4.4(a). For the symmetric wing motions in hovering and the asymmetric paddling motions, this relation forms a loop which is traversed in a counter-clockwise sense. This direction of traversal indicates that work is being done on the insect to drive wing pitching rather than the insect doing work on the fluid. The energy extracted is equal to the area of this work-loop. With regard to wing pitching motions, this indicates that the wing hinge and musculature act as a brake that resist the inertial and aerodynamic torques that would flip the wing over. The wing pitching motions arise passively.

The difference between wing pitching during hovering and during a turn corresponds to a shift in the loop toward greater values of pitch [4.4(a)]. As

discussed above, greater pitch corresponds to paddling motions. In the context of wing actuation, this shift corresponds to a biasing of the angular position of the pitch brake. To couch this idea in a more quantitative model, consider the wing hinge and musculature as a damped torsional spring, as shown in the schematic of Figs. 4.4(b) and (c). The torque exerted by the insect is then $\tau = -\kappa\cdot(\eta-\eta_0)-C\cdot\dot{\eta}$, where η is the wing pitch angle, κ is the torsional spring constant, η_0 is the rest angle of the spring, and C defines the degree of damping. This viscoelastic behavior is called a Voigt model in the context of the mechanics of biological tissues . For hovering, $\eta_0 \approx 90^\circ$ so that the wings pitch symmetrically back and forth, as in 4.4(b). For turning, $\eta_0 \neq 90^\circ$ and asymmetric paddling motions drive body rotations, as shown in 4.4(c).

To test the validity of this picture, we combine the biomechanical model and the aerodynamic simulations to derive a relationship between the adjustment of the spring rest angle η_0 and the paddling motions this induces. The paddling angle quantifies the deviation of the wing pitch or angle of attack itself from 90°, while the actuation angle corresponds to the bias of η_0 from 90°. In Fig. 4.4(d), we plot the predicted relationship between these quantities as a dashed line, and data points correspond to experimentally measured wing-strokes. The theory is able to quantitatively account for the trend in the data.

Physically, this actuation model can be interpreted as a transmission system that converts flapping motions to flapping-plus-flipping motions. It is an active-passive hybrid system. It is passive in the sense that the insect need not invest power directly to the pitching degree-of-freedom but instead harvests power from the flapping motions. It is active in the sense that pitching motions can be modulated in a simple way to drive maneuvers.

The transmission system has two other nice properties. First, it eliminates the need to actuate on the time-scales of a wing-beat, a convenience and perhaps necessity for such animals in which the wing-beat period is as fast as neural time-scales. Though the wing motions themselves change within a wing-beat, the actuation need only be applied on the scale of an entire maneuver, say 10-20 wing-beats. Second, the system takes a relatively large actuation to a finer change in wing motion. The data and theory shown in Fig. 4.4(d) shows that is the base of the wing is biased by 10° then paddling motions of about 5° result. This down-gearing may be important considering the precision required for such a sensitive dependence of torque on wing motion modulation.

4.8 Why Paddle?

Given that their are numerous ways in which flies could generate yaw torque, what advantages does paddling offer? A possible answer is clear when one considers both lift and drag forces on flapping wings. If wing pitch or angle of attack is modulated, as during the idealized paddling shown in Fig. 4.5(a), drag becomes unbalanced but lift is not changed much. This becomes clear when one views the dependence of lift and drag coefficients on angle of attack, as plotted in Fig. 4.5(b) from a dynamically-scaled experiment [6]. Fruit flies typically beat their wings near an angle of attack of 45°, exactly where drag is most sensitive to changes in angle and lift is least sensitive. Thus, modulating attack angle recruits a large difference in drag while largely maintaining the lift needed to keep aloft.

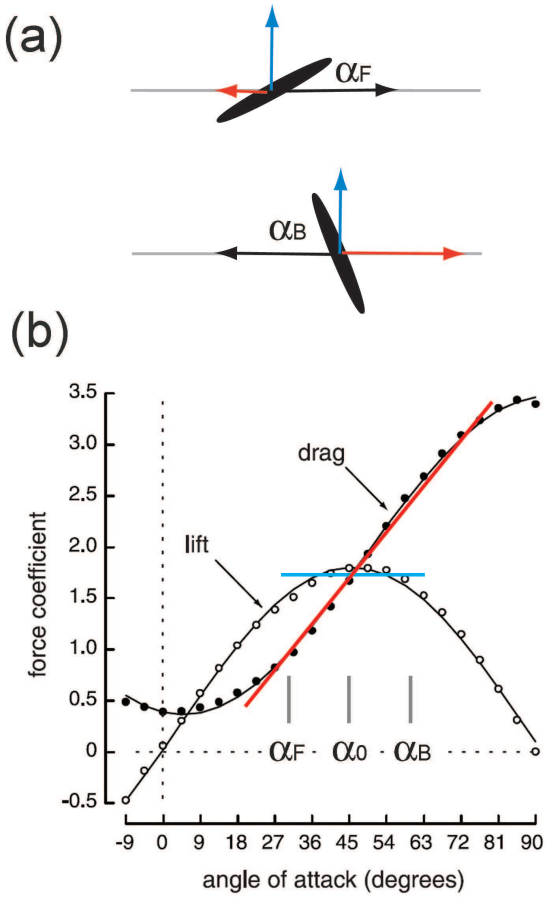

Figure 4.5: Paddling recruits drag to maneuver while largely maintaining lift. (a) Idealized paddling motions involve slicing and pushing. Each wing sweeps forward at low angle of attack and sweeps backward at a higher angle. (b) Lift and drag coefficients as a function of angle of attack [6]. By operating near an angle of attack of $45^{/}circ$ and adjusting this angle, insects can generate large drag differentials while largely keeping a constant lift.

4.9 Revisiting Previous Work

It is difficult to evaluate why our results differ from the previous study [7] of free-flight yaw turns in fruit flies. However, I have some thoughts on these differences that may shed light on the subtleties involved in understanding such problems. First, the lower time resolution and much lower spatial resolution of the earlier flight videos, combined with a manual motion tracking method, cer-

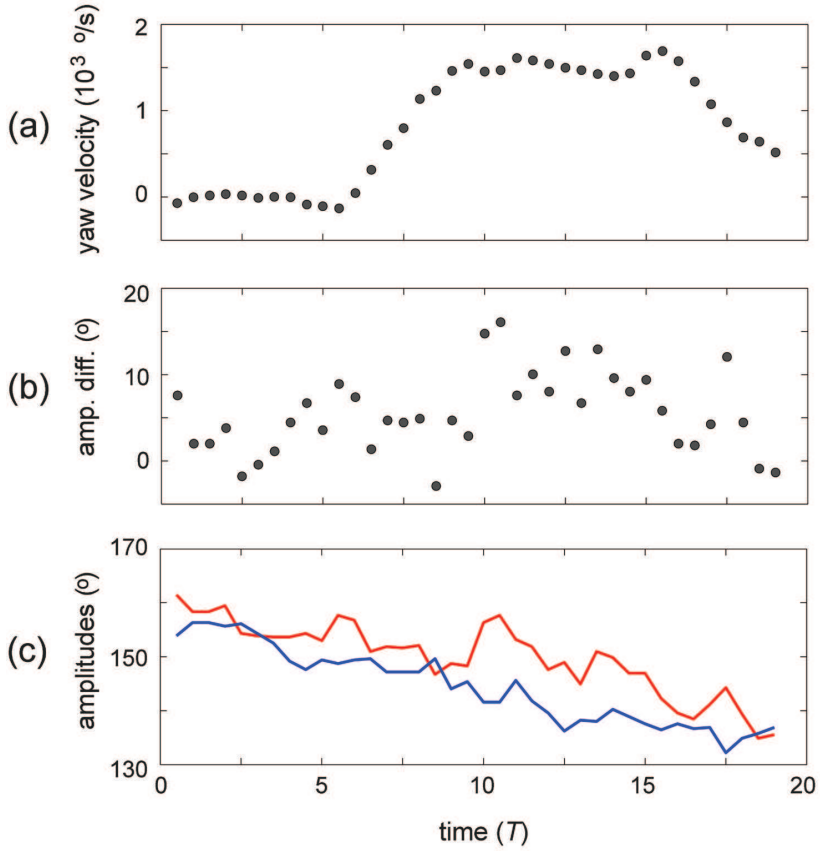

Figure 4.6: Re-evaluation of the 2003 study of saccadic turns in fruit flies [7]. The data in these plots have been manually digitized from the original study. (a) Yaw velocity during a representative saccade versus time measured in wingbeat periods T. (b) Difference between right and left stroke amplitudes. (c) Stroke amplitudes for the right (red) and left (blue) wings.

tainly made the kinematic data of lower quality than those presented here. The reported changes in stroke-plane angle and amplitude of 5° and smaller would certainly be difficult to resolve reliably. Second, these changes may well have occurred, but that does not mean that these changes are important to the aerodynamic mechanism driving turns. The previous study simply found some kinematic correlates between wing and body motion. Third, the previous study did suffer from one subtle but serious procedural flaw. In determining the torque generated by given wing motions, the researchers had the mechanical wings

flap as in the body frame, not as in the lab frame. Thus, the wing-body coupled motion was ignored. Our results show that this coupling is crucial in dictating the body dynamics and gives rise to a resistive torque during turns.

In an attempt to understand some of these differences in more detail, I reviewed some of the kinematic data gathered in the earlier study. The central claim of the paper is that the torque that these insects exert must primarily overcome the inertia of the body. The researchers confirm this in part by showing that the modulation of the wing-strokes correlates with yaw torque and with yaw acceleration. I have been unable to confirm this in analyzing the maneuvering kinematics presented in the paper. Fig. 4.6(a-c) shows data I have digitized from the earlier work. Though the data is noisy, the difference in wing-stroke amplitudes seems to correlate with yaw velocity, not yaw acceleration. This is indicative of a heavily damped system in which driving torque must overcome resistive torque that is proportional to velocity.

Finally, in revisiting the wing angle of attack data, I find that the original data does show paddling-like wing motions. In particular, as in our data sets, the curve for the right wing angle of attack is consistently shifted upwards relative to that for the left wing. However, given the uncertain errors, it is difficult to evaluate this idea more quantitatively.

4.10 Supporting Information

The lighting used in these experiments is chosen so as to avoid over-stimulating the insects. The spectral data of Fig. 4.7 shows that the back-lighting LEDs are peaked to emit light at a frequency band to which insects are insensitive [3] but

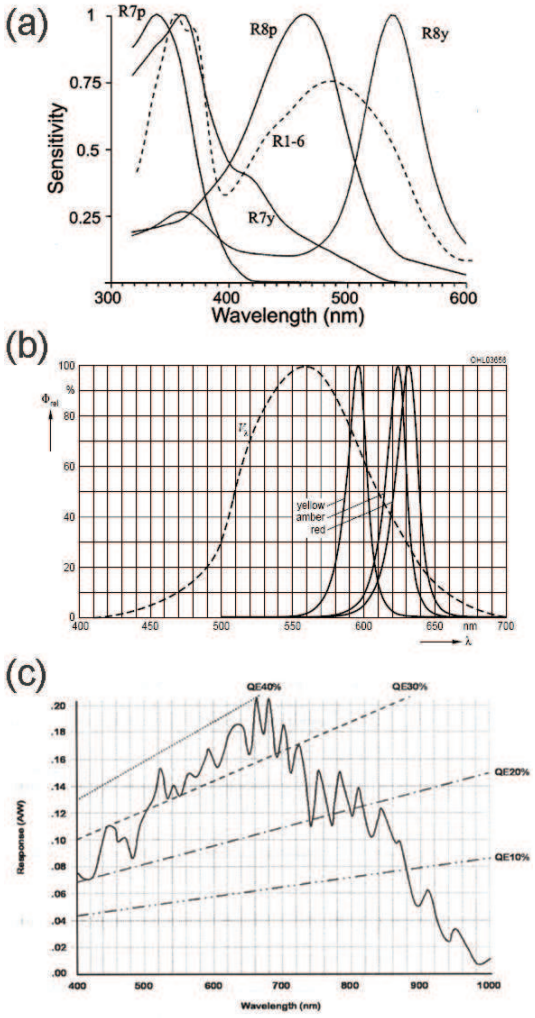

Figure 4.7: Spectral response for (a) the house fly [3] and (c) the Phantom v7.1 high-speed camera. (b) The emission spectrum for the high-power LED lights (Diamond Dragon, OSRAM). Though complete spectral data is not available for fruit flies, the house fly and fruit fly have receptor cells of similar spectral sensitivity [3]. Notice that the cameras are most sensitive to red, while the fly visual sensitivity rapidly drops off above 600 nm. The lighting for these experiments is done with LEDs that peak at about 630 nm and have dropped to less than 5% of their maximal sensitivity by 600 nm.

the cameras are highly sensitive. This may be important in future studies aimed at exploring the visual control of flight.

BIBLIOGRAPHY

[1] J. A. Bender and M. H. Dickinson. Visual stimulation of saccades in magnetically tethered drosophila. *J. Exp. Biol.*, 209:3170–3182, 2006.

[2] A. J. Bergou, L. Ristroph, J. Guckenheimer, I. Cohen, and Z. J. Wang. *Phys. Rev. Lett.*, 104:148101, 2010.

[3] A. D. Briscoe and L. Chittka. The evolution of color vision in insects. *Ann. Rev. Entomol.*, 46:471–510, 2001.

[4] T. S. Collett and M. F. Land. Visual control of flight behavior in the hoverfly, syritta pipiens l. *J. Comp. Physiol. A*, 99:1–66, 1975.

[5] M. H. Dickinson. The initiation and control of rapid flight maneuvers in fruit flies. *Integr. Comp. Biol.*, 45:274–281, 2005.

[6] M. H. Dickinson, F.-O. Lehmann, and S. Sane. Wing rotation and the aerodynamic basis of insect flight. *Science*, 284:1954–1960, 1999.

[7] S. N. Fry, R. Sayaman, and M. H. Dickinson. The aerodynamics of free-flight maneuvers of drosophila. *Science*, 300:495–498, 2003.

[8] M. Heisenberg and R. Wolf. The sensory-motor link in motion-dependent flight control of flies. In *Visual Motion and its Role in the Stabilization of Gaze*, pages 265–283, Amsterdam, 1993. Elsevier.

[9] T. Hesselberg and F.-O. Lehmann. Turning behavior depends on frictional damping in the fruit fly drosophila. *J. Exp. Biol.*, 210:4319–4334, 2007.

[10] T. Hesselberg and F.-O. Lehmann. Wingbeat time and the scaling of passive rotational damping in flapping flight. *Science*, 324:252–255, 2009.

[11] M. Mayer, K. Vogtmann, B. Bausenwein, R. Wolf, and M. Heisenberg. Flight control during 'free yaw turns' in drosophila melanogaster. *J. Comp. Physiol. A*, 163:389–399, 1950.

[12] L. Ristroph, G. J. Berman, A. J. Bergou, Z. J. Wang, and I. Cohen. Automated hull reconstruction motion tracking (hrmt) applied to sideways maneuvers of free-flying insects. *J. Exp. Biol.*, 212:1324–1335, 2009.

[13] R. F. Stengel. *Flight dynamics*. Princeton University Press, Princeton, 2004.

[14] L. F. Tammero and M. H. Dickinson. he influence of visual landscape on the free flight behavior of the fruit fly drosophila melanogaster. *J. Exp. Biol.*, 205:327–343, 2002.

CHAPTER 5

YAW STABILIZATION IN FRUIT FLIES

5.1 Summary

Just as the Wright brothers implemented controls to achieve stable airplane flight, flying insects have evolved behavioral strategies that ensure recovery from flight disturbances[1]. Pioneering studies performed on tethered and dissected insects demonstrate that the sensory, neurological, and musculoskeletal systems play important roles in flight control. Such studies, however, cannot produce an integrative model of insect flight stability since they do not incorporate the interaction of these systems with free-flight aerodynamics. We directly investigate control and stability through the application of torque impulses to freely-flying fruit flies (*Drosophila melanogaster*) and measurement of their behavioral response. High-speed video and a new motion tracking method capture the aerial "stumble", and we discover that flies respond to gentle disturbances by accurately returning to their original orientation. These insects take advantage of a stabilizing aerodynamic influence and active torque generation to recover their heading to within 2° in less than 60 milliseconds. To explain this recovery behavior, we form a feedback control model that includes the fly's ability to sense body rotations, process this information, and actuate the wing motions that generate corrective aerodynamic torque. Thus, like early man-made aircraft and modern fighter jets, the fruit fly employs an automatic stabilization scheme that reacts to short time-scale disturbances.

[1]The work presented in this chapter is modified with permission from Ristroph *et al.*, *PNAS*, **107**, 4820-4824 (2010).

Figure 5.1: Three-dimensional reconstruction of a recovery maneuver. Three orthogonal high-speed cameras capture 35 frames per wing-beat, and the still images shown on the side panels are spaced by about four wing-beats. The corresponding three-dimensional wing and body configurations extracted from the images are displayed on a computer-generated model of the fruit fly (body length 2.5 mm). As the fly descends from left to right, we apply a magnetic field (red looped arrow) for one wing-beat that torques the ferromagnetic pin (bronze rod) glued to its back and reorients the insects flight heading. The insect responds to the flight perturbation by making a corrective turn that lasts several wing-beats.

5.2 Insect Flight Stability and Control

Locomotion through natural environments demands mechanisms that maintain stability in the face of unpredictable disturbances. Behavioral strategies play a particularly important role in controlling the flight of insects [10, 32, 24, 15, 16, 23, 7], because even gentle air currents can cause large disruptions to the intended flight path. Insects must also contend with the intrinsic instability of flapping flight [33, 30] and the large fluctuations in aerodynamic forces caused

by slight variations in wing motions [12, 13]. Corrective behavior often takes advantage of vision [10, 32]. For fruit flies, however, reaction time to visual stimuli is at least 10 wing-beats [17], so these insects must employ faster sensory circuits to recover from short time-scale disturbances and instabilities. To probe this fast control strategy, we devised an experimental method that imposes impulsive mechanical disturbances [23, 20] to flying insects while allowing us to measure relevant aspects of flight behavior. We first glue tiny ferromagnetic pins to fruit flies and image their free flight using three orthogonally-oriented high-speed video cameras. See Methods and online Supporting Information (SI). When a fly enters the filming volume, an optical trigger detects the insect, initiates recording, and activates a pair of Helmholtz coils that produce a magnetic field. The field and pin are both oriented horizontally, so the resulting torque on the pin reorients the yaw, or heading angle, of the insect (Fig. 5.1). We then use a new motion tracking technique to extract the three-dimensional body and wing motions [25]. The videos and extracted flight data reveal that these insects respond to such mechanical perturbations by attempting to correct their course, and this reaction depends on the strength of the disturbance.

5.3 Stabilization Response of the Fruit Fly

By conducting experiments at various values of the applied torque, we induce different maximal deflections in the yaw angle, $\Delta\psi_{\max}$. As diagrammed in the inset of Fig. 5.2, we characterize the response by measuring the error, $\Delta\psi_{\text{err}}$, which is the difference between the final and initial yaw angles. In all 23 trials, the insects exhibit corrective responses such that $\Delta\psi_{\text{err}} < \Delta\psi_{\max}$, as shown in Fig. 5.2. Impressively, for gentle disturbances, the insects correct their heading

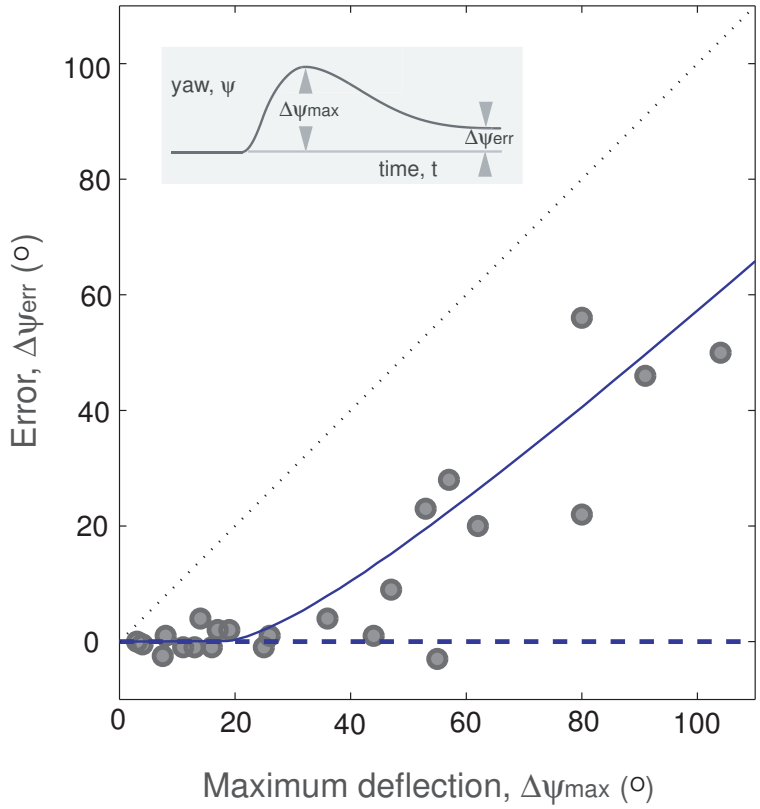

Figure 5.2: Accuracy of the corrective response. Inset: For each trial, the error $\Delta\psi_{\text{err}}$ (final minus initial yaw) and maximum induced deflection $\Delta\psi_{\text{max}}$ are measured from the yaw dynamics. Main figure: The error is plotted against the deflection for 23 experiments. The dashed blue horizontal line is the predicted perfect correction from a linear control model, and the solid blue line is the result of a nonlinear model. See text for details of both models.

nearly perfectly, with a mean of 2° (15 trials with $\Delta\psi_{\text{max}} < 45°$). For stronger perturbations, however, the corrective responses are not sufficient to return the flies to their original heading. For cases of both inaccurate and accurate correction, the insects exhibit a stereotypical response in which specific changes in the motions of the wings drive the reorientation of the body.

The yaw dynamics, $\psi(t)$, for a case in which the fly accurately corrects its heading is visualized in Fig. 5.3A and plotted in Fig. 5.3B. At time $t = 0$, the field is turned on for 5 milliseconds (vertical pink stripe), or about one wing-beat pe-

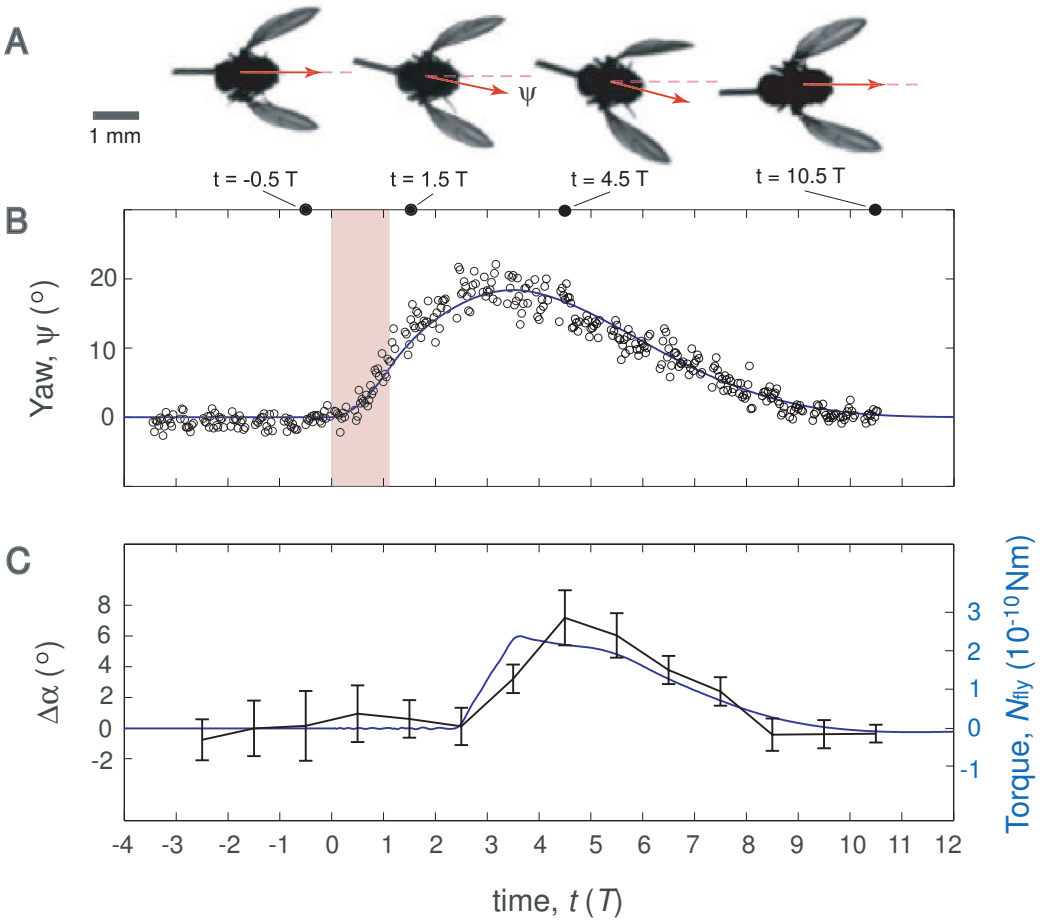

Figure 5.3: Body and wing motions for a case of accurate correction. (A) Top-view images of the insect before the perturbation, during the induced rightward rotation, during the corrective turn leftward, and after accurate recovery. The yaw angle, or heading, is shown as a red arrow, and the wings are moving forward in each image. The differences in right and left wing area in the third image indicate differences in angles of attack that drive the corrective turn. (B) Yaw angle as a function of time measured in wing-beat periods, T = 4.5 ms. The red stripe indicates the 5 ms during which the perturbing torque, N_{ext} = 0.8×10^{-9} N·m, is applied. The yaw is experimentally measured (open circles), and a control model (blue curve) is fit to the experimental data. The parameters used for the fit are: $I = 0.6 \times 10^{-13}$ kg·m^2, $\beta = 1.0 \times 10^{-11}$ kg·m^2·s^{-1}, Δt = 2.5 T, $K_{\text{P}} = 5.0 \times 10^{-10}$ kg·m^2·s^{-2}, $K_{\text{D}} = 4.1 \times 10^{-12}$ kg·m^2·s^{-1}. See text for description of the model (Eqs. 1-4). (C) The attack angle difference between wings averaged over each wing-beat, $\Delta\alpha$, is plotted in black (mean and standard error of the mean). These data are compared to the torque predicted by the model (blue curve).

riod, T = 4.5 ms. In about three wing-beats, the fly experiences its maximal deflection of $\Delta\psi_{\max}$ = 19°, and by the recovery time Δt_{rec} = 10 T or 45 ms, it has recovered its orientation to within 2° of the original yaw. To reorient its body, the fly induces differences between the right and left wing motions, thus generating aerodynamic torque A recent analysis of free-flight turning maneuvers of fruit flies indicates that these insects generate yaw torque by asymmetrically adjusting the wing angles of attack, α, defined as the inclination angle of each wing relative to its velocity [5]. Qualitatively, these differences can be seen in the top-view stills from the flight videos, as shown in Fig. 5.3A. The insect beats its wings back-and-forth, and these images capture the wings as they move forward. In the third image, the right and left wings have different projected areas due to different attack angles. When the attack angle on one wing is greater than the other, the larger area presented to the flow induces a greater drag force, and this unbalanced drag causes the insect to rotate [5]. We quantify the asymmetric rowing wing motions by measuring the complete wing kinematics [25], and we verify that fruit flies drive yaw corrective maneuvers by differentially varying wing angle of attack. Specifically, in Fig. 5.3C, we plot the difference between the right and left wing attack angles averaged over each wing beat, $\Delta\alpha$ (black data). Prior to the perturbation and for the first three wing-beats after the disturbance, $\Delta\alpha$ = 0, indicating that the wings beat symmetrically. After this initial delay, asymmetries in the wing motions appear for about five wing-beats, indicating the insect is actively generating corrective torque. The accuracy of the recovery indicates that a refined control strategy underlies the response of fruit flies to in-flight perturbations.

5.4 Aerodynamic Model of Response

To reveal this strategy, we construct a physics-based model of the observed behavioral response. Combining all relevant yaw torques, the body rotational dynamics are described by

$$I\ddot{\psi} = N_{\text{aero}} + N_{\text{ext}} \tag{5.1}$$

where I is the yaw moment of inertia of the insect body, N_{aero} is the aerodynamic torque on the insect, and N_{ext} is the applied torque due to the magnetic field. For wings that beat in a horizontal stroke plane, only the aerodynamic drag on the wings contributes to yaw torque. In general, the drag on each wing is proportional to the wings drag coefficient, $C_{\text{D}}(\alpha)$, times the square of its speed relative to air. We consider the general case in which the right and left wing angles of attack may be different, and each wing beats with mean angular speed ω relative to the body. For an insect body rotating at angular velocity $\dot{\psi}$, the stroke-averaged net aerodynamic torque is found by summing each wings contribution (SI):

$$N_{\text{aero}} \sim -C_{\text{D}}(\alpha_{\text{L}})\cdot(\omega+\dot{\psi})^2 + C_{\text{D}}(\alpha_{\text{R}})\cdot(\omega-\dot{\psi})^2 \approx -C_{\text{D}}(\alpha_0)\cdot 4\omega\cdot\dot{\psi} + C'_{\text{D}}(\alpha_0)\cdot\omega^2\cdot\Delta\alpha. \tag{5.2}$$

Here, we have kept leading order terms in $\dot{\psi}$ and taken advantage of the linearity of the coefficient dependence on attack angle: $C_{\text{D}}(\alpha) \approx C_{\text{D}}(\alpha_0) + C'_{\text{D}}(\alpha_0)\cdot(\alpha-\alpha_0)$, where $\alpha_0 = 45^\circ$ and $C'_{\text{D}}(\alpha_0)$ is the slope at α_0. This aerodynamic torque has two components. The first is a damping torque, and it is proportional to the yaw velocity $\dot{\psi}$ with a damping coefficient β that depends on aerodynamic properties of the wings. The second is the torque due to the asymmetric wing motions, $N_{\text{fly}} = \gamma\cdot\Delta\alpha$, and it is proportional to $\Delta\alpha$ with a second aerodynamic constant γ. Combining Eqs. 5.1 and 5.2, we arrive at the yaw dynamical equation

$$I\ddot{\psi} = -\beta\dot{\psi} + \gamma\cdot\Delta\alpha + N_{\text{ext}} \tag{5.3}$$

Thus, the active torque exerted by the fly must act in concert with aerodynamic damping and inertia to restore body orientation.

To physically interpret these results, first consider the scenario just after the perturbation is applied. Here, the wings beat symmetrically, $\Delta\alpha = 0$, so that $N_{\text{fly}} = 0$. The induced body rotation, however, introduces a difference in the wing velocities and hence a difference in the drag forces acting on the wings [29, 18, 19], as illustrated in Fig. 5.4A,B. Then Eq. 5.3 reduces to $I\ddot{\psi} = -\beta\dot{\psi}$. Thus, an induced yaw rotation exponentially decays with a characteristic damping time of about two wing-beat periods, $I/\beta \approx 2T$ (SI). This time-scale is consistent with the decay of yaw velocity during the few wing-beats after the applied perturbation (Fig. 5.3B). As the insect recovers, its wings beat asymmetrically, as shown in Fig. 5.4C,D, and torque is generated from unbalanced drag on the wings. For example, to turn rightward, the fly employs a higher average attack angle α on the right wing for the forward stroke and a higher α on the left wing for the backward stroke [5]. These rowing motions generate differential drag on the wings and thus produce the yaw torque, N_{fly}, that drives the corrective body rotation.

5.5 Feedback Control Model of Response

The ability to adjust their response for perturbations of different strengths (Fig. 5.2) suggests that these insects sense their body motion and use this information to determine the corrective response. In fact, flies are equipped with a pair of small vibrating organs called halteres that act as gyroscopic sensors [24]. Anatomical, mechanical, and behavioral evidence indicates that the hal-

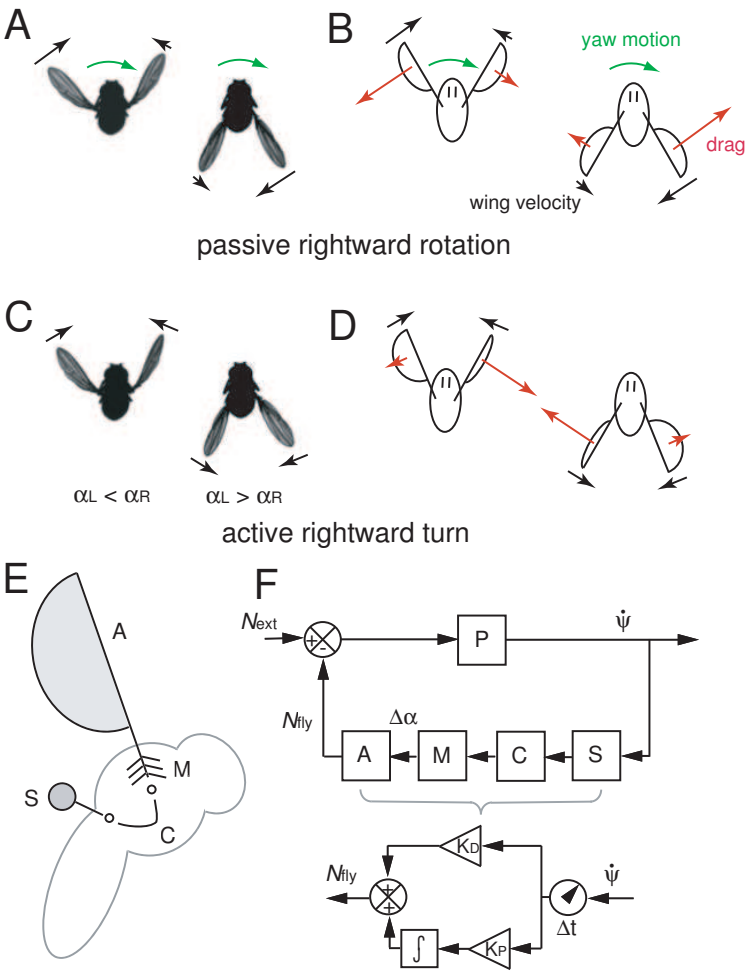

Figure 5.4: Physical and biological elements of the flight control model. (A and B) Aerodynamics of symmetric flapping flight during body rotation. Top-view images of the fly as it is rotated to its right by the perturbing torque show that the insect continues to beat symmetrically. The imposed rotation induces differences in wing velocity that generate unbalanced drag on the wings. (C and D) Active steering is driven by differences in wing angles of attack. To turn rightward, the insect assumes different pitch angles for the right and left wings that generate an unbalanced drag-based torque. (E) The haltere organs (S) sense body rotations, the neural controller (C) processes this information, and the flight motor (M) drives the wing motions that generate corrective aerodynamic torque (A). (F) Information flow diagram for the insect flight control model. The upper circuit describes the feedback loop used for correction, and the lower circuit shows the detailed control model. After an initial time delay, a term that is proportional to the sensed yaw rate signal and a term that integrates this signal are added to determine the output torque exerted by the fly.

teres serve as detectors of body angular velocity that quickly trigger muscle action [24, 7, 27]. These findings suggest that these insects drive their corrective response using an auto-stabilizing feedback loop in which the sensed angular velocity serves as the input to the flight controller. As diagrammed in Fig. 5.4E, the velocity is sensed by the halteres (S), processed by a neural controller (C), and transmitted by the flight motor (M) into specific wing motions that generate aerodynamic torque (A). In the top control diagram of Fig. 5.4F, the loop is triggered when an external torque, N_{ext}, induces a yaw velocity, $\dot{\psi}$, that is determined by the physics (P) of a damped, inertial body. The active torque exerted by the insect, N_{fly}, feeds back to determine the yaw dynamics (Eq. 5.3) and thus closes the loop.

A minimal linear control model [3] that guarantees perfect correction (dashed blue horizontal line in Fig. 5.2) in response to short-lived disturbances requires that the exerted torque contain a term proportional to the integral over time of the sensed angular velocity (SI). However, we find that a pure integrator fails to account for the fast recovery time observed in the flight data. By adding a term that is proportional to the angular velocity itself, we arrive at a good match to the yaw data, as shown by the model fit shown in Fig. 5.3B (blue curve). This model is a proportional-derivative (PD) scheme [3] that controls yaw angle using a yaw-rate sensor, and the corrective torque can be written as:

$$N_{\text{fly}}(t) = K_{\text{P}}\psi(t - \Delta t) + K_{\text{D}}\dot{\psi}(t - \Delta t). \tag{5.4}$$

Here, K_{P} and K_{D} are gain constants and Δt is the response delay time that we measure to be 2-5 wing-beat periods. This loop delay may reflect both neural latency and inertia of the sensors and motor [27, 8]. A diagram of this control scheme is shown in the bottom of Fig. 5.4F. In Fig. 5.3C, we overlay the torque, N_{fly}, predicted by Eq. 5.4 on the measured $\Delta\alpha$ data and find a strong agreement

between the model and experiment. Furthermore, both curves remain positive throughout the corrective maneuver, which reflects a simple strategy for linearly damped systems: to recover, the fly need only counter the perturbing impulse with an impulse of equal strength but opposite direction. To prove this, we integrate Eq. 5.3 over time to arrive at

$$I \cdot \Delta\dot{\psi} = -\beta\Delta\psi + \int \mathrm{d}tN_{\mathrm{fly}} + \int \mathrm{d}tN_{\mathrm{ext}} \tag{5.5}$$

where the symbol Δ indicates the net change in each quantity. Because the system is damped and all torques act over finite periods of time, the change in yaw velocity $\Delta\dot{\psi} = 0$. Perfect recovery implies $\Delta\psi = 0$, which requires that $\int \mathrm{d}tN_{\mathrm{fly}} = -\int \mathrm{d}tN_{\mathrm{ext}}$. Thus, accurate recovery simply requires a counter-impulse of equal magnitude to the perturbing impulse. These insects employ this strategy and do not brake the perturbing rotation nor their self-induced corrective rotation but instead take advantage of aerodynamic damping to come to each stop.

5.6 Testing the Control Model

The interplay of active and passive torques also sets the overall time-scale for recovery. Using the flight control model with average system parameters Δt, T, I, K_{P}, and K_{D}, the control model predicts that the total recovery time, Δt_{rec}, rises sharply and then plateaus for increasing imposed deflections, as shown by the dashed blue curve in Fig. 5.5. The experimentally measured recovery times confirm this trend, and this agreement indicates that the model is robust, with system parameters varying by ±15% among individuals.

Finally, the increasing error for stronger disturbances (Fig. 5.3) may reflect

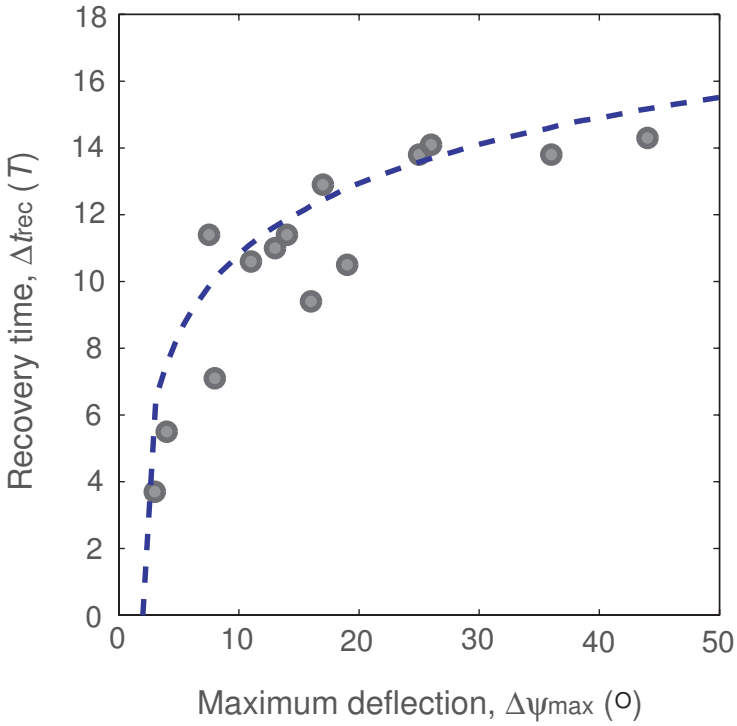

Figure 5.5: Recovery time, Δt_{rec}, increases for stronger perturbations. Here, Δt_{rec} is plotted for cases of accurate correction, and the model prediction is the dashed blue curve. The theoretical curve marks the total time to return to within 2° of the original yaw angle and is generated using the mean parameter values extracted from fits to trials of accurate recovery: $I = 0.9 \times 10^{-13}$ kg·m^2, $\beta = 0.9 \times 10^{-11}$ kg·m^2·s^{-1}, $\Delta t = 3.5$ T, $K_{\text{P}} = 5.9 \times 10^{-10}$ kg·m^2·s^{-2}, $K_{\text{D}} = 5.3 \times 10^{-12}$ kg·m^2·s^{-1}

.

sensor saturation. Specifically, we form a model that modifies the controller of Eq. 5.4 such that the sensors can only register velocities up to a maximum of $\dot{\psi} = 2500°/\text{s}$, a hypothesis consistent with the strong nonlinear mechanical response of vibratory gyroscopes [2]. This nonlinear model gives the solid blue error curve in Fig. 5.2 that accounts for both the accurate and inaccurate responses. The agreement between the model prediction and the experimental data indicates that this simple model based on sensor saturation is sufficient to explain why fruit flies are unable to accurately recover from strong perturbations.

5.7 Discussion and Predictions

These models reveal the physical and biological aspects of yaw auto-stabilization in fruit flies. Future experiments that modify the orientations of the magnetic coils and pin will investigate the control of pitch and roll. Studies that combine such perturbations will elucidate how these insects coordinate their response to complex disturbances. Aerodynamically, these experiments on freely-flying insects demonstrate the critical importance of considering the coupled wing and body motions for studies of flight behavior. In particular, this coupling gives rise to a strong damping of yaw rotation [18, 19], and our results show that auto-stabilizing fruit flies use this damping rather than active braking to stop body rotation. This important effect is, of course, entirely removed in studies that rigidly tether insects [17]. Even in experimental preparations that loosely confine the motion of insects [21, 4], turning kinematics are different from those observed in free-flight studies [12, 5, 31]. These discrepancies indicate that restrictive preparations interfere with flight behavior, and the results of such studies must be interpreted in light of this influence.

Biologically, our findings lead to novel hypotheses regarding the roles of the systems that underlie flight control in the fruit fly. First, our results suggest that the halteres are unable to detect high rotation rates of the body, and recordings from sensory neurons should reflect this limitation [11]. Second, we predict that the neural circuitry between the halteres and wing muscles [8] transmits a position- and rate-driven signal. Determination of the wiring and firing of these neurons would offer insight into the neurological basis of signal integration and summation [26]. Third, we find that wing orientation adjustments during auto-stabilization are remarkably similar to those used for voluntary turns

[5] and hypothesize that they result from the same musculoskeletal elements [8]. We stress, however, that our experiments strictly address the fruit fly's reflexive turning response to mechanical stimuli rather than visually-induced turning behavior. The interaction between the haltere control loop and visual system loops in structuring such voluntary turns remains an open problem [8]. Nevertheless, we expect that the aerodynamic and behavioral models presented here will be key components of general flight navigation models for the fruit fly.

5.8 Broader Implications

Flight control principles uncovered in this model organism may also apply more broadly, and this work provides a template for future studies aimed at determining if other animals employ flight auto-stabilization. The control strategies across different animals are likely to share common features, because the physics of body rotation is similar across many animals during flapping-wing flight [19]. Additionally, animals that lack halteres may use functionally-equivalent mechanosensory structures such as antennae [28]. Finally, the control architecture of the fruit fly offers a blueprint for stabilization of highly-maneuverable flapping-wing flying machines [34].

For fixed-wing machines, the need to overcome instabilities spurred the invention of auto-stabilizing systems by 1912, only 9 years after the Wright brothers first manually controlled airplane flight [1, 35]. The development of such automatic steering systems also led to the first formal description of proportional-integral-derivative (PID) control schemes [22] and advanced gyroscopic sensor technology [1]. The fruit flys auto-stabilization response is well-modeled by a

simple PD scheme that receives input from gyroscopic halteres, and, like airplanes [29, 1], uses fine adjustment of wing orientation to generate corrective torques. Roughly 350 million years after insects took flight [14], man converged to this solution for the problem of flight control and joined animals in the skies.

5.9 Summary of Methods

Videography. As described in our earlier paper [25], three synchronized, orthogonal high-speed cameras record at 8000 frames per second. Each camera is back-lit by a bright red light-emitting diode. Recording is initiated by an optical detector system that triggers when an insect flies in the region of interest.

Magnetic torque perturbation. The optical detector also triggers a circuit that drives a 4-amp direct current pulse of width 5 ms through paired Helmholtz coils placed inside a clear flight chamber. The magnetic field strength is on the order of 10^{-2} Tesla, or 10^3 times stronger than the Earth's field.

Motion tracking. The three-dimensional body and wing coordinates are extracted from the flight videos using a recently-developed method [25]. The yaw angle is measured directly, and we extract the wing angle of attack difference, $\Delta\alpha$, from the measured wing coordinates with an accuracy of about 3°. Though the corrective turns are accompanied by changes in other aspects of the wing motions (i.e., stroke amplitude), a recent analysis implicates attack angle difference as the aerodynamically relevant parameter [5]. We average this parameter over each wing-beat, because the modulation of $\Delta\alpha$ occurs over longer timescales [5]. For the $\Delta\alpha$ data of Fig. 5.3C, the vertical bars indicate the standard error of the mean taken over the 35 measurements per wing-beat and thus reflect

both measurement error and actual intra-wing-beat variation. The magnitude, duration, and variation of the $\Delta\alpha$ data in these experiments are similar to those measured for free-flight turns [5].

Animal preparation. During each day of experiments, about 40 common fruit flies (*D. melanogaster*) from out-bred laboratory strains are first selected for strong flight capability. A carbon steel wire 1.5 mm long and 0.006 inch in diameter is carefully glued to the notum, the dorsal surface of the insect's thorax. The attached pins weight is 15-20% that of the typical fly, and we analyze only sequences in which the pin does not interfere with the motion of the wings.

Control experiments. Videos that capture the flight of insects whose pins had fallen off show no change in behavior upon application of the magnetic field. Also, videos captured in a darkened laboratory show no qualitative or quantitative difference in corrective behavior.

Models. The Simulink software package for MATLAB (The Mathworks Inc., Natick, MA USA) numerically integrates the linear and nonlinear delay differential equations. For each sequence, we calculate approximate values for the morphological and aerodynamic parameters I and β. The value of the delay time Δt is determined directly from the time-course of the measured $\Delta\alpha$ data. We then select the value of N_{ext} that yields the measured maximal deflection of yaw. Finally, the best-fit match to the complete time-course of yaw determines the values of the free parameters K_{P} and K_{D}. All model parameters vary by ±15% among different individuals.

Figure 5.6: A common fruit fly (*D. melanogaster*) with ferromagnetic pin glued to the dorsal surface of its thorax is suspended by a magnetized sewing needle. The pin is 1.5 mm long. In free-flight, the insect is perturbed by application of a magnetic field that induces a torque on the pin.

5.10 Supporting Information

Animal preparation and protocol. During each day of experiments, about 40 common fruit flies (*D. melanogaster*) from out-bred laboratory strains are first selected for strong flight capability. Each fly is then chilled for 1 to 2 minutes, and a 1.5 mm cutting of 0.006 in.-diameter carbon steel wire (Gordon Brush Co., Commerce, CA USA) is carefully glued to the dorsal surface of the insects thorax. The adhesive (Norland Optical, New Brunswick, NJ USA) is cured for 20 s under ultraviolet light. See Fig. 5.6 for a photograph of a pinned fly. The insects are then deprived of food and water for approximately 2 hours before being inserted into the flight chamber. Filming is then conducted for up to 6 hours.

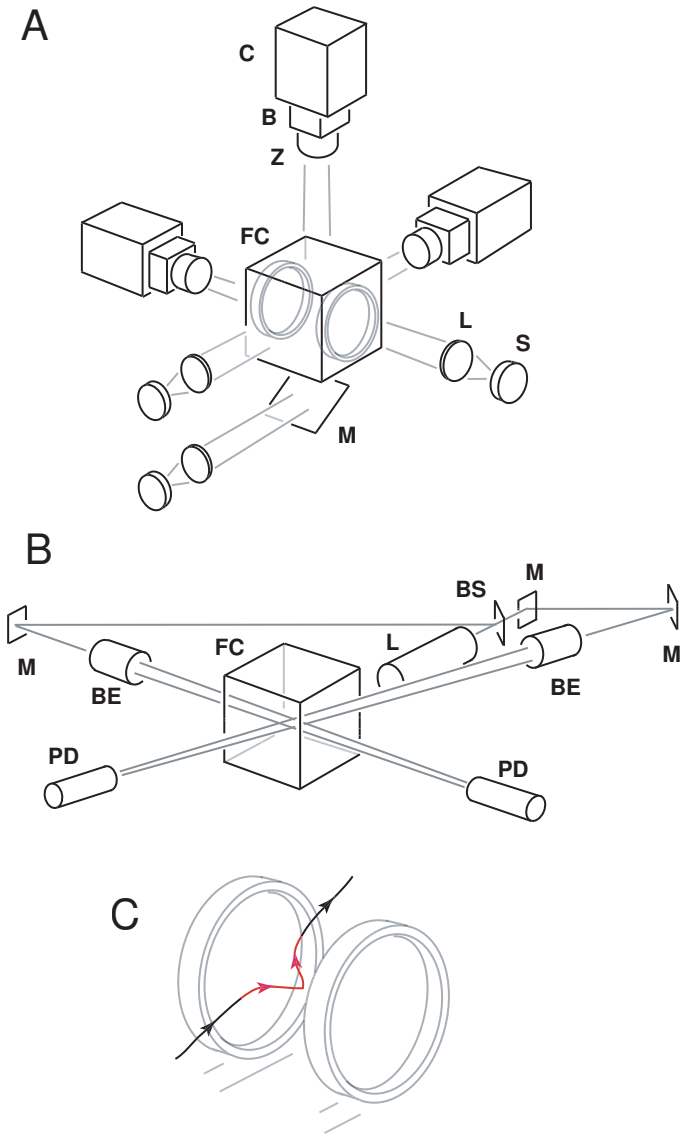

Figure 5.7: Schematic of the flight perturbation and videography apparatus. (A) Three high-speed cameras (C) focus on a cubic volume (2 cm side length) in a larger plexiglas flight chamber (FC). The chamber contains a pair of Helmholtz coils that generate a magnetic field. Each camera is fitted with a magnifying bellows (B) and a zoom lens (Z), and each view is back-lit by a bright red light-emitting diode source (S) that is focused using a simple convex lens (L). (B) An optical triggering system detects the presence of an insect in the filming volume and signals the cameras to record and the magnetic field to turn on. A red laser (L) emits a beam that is divided by a beam splitter (BS), re-routed by mirrors (M), passed through Galilean beam expanders (BE) and the chamber, and focused on photodiodes (PD). When an insect flies through the intersection of the beams, it is detected by the photodiodes, and a triggering circuit (not shown) initiates recording and the application of a magnetic field. (C) As an insect flies through the beams, the cameras capture the portion (red) of its trajectory that includes the application of the perturbing field.

Automated high-speed, three-dimensonal videography. See our earlier paper [25] and Fig. 5.7 for descriptions of the filming apparatus. Three synchronized, orthogonal high-speed cameras (Phantom v7.1, Vision Research, Inc., Wayne, NJ USA) record at 8000 frames per second (fps) when triggered by an optical detection system. This frame rate captures about 35 images during each wing-stroke, and the magnification is such that the insect body is typically about 80 pixels long. The experimental set-up described in ref. 1 is modified by changing the back-lighting and introducing the magnetic field system. Specifically, in place of slide projectors, we use bright red light-emitting diodes (LEDs, Diamond Dragon, OSRAM Opto Semiconductor, Sunnyvale, CA USA) to back-light each camera. The back-lighting and laser (HeNe, Thorlabs, Newton, NJ USA) are chosen to be red (wavelength > 600 nm) in order to minimize the visual stimulus to the insects, which have poor sensitivity to light of long wavelength [6]. The magnetic field system includes paired Helmholtz coils placed inside the flight chamber that pass a direct current from a power supply for 5 ms when triggered (Fig. 5.7). The number of windings in each coil, size and spacing of the coils, and magnitude of the current are chosen to generate a magnetic field strength of about 10^{-2} Tesla.

Automated motion tracking. The three-dimensional information contained in the flight videos is analyzed using a recently-developed method called Hull Reconstruction Motion Tracking [25]. HRMT uses the silhouette information captured in the movies to directly reconstruct a representation of the insect's three-dimensional shape. This reconstruction is analyzed in order to recover the position and orientation of the insect body and wings through time. The difference in the right and left wing angles of attack is used a measure of the wing-beat asymmetry and indicates active torque generation. The angle of at-

tack a is defined to be the orientation of the wing measured relative to its velocity. We take the convention that the angle is signed, assuming about 45 degrees for the down-stroke and about 135 degrees for the up-stroke. Here, the angle is averaged over each wing-stroke and is approximated by the pitch angle η measured relative to the horizontal. Hence, $\Delta\alpha \approx < \eta_R - \eta_L >$, where η is the wing pitch angle as measured directly by the HRMT method [25]. The approximation is exact in the limit of no stroke plane deviation and is justified by the small deviation for fruit fly wing motions [25, 12].

Control experiments. Movies that capture the flight of insects whose pins had fallen off show no change in behavior upon application of the field, indicating the field alone does not alter flight behavior. Further, experiments conducted with laboratory room lights off show no clear difference from those conducted with lights on. This supports the hypothesis that the mechanosensory halteres, and not visual system, are responsible for the observed recovery behavior.

Passive rotational damping of symmetrical flapping flight. As diagrammed in Fig. 5.4A,B of the text, unbalanced drag forces on the flapping wings cause rapid damping of the yaw motion [29, 18, 19]. Consider an insect of yaw moment of inertia I, average wing-beat angular speed ω, wing area S, and wing span length R. The body itself is rotating with yaw angular velocity $\dot{\psi}$. Because the Reynolds number Re = 100, we use an approximate high-Re fluid force law for the drag force on each wing,

$$D = \frac{1}{2}\rho S u^2 C_D(\alpha), \tag{5.6}$$

where ρ is the density of air, u is the wing speed relative to air, α is the angle of attack of the wing (orientation of wing relative to its velocity), and C_D is the

drag coefficient which depends on α. In a 2D approximation for rotary, flapping wings, we evaluate the drag force at two-thirds span length. Then, the average drag forces on the right and left wings act to give the yaw torque:

$$\frac{1}{2}\rho S C_{\mathrm{D}}(\alpha)\left(\frac{2}{3}R\right)^3 \cdot [-(\omega+\dot{\psi})^2 + (\omega-\dot{\psi})^2] = -2\left(\frac{2}{3}\right)^3 \rho S C_{\mathrm{D}}(\alpha) R^3 \omega\dot{\psi}. \tag{5.7}$$

Thus, the yaw dynamics are exponentially damped with a damping coefficient β that depends on wing properties:

$$I\ddot{\psi} = -\beta\dot{\psi}, \beta = 2\left(\frac{2}{3}\right)^3 \rho S C_{\mathrm{D}}(\alpha) R^3 \omega. \tag{5.8}$$

The damping occurs with a characteristic time of about 2 wing-beat periods:

$$\tau = \frac{I}{\beta} \approx 2T. \tag{5.9}$$

In the above calculation, we use approximate morphological and kinematic values obtained from measurements on fruit flies (*D. melanogaster*). For the body: $I = MR_{\mathrm{B}}^2$, with body mass $M = 10^{-6}$ kg and body radius $R_{\mathrm{B}} = 5 \cdot 10^{-4}$ m. For the wings: wing area $S = 2 \cdot 10^{-6}$ m^2 and span length $R = 2 \cdot 10^{-3}$ m. The drag coefficient (7) near $\alpha = 45°$ is $C_{\mathrm{D}} \approx 2$ and the average flapping angular speed is $\omega = 1100$ s^{-1}. This speed corresponds to a wing flapping with total amplitude sweep of about 140° and with wing-beat period of $T = 4.5$ ms. The fly flaps in air of density $\rho = 1.2$ kg·m^{-3}.

Active rotational motion by paddling. As diagrammed in Fig. 5.4C,D of the text, the insect actively turns by inducing differences between the right and left wing angles of attack. The insect initially has equal angles of attack $\alpha_{\mathrm{R}} = \alpha_{\mathrm{L}} = \alpha_0 \approx 45°$. Then, during drag ratcheting on the down-stroke (left images in Fig. 5.4C,D), the insect induces differences in the attack angles so that $\alpha_{\mathrm{R}} - \alpha_{\mathrm{L}} = \Delta\alpha > 0$. During the up-stroke, the angles then switch in order to maintain rightward

torque (right images in Fig. 5.4C,D). On average, the drag-based yaw torque sums to give:

$$\begin{aligned} I\ddot{\psi} &= \frac{1}{2}\rho S(\frac{2}{3}R)^3[-(\omega+\dot{\psi})^2\cdot C_{\mathrm{D}}(\alpha_{\mathrm{L}})+(\omega-\dot{\psi})^2\cdot C_{\mathrm{D}}(\alpha_{\mathrm{R}})] \\ &\approx \frac{1}{2}\rho S(\frac{2}{3}R)^3[-4\omega\dot{\psi}C_{\mathrm{D}}(\alpha_0)+\omega^2 C'_{\mathrm{D}}(\alpha_0)\cdot\Delta\alpha] \equiv -\beta\dot{\psi}+N_{\mathrm{fly}}. \end{aligned} \tag{5.10}$$

This calculation approximates the coefficient of drag dependence on angle of attack as $C_{\mathrm{D}}(\alpha) \approx C_{\mathrm{D}}(\alpha_0) + C'_{\mathrm{D}}(\alpha_0)\cdot(\alpha-\alpha_0)$ near $\alpha_0 = 45°$, which is justified by drag measurements in a dynamically-scaled experiment [9]. In addition, the terms that are second-order in are negligible because the wing speed is much greater than the body rotational speed: $(\dot{\psi}/\omega)2 < 0.01$, so the neglected terms are less than 1% of the retained terms. Thus, the yaw dynamics are again damped with the same damping constant as above and an additional, constant torque is generated by the paddling mechanism:

$$\begin{aligned} I\ddot{\psi} &= -\beta\dot{\psi}+N_{\mathrm{fly}}(\Delta\alpha), \\ \beta &= 2\left(\frac{2}{3}\right)^3\rho S\,C_{\mathrm{D}}(\alpha)R^3\omega, \\ N_{\mathrm{fly}} &= \frac{1}{2}\left(\frac{2}{3}\right)^3\rho S\,C'_{\mathrm{D}}(\alpha_0)R^3\omega^2\cdot\Delta\alpha. \end{aligned} \tag{5.11}$$

The torque N_{fly} is thus directly proportional to the angle of attack asymmetry $\Delta\alpha$.

Perfect correction for integral response. The complete yaw dynamics includes inertia, passive rotational damping, drag ratcheting torque generation, and the disturbing torque:

$$I\ddot{\psi} = -\beta\dot{\psi}+N_{\mathrm{fly}}(\dot{\psi})+N_{\mathrm{ext}}. \tag{5.12}$$

Here, we assume that the insect responds by outputting a torque that depends on its sensory measurement of body angular velocity. If the response is a linear

operator on angular velocity, then we can analyze the system using the Laplace transform [3]. Taking advantage of the fact that the Laplace transform of the derivative of a function is the frequency times that function, we obtain:

$$Is\dot{\psi}(s) = -\beta\dot{\psi}(s) + N_{\text{fly}}(s)\dot{\psi}(s) + N_{\text{ext}}(s). \tag{5.13}$$

where all functions are now in frequency space and s is the Laplace frequency variable. Assuming a stable system, the Laplace transform of angular velocity is then:

$$\dot{\psi}(s) = \frac{N_{\text{ext}}(s)}{Is + \beta - N_{\text{fly}}(s)}. \tag{5.14}$$

The requirement for accurate correction is that the total change in yaw angle over all time is zero:

$$\Delta\psi = 0 = \int_0^\infty \mathrm{d}t\dot{\psi} = \lim_{s\to 0}\int_0^\infty \mathrm{d}t\mathrm{e}^{-st}\dot{\psi} = \lim_{s\to 0}\dot{\psi}(s). \tag{5.15}$$

Hence, the low-frequency limit of the Laplace transform of angular velocity must be zero. Now, $N_{\text{ext}}(s)$ can be expressed as a series containing terms proportional to s^n with $n \geq 0$ for disturbances that last a finite period of time. With regard to recovery, the "worst-case scenario" is that of an impulse: N_{ext} is a constant ($n = 0$). [A disturbance of $N_{\text{ext}}(s) \sim s^n$, for any $n \geq 1$, would move the insect and then return it and would thus require no response from the insect.] The simplest controller that guarantees correction after an impulsive disturbance must then have $N_{\text{fly}}(s) \sim 1/s$ in order satisfy Eqs. 5.14 and 5.15. Performing the inverse transform, this operation is the integration over time of the angular velocity [3]. Thus, the minimal controller integrates velocity. Note that this argument is unaffected by the presence of delay, which does not alter the long-time (low-frequency) behavior of the system.

BIBLIOGRAPHY

[1] M. J. Abzug and E. E. Larrabee. *Airplane Stability and Control: A History of the Technologies That Made Aviation Possible*. Cambridge University Press, Cambridge UK, 2002.

[2] V. Apostolyuk. Theory and design of micromechanical vibratory gyroscopes. In *MEMS/NEMS Handbook: Techniques and Applications*, pages 173–195, New York, 2006. Springer.

[3] J. Bechhoefer. Feedback for physicists: A tutorial essay on control. *Rev. Mod. Phys.*, 77:783–836, 2005.

[4] J. A. Bender and M. H. Dickinson. Visual stimulation of saccades in magnetically tethered drosophila. *J. Exp. Biol.*, 209:3170–3182, 2006.

[5] A. J. Bergou, L. Ristroph, J. Guckenheimer, Z. J. Wang, and I. Cohen. Fruit flies modulate passive wing pitching to generate in-flight turns. *Phys. Rev. Lett.*, 104:148101, 2010.

[6] A. D. Briscoe and L. Chittka. The evolution of color vision in insects. *Ann. Rev. Entomol.*, 46:471–510, 2001.

[7] M. H. Dickinson. Haltere-mediated equilibrium reflexes of the fruit fly, drosophila melanogaster. *Phil. Trans. R. Soc. Lond. B*, 354:903–916, 1999.

[8] M. H. Dickinson. The initiation and control of rapid flight maneuvers in fruit flies. *Integr. Comp. Biol.*, 45:274–281, 2005.

[9] M. H. Dickinson, F.-O. Lehmann, and S. Sane. Wing rotation and the aerodynamic basis of insect flight. *Science*, 284:1954–1960, 1999.

[10] R. Dudley. *The Biomechanics of Insect Flight: Form, Function, Evolution*. Princeton University Press, Princeton, 2000.

[11] J. L. Fox and T. L. Daniel. A neural basis for gyroscopic encoding in the halteres of holorusia. *J. Comp. Physiol. A*, 194:887–897, 2008.

[12] S. N. Fry, R. Sayaman, and M. H. Dickinson. The aerodynamics of free-flight maneuvers of drosophila. *Science*, 300:495–498, 2003.

[13] S. N. Fry, R. Sayaman, and M. H. Dickinson. The aerodynamics of hovering flight of drosophila. *J. Exp. Biol.*, 208:2303–2318, 2005.

[14] D. Grimaldi and M. S. Engel. *Evolution of the insects*. Cambridge University Press, Cambridge UK, 2005.

[15] G. Heide. Neural mechanisms of flight control in diptera. In *BIONA report 2*, pages 35–52, Stuttgart, 1983. Fischer.

[16] G. Heide and K. G. Goetz. Optomotor control of course and altitude in drosophila is correlated with distinct activities of at least three pairs of steering muscles. *J. Exp. Biol.*, 199:1711–1726, 1996.

[17] M. Heisenberg and R. Wolf. The sensory-motor link in motion-dependent flight control of flies. In *Visual Motion and its Role in the Stabilization of Gaze*, pages 265–283, Amsterdam, 1993. Elsevier.

[18] T. Hesselberg and F.-O. Lehmann. Turning behavior depends on frictional damping in the fruit fly drosophila. *J. Exp. Biol.*, 210:4319–4334, 2007.

[19] T. Hesselberg and F.-O. Lehmann. Wingbeat time and the scaling of passive rotational damping in flapping flight. *Science*, 324:252–255, 2009.

[20] D. L. Jindrich and R. J. Full. Dynamic stabilization of rapid hexapedal locomotion. *J. Exp. Biol.*, 205:2803–2823, 2002.

[21] M. Mayer, K. Vogtmann, B. Bausenwein, R. Wolf, and M. Heisenberg. Flight control during 'free yaw turns' in drosophila melanogaster. *J. Comp. Physiol. A*, 163:389–399, 1950.

[22] N. Minorsky. Directional stability of automatically steered bodies. *J. Am. Soc. Nav. Eng.*, 34:280–309, 1922.

[23] H. Mittelstaedt. hysiology of the sense of balance of flying dragonflies. *J. Comp. Physiol. A*, 32:422463, 1950.

[24] J. W. S. Pringle. The gyroscopic mechanism of the halteres of diptera. *Phil. Trans. R. Soc. Lond. B*, 233:347–384, 1948.

[25] L. Ristroph, G. J. Berman, A. J. Bergou, Z. J. Wang, and I. Cohen. Automated hull reconstruction motion tracking (hrmt) applied to sideways maneuvers of free-flying insects. *J. Exp. Biol.*, 212:1324–1335, 2009.

[26] D. A. Robinson. Integrating with neurons. *Ann. Rev. Neurosci.*, 12:33–45, 2008.

[27] D. C. Sandeman and H. Markl. Head movements in flies (calliphora) produced by deflexion of the halteres. *J. Exp. Biol.*, 85:43–60, 1980.

[28] S. P. Sane, A. Dieudonne, M. A. Willis, and T. L. Daniel. Antennal mechanosensors mediate flight control in moths. *Science*, 315:863–866, 2007.

[29] R. F. Stengel. *Flight dynamics*. Princeton University Press, Princeton, 2004.

[30] M. Sun and Y. Xiong. Dynamic flight stability of a hovering bumblebee. *J. Exp. Biol.*, 208:447459, 2005.

[31] L. F. Tammero and M. H. Dickinson. he influence of visual landscape on the free flight behavior of the fruit fly drosophila melanogaster. *J. Exp. Biol.*, 205:327–343, 2002.

[32] G. K. Taylor and H. G. Krapp. Sensory systems and flight stability: What do insects measure and why? *Adv. Insect. Physiol.*, 34:231–316, 2007.

[33] G. K. Taylor and A. L. R. Thomas. Dynamic flight stability in the desert locust schistocerca gregaria. *J. Exp. Biol.*, 206:28032829, 2003.

[34] R. J. Wood. First take-off of a biologically-inspired at-scale robotic insect. *IEEE Trans. on Robotics*, 24:341–347, 2008.

[35] O. Wright and W. Wright. United states patent no. 821393, 1906.

CHAPTER 6

SMALL, SLEEK, AND IN CONTROL: THE BODY PLAN AND FAST FLIGHT STABILIZATION OF INSECTS

6.1 Summary

Flying insects have evolved sophisticated sensory-neural systems, and here we argue that their fast reaction times reflect the need to overcome an intrinsic flight instability [1]. We formulate a theory that shows how the body morphology and flapping-wing aerodynamics determine the instability growth rate, which in turn dictates the response time needed to suppress it. We experimentally validate this model by manipulating the flight, sensors, and body plan of fruit flies. Finally, a generalization of this theory provides stability criteria for a broad class of hovering insects, hummingbirds, and flapping-wing robots.

6.2 Stability or control?

Flight of both animals and machines requires not only generating aerodynamic force sufficient to counter gravity but also maintaining balance while aloft [14, 1, 40]. For fixed-wing aircraft, the need for balance has led to solutions ranging from passenger airliners that are stable by design to fighter jets that require active control of wing surfaces to overcome intrinsic instabilities [50]. More generally, the intrinsic dynamics of an aircraft imposes demands on its control strategies, with faster-growing instabilities demanding faster active responses [39, 5]. For the flapping-wing flight of animals, this interplay of control

[1] This work will soon be submitted for publication.

and stability remains largely unexplored. While recent aerodynamic simulations indicate that body pitch orientation is intrinsically unstable for some specific insects [41, 42, 19], it is unclear whether this is a generic feature of insect flight. Further, the impact of instabilities on the sensory-neural systems that must suppress their growth has not been investigated, and there is little experimental work to corroborate theoretical studies [44].

6.3 Fast flight stabilization in fruit flies

We investigate insect flight stability and control by mechanically perturbing the flight of fruit flies, *D. melanogaster*. In these experiments, we glue small magnets to the backs of flies and apply a magnetic field that perturbs the body pitch orientation while capturing the wing and body motions with high-speed video cameras [34, 33]. The observed flight trajectory for a representative experiment is shown in Fig. 6.1(a). The insect is rotated nose-down by the perturbation but quickly recovers its orientation and thus keeps upright. The insect drives this recovery by adjusting its wing motions, most notably by increasing the forward sweep of its wings [Fig. 6.1(b)]. These measurements are consistent with a strategy in which shifting the aerodynamic center of lift towards the front of the insect generates a nose-up pitch torque that counters the nose-down perturbation [55, 43].

To quantify the recovery dynamics, we use a motion-tracking method that extracts the body and wing positions and orientations through time [34]. The measured pitch dynamics for the sequence shown in Fig. 6.1(a) are shown in (c) and the stroke center angle of the wings in (d). Data from twelve such

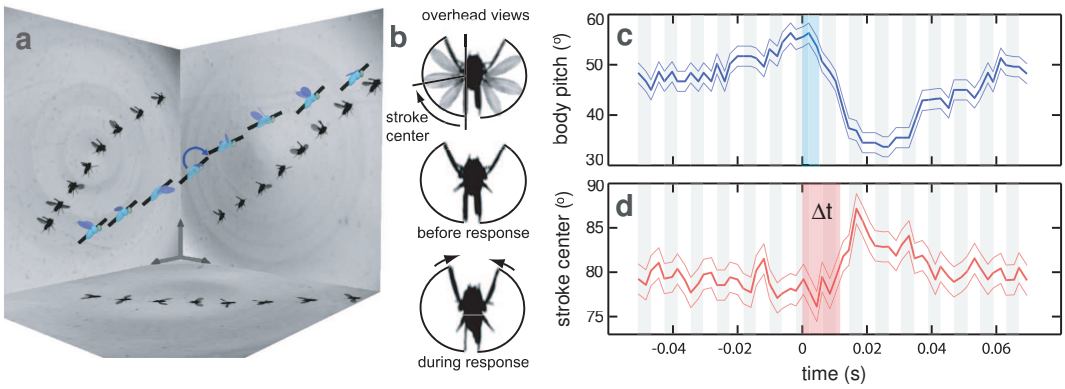

Figure 6.1: Fruit flies quickly overcome in-flight perturbations. (a) Reconstruction of a flight perturbation filmed with three high-speed cameras. Selected images from each camera are shown on the side panels, and the measured configurations of the insect (body length 2.5 mm) are displayed on the model. A black bar on the insect body highlights its pitch orientation. As the insect ascends from left to right, a magnetic field (blue arrow) induces a torque on the ferromagnetic pin glued to its back. (b) The insect responds by sweeping its wings further in front thus generating a nose-up corrective torque. (c) Body pitch orientation. The magnetic torque perturbation (blue stripe) tips the insect downward, and the insect responds by correcting its orientation. (d) The average wing stroke center angle. After a reaction time of $\Delta t = 12$ ms (red stripe), the fly initiates corrective wing motions.

experiments reveal that these insects make corrective actions after a reaction time $\Delta t = (13 \pm 2)$ ms, or about 3 wing-beats. Remarkably, this reaction time approaches the fastest behavioral responses in the animal kingdom [8, 38, 36] and is only an order-of-magnitude longer than the time-scales typical of neural synapses [26].

6.4 Theoretical stability analysis

Understanding the need for a fast response requires knowledge of the time-scales associated with pitch dynamics during flight. The relevant physical mechanisms can be illustrated most simply for hovering. The wings beat back-

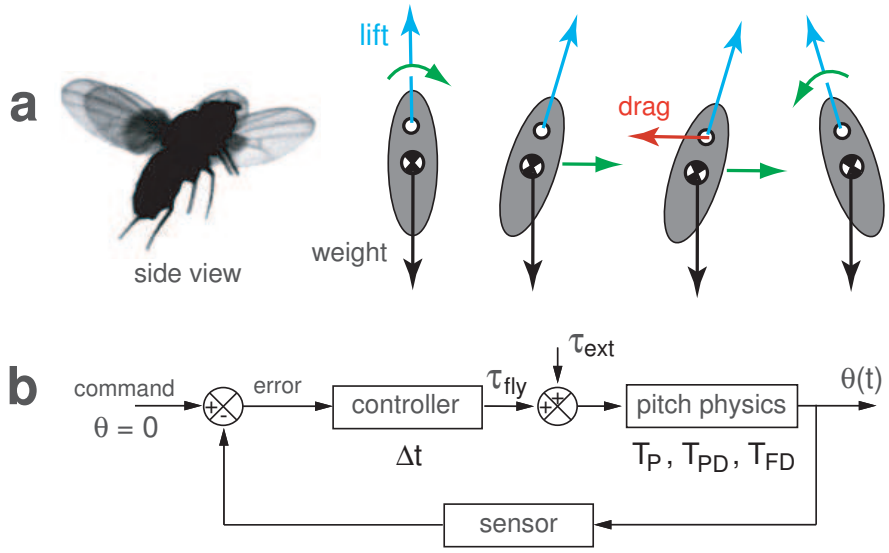

Figure 6.2: Fruit fly flight is intrinsically unstable and requires a fast control response. (a) During hovering, wings flap back-and-forth to produce lift that balances body weight. A perturbation to the pitch orientation causes the the insect to move forward, drag on the wings then becomes unbalanced and tips the insect over. (b) Because flight is intrinsically unstable, feedback control is needed. The reaction time Δt of the control response must be fast compared to the instability growth rate. The growth rate itself depends on physical time-scales (T_{P}, T_{PD}, T_{FD}) relevant to the pitch dynamics.

and-forth, the average lift is directed upward to balance body weight, and drag points horizontally but cancels for the two half-strokes [Fig. 6.2(a)]. If pitched forward, the re-directed lift drives the insect forward. This leads to a net drag on the wings, because the wing airspeed on the forward sweep is now greater than the airspeed on the backward sweep. If the wings are located above the body center of mass, as is the case for flies and many other insects [16], this drag creates a pitch torque that rotates the insect backward. In effect, the insect is flipped over or, "clothes-lined", by drag on its wings. If left uncontrolled, this clothesline instability rocks the insect back-and-forth with growing amplitude and ultimately causes it to tumble from the air.

These ingredients – weight, lift, drag, and drag-based torque – can be com-

bined to form a reduced-order dynamical model of the insect's forward velocity u, pitch angle θ, and pitch rate $\omega = \dot{\theta}$.

$$\dot{u} = -\frac{1}{T_{\mathrm{FD}}} \cdot u + g \cdot \theta \tag{6.1}$$

$$\dot{\omega} = -\frac{1}{T_{\mathrm{PD}}} \cdot \omega - \frac{1}{g T_{\mathrm{FD}} T_{\mathrm{P}}^2} \cdot u \tag{6.2}$$

Physically, the first term in Eq. 6.1 indicates that wing drag slows translational motion with a characteristic forward damping time T_{FD} that depends on the wing aerodynamic characteristics. The second term accounts for the forward acceleration produced by re-directed lift in the small pitch angle limit. Similarly, the first term in Eq. 6.2 indicates that fluid resistance slows rotations with a characteristic pitch damping time of T_{PD} that depends on body drag. The second term describes the drag-based torque that arises from the displacement of the wing attachment point from the body center-of-mass as well as the resulting pendulum-like dynamics. Combining these equations, we arrive at a single differential equation for pitch in the absence of external torques:

$$T_{\mathrm{FD}} \dddot{\theta} + (1 + T_{\mathrm{FD}}/T_{\mathrm{PD}}) \ddot{\theta} + (1/T_{\mathrm{PD}}) \dot{\theta} + (1/T_{\mathrm{P}}^2) \theta = 0. \tag{6.3}$$

Written in this form, the third physical time-scale $T_{\mathrm{P}} = \sqrt{L/g}$ can now be seen to correspond to a pendulum oscillation time. The pendulum length $L = I/Mh$ results from that fact that the insect body (moment of inertia I and mass M) is similar to a compound pendulum with its wings a distance h above the center-of-mass [16].

The dynamics described by Eq. 6.3 indicate that an uncontrolled insect is analogous to a damped rotational oscillator with a destabilizing driving term represented by the third-order derivative. Using measurements of the body morphology and wing aerodynamic characteristics for fruit flies, we determine

T_P, T_{PD}, and T_{FD} and find that perturbations to Eq. 6.3 grow exponentially with a time-scale of 60 ms, or about 14 wing-beats.

6.5 Active stabilization

To manage this instability, fruit flies employ a feedback control scheme that senses body rotations using organs called halteres [30] and thus determines the appropriate sweep angles for the wings [Fig. 6.2(b)]. As anyone who has tried balancing an upright stick knows, the challenge in controlling such an unstable system is reacting at a time-scale Δt that is fast relative to the instability growth time [39, 5]. Feedback control theory provides a quantitative criterion for assessing the performance of such a time-delayed response in controlling an unstable process [5, 4, 21]. Applying this theory to the fly, we find that the measured reaction time confers robust stability, suggesting that the nervous system and body plan co-evolved to produce good flight performance [35].

This control model also predicts that stabilization performance depends sensitively on the reaction time Δt as well as on the physical time-scales. To test this prediction, we employ classic techniques that manipulate both the sensors and body plan of insects [20]. First, we disable the sensory function of the halteres by gluing them down [Fig. 6.3(a) and (b)] and find that the fly loses stability, as shown by the tumbling flight trajectory shown in the left inset of Fig. 6.3(d). To quantify this loss of flight capability, we release flies in air and measure their flight angle, which is always less than 10° for sensor-disabled insects. In a second experiment, we find that stability can be reinstated if body drag is increased. We glue dandelion seed fibers to haltere-disabled insects [Fig. 6.3(c)]

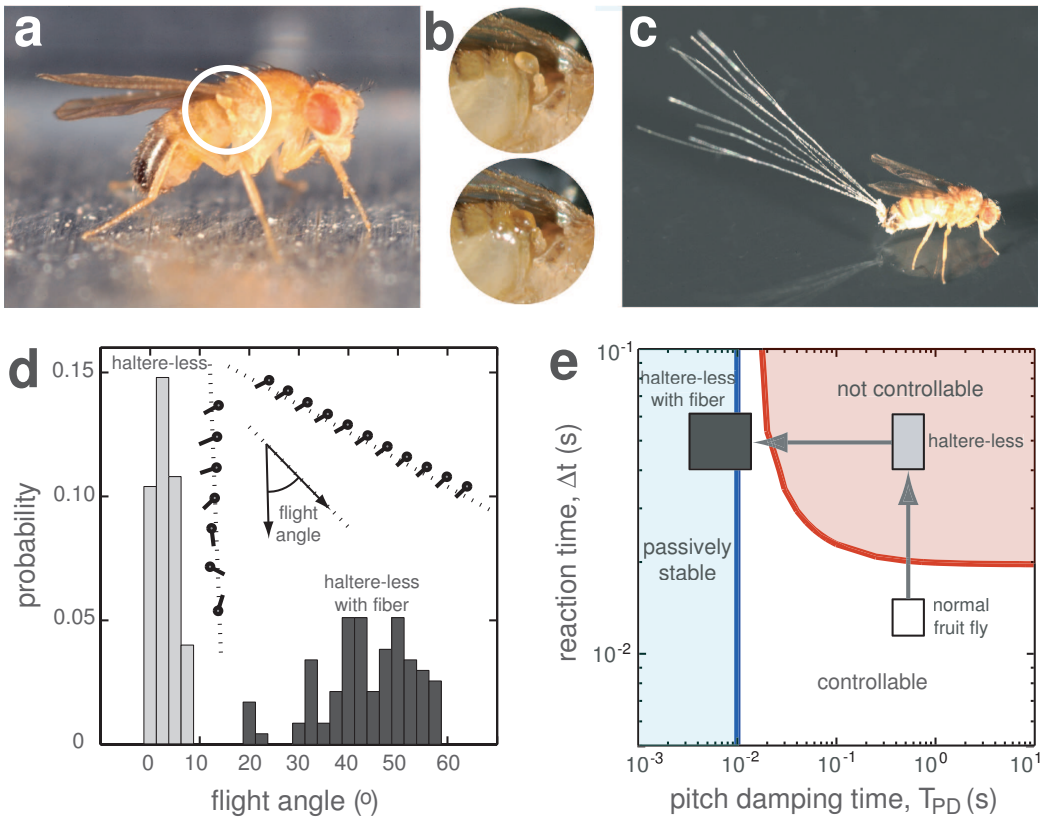

Figure 6.3: Testing the flight control model by manipulating sensors and body plan. (a) Fruit flies use fast gyroscopic sensors called halteres to mediate flight control. (b) Each haltere vibrates during flight and is sensitive to changes in body orientation. If glued down, the haltere no longer properly functions. (c) Dandelion seed fibers add drag to the insect body, thus increasing passive stability. (d) Disabling the halteres destroys flight stability while adding fibers restores stability. Inset: Flight trajectories of a fly with halteres disabled (left) and then with fibers added on (right). Main figure: Probability distributions of flight angle for haltere-disabled and fibered insects. (e) Theoretical interpretation: Normal fruit flies (white square) can control flight because of their fast sensory response time. The haltere-disabled insects (gray) cannot control flight with slower sensors, such as eyes. If fibers are added (black), flight can be controlled with slower sensors or passively stabilized.

and observe a recovery in flight capability: a typical trajectory is shown in the right inset of Fig. 6.3(d), and these insects now fly with a mean angle of 45°.

In Fig. 6.3(e), we use the control model to interpret these observations as transitions in stability. The plot characterizes stability as a function of reaction time Δt and pitch damping time T_{PD}. Plotted are regions in which flight is passively stable due to high body drag (small T_{PD}, blue region) and intrinsically unstable but actively controllable given a sufficiently fast response. An unmodified fly (white square) has little damping and thus lacks passive stability but instead relies on a fast control response. When the fast sensors are disabled (gray square), the fly must rely on slower modalities, such as vision which has $\Delta t \sim 50$ ms [25]. Our model predicts that slower sensors encounter severe difficulty in controlling flight, and indeed these insects tumble from the air. If high-drag fibers are added to the body (black square), body drag increases, pitch damping time drops dramatically, and flight can be stabilized either passively or with slower sensors.

6.6 Generalization to other insects and robots

The success of this model for the fruit fly suggests that it can be used as a general framework for understanding the control of flapping-wing flight. According to our model, the various body plans of hovering insects, birds, and robots will determine the necessary response time needed to stabilize flight [Fig. 6.4(a)-(c)]. In Fig. 6.4(d), we show how this response time Δt (colored contours) changes as a function of the pitch damping time T_{PD} (horizontal axis) and the pendulum time T_{P} (vertical axis), which are the two time-scales that dominate the pitch

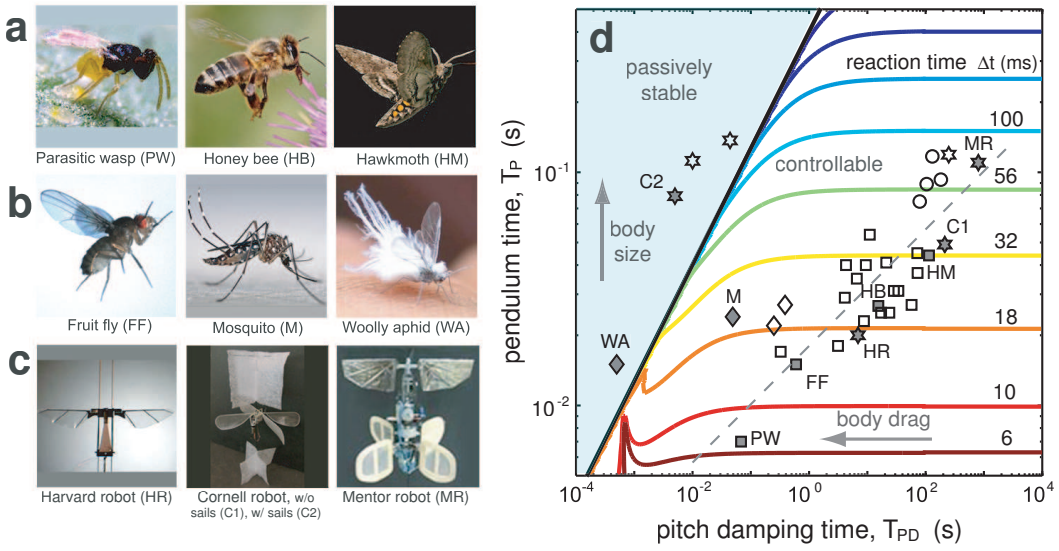

Figure 6.4: Control requirements for insects and flapping-wing robots. (a) Many insects share a similar body plan but vary in size: the wasp is 0.6 mm in body length, honey bee 16 mm, and hawkmoth 46 mm. (b) Insects of similar size (few mm in body length) have varying degrees of body drag: mosquitoes fly with legs extended, and the woolly aphid has a fibrous covering. (c) Flapping-wing robots with different stability strategies: Harvard robot (15 mm) is externally stabilized with wire guides; Cornell robot (220 mm) has large sails; Mentor robot (360 mm) has gyroscope-based feedback control. (d) Predicted reaction time needed to stabilize flight. Contours are the reaction time needed, and the two physical time-scales T_P and T_{PD} can be estimated from body morphological data. Represented are insects with compact body plans (squares), high-drag insects (diamonds), hummingbirds (circles), and robots (stars).

dynamics. Short T_{PD} and long T_P correspond to high body drag and large body size, respectively, and lead to linear stability of Eq. 6.3 and thus passive stability of flight (blue region). By compiling morphological and flight data for many flyers, we estimate these physical time-scales and thus predict the required reaction time. Our theory predicts, for example, that honeybees must respond faster than 23 ms, and recent behavioral measurements confirm that bees react to gusts of wind with a speed of (25 ± 5) ms [49]. Further, we predict that hawkmoths need a 32 ms reaction time, and simulations have indicated that stabilization is difficult with controllers slower than one wing-beat (38 ms) [24].

Our comparative analysis reveals that, with respect to stability, a wide variety of insects have scaled versions of a similar body plan that is compact and devoid of damping surfaces [Fig. 6.4(a)]. Isometric scaling of these insects indicates that $T_P \sim T_{PD}^{1/4}$, which captures observed trend shown as the dashed line in Fig. 6.4(d). Further, our model predicts that for these insects, the required reaction time depends primarily on the pendulum time-scale: $\Delta t \sim T_P = \sqrt{L/g}$, where $L = I/Mh$ is the pendulum length of the insect. Thus, bigger animals require slower sensors, while the smallest insects, such as the parasitic wasp *Encarsia formosa*, are predicted to require the fastest reaction times.

This analysis also provides design criteria for flapping-wing robots, such as those shown in Fig. 6.4(c), and these flyers have been included as stars in (d). The Cornell micro-air vehicle provides an interesting test case for the theory [31]. Without the sail-like surfaces (C1), this robot is unstable, consistent with our model predictions. Fitting it with sails (C2) instills passive stability, and our model accounts for this stabilization by damping and also indicates that an alternate strategy would involve the use of a 30 Hz active controller.

As a final comparative study, we identified similarly-sized insects that have different degrees of damping, as shown in Fig. 6.4(b). The fruit fly, mosquito, and woolly aphid are all millimeter-sized. Relative to the fly, the mosquito has long legs that are extended in flight, providing inertial and damping stabilization and permitting slower response times. The woolly aphid's fibrous covering represents a bizarre extreme in damping, and our model indicate that the aphid may be one of the few intrinsically stable flying insects.

6.7 Stability, control, and the evolution of flight

This strategy of passive stabilization may have been employed by the first flying insects. In particular, the first flyers are unlikely to have had the fast and sophisticated sensory-neural systems of modern insects and may instead have relied on body plans that confer intrinsic stability [35]. Though the palaeontological record is too incomplete to fully support this conjecture, fossil insects do include damping features such as plate-like lobes, abdominal fibers, and long, hair-like cerci [27]. In most modern insects, damping structures are conspicuously absent, which may reflect an adaptation toward maneuverability and evasiveness in Nature's increasingly crowded airspace.

6.8 Supporting Information

Dynamical model of body pitch. Recent aerodynamic simulations indicate that body orientation is intrinsically unstable for some insects [41, 42, 19]. These simulations include both computational fluid dynamics (CFD) codes that numerically solve the Navier-Stokes equations as well as quasi-steady models that approximate aerodynamic forces on the flapping wings. Both couple fluid forces to the rigid-body dynamics of the insect body. These simulations show that body pitch is subject to diverging oscillations, and this instability appears for simulations of flies, bees, and moths. Its presence in a variety of computational implementations using a variety of insect body forms suggests that pitch instability is a generic feature of flapping-wing flight.

The CFD work of Sun's group inspires a simplified physical picture of the in-

stability [41]. The relevant physical mechanisms can be illustrated most simply for hovering flight. The wings beat back-and-forth, the average lift is directed upward to balance body weight, and drag points horizontally but cancels for the two half-strokes. If pitched forward, the re-directed lift drives the insect forward. This leads to a net drag on the wings, because the wing airspeed on the forward sweep is now greater than the airspeed on the backward sweep. If the wings are located above the body center of mass, as is the case for flies and many other insects [16], this drag creates a nose-up pitch torque that rotates the insect. In effect, the insect is flipped backwards by the drag on its wings. If left uncontrolled, this instability rocks the insect back-and-forth with growing amplitude and ultimately causes it to tumble from the air.

These observations suggest a minimal set of ingredients to be included in a reduced-order model. The insect body is an extended rigid body of mass M and pitch moment of inertia I. We will evaluate longitudinal motion of this body, that is, the dynamics of the forward speed, upward speed, pitch angle and pitch rate, $(u, v, \theta, \omega = \dot{\theta})$. The body orientation during hovering defines $\theta = 0$. So-called "normal hovering" insects beat their wings back-and-forth [51], and average lift points upward and balances body weight: $L = Mg$. We assume the wings co-move with the body, so the average lift vector is of fixed position and orientation with respect to the body [16, 17]. As we will show, the distribution of drag is critical to the flight dynamics. For the sake of generality, we assume the insect body has distributed sources of linear drag $\vec{D}$ at displacements $\vec{r}$ from the center-of-mass. Such drag sources include the wings, which have been shown to give rise to drag linear in body velocity [32], as well as viscous forces on the body itself and on other damping surfaces such as legs. Drag is directed opposite to the velocity $\vec{v}$ for each drag source, $\mathrm{d}\vec{D} = -\vec{v} \cdot \mathrm{d}\mu$. Here, $\mathrm{d}\mu$ represents

the dependence of drag on aerodynamic characteristics of the source (such as size and coefficient of drag) as well as on fluid properties (such as density and viscosity).

We next write down a general linear model of the longitudinal dynamics. If the insect is pitched, horizontal body acceleration $\dot{u} = L/M \sin\theta \approx g\theta$ results from the re-directed lift. Vertical body acceleration $\dot{v}$ stems from the loss of lift, but this is a second-order effect. Thus, vertical dynamics are unchanged in the linearized system leading us to evaluate the simplified (u, θ, ω) system. Drag causes both translational or angular velocities to couple to both translational and angular accelerations. Thus, the general system can be described using the linearized Newton-Euler equations:

$$\dot{u} = \alpha \cdot \theta - \beta \cdot u - \delta \cdot \omega \tag{6.4}$$

$$\dot{\theta} = \omega \tag{6.5}$$

$$\dot{\omega} = -\epsilon \cdot \omega - \gamma \cdot u + \tau \tag{6.6}$$

Here, $\alpha = g$ is the re-directed lift-based acceleration, the coefficients $(\beta, \gamma, \delta, \epsilon)$ define how the sources of drag give rise to accelerations, and τ is the net external pitch torque divided by the body moment of inertia. Evaluation of the drag sources distributed at displacements $\vec{r}$ from the body center-of-mass leads to the following relations: $\beta = \frac{\int \mathrm{d}\mu}{M}$, $\epsilon = \frac{\int r^2 \mathrm{d}\mu}{I}$, $\gamma = \frac{\int \vec{r}\cdot\hat{y}\mathrm{d}\mu}{I}$, and $\delta = \frac{\int \vec{r}\cdot\hat{y}\mathrm{d}\mu}{M}$ with $\hat{y}$ the vertical unit vector. Thus, coefficients in this dynamical system appear as ratios of moments of the drag distribution and moments of the mass distribution ($M = \int \mathrm{d}m$ and $I = \int r^2 \mathrm{d}m$).

Taking the Laplace transform of the above system reveals some simplifications. The transfer function from external torque to pitch angle can be shown to

be

$$\frac{\tilde{\theta}}{\tilde{\tau}} = \frac{\frac{1}{\beta}s + 1}{\frac{1}{\beta}s^3 + (1 + \frac{\epsilon}{\beta})s^2 + (\epsilon - \frac{\delta\gamma}{\beta})s + \frac{\alpha\gamma}{\beta}}, \tag{6.7}$$

where $\tilde{\cdot}$ represents the Laplace transform and s is the frequency variable. This form reveals that some variables appear only as combinations, and this inspires a physical interpretation of these combinations. The quantities β and ϵ appear alone, and their inverses are simply characteristic time-scales for which forward and pitch motions are damped by drag. To evaluate the other variables, it is convenient to define a center-of-drag vertical displacement from the center-of-mass, $h = \frac{\int \vec{r}\cdot\hat{y}\mathrm{d}\mu}{\int \mathrm{d}\mu}$. Then, one can show that $\frac{\alpha\gamma}{\beta} = \frac{Mgh}{I}$, which is similar to squared oscillation frequency for a compound pendulum supported at a distance h from the center-of-mass (positive upwards). Further, it can be shown that the term $\frac{\delta\gamma}{\beta} = \frac{Mh^2}{I}\beta$. Considering only nearly symmetric drag distributions allows one to linearize in h and thus drop this term.

These findings suggest interpretations of all quantities in terms of physical time-scales. Forward motion is damped with a characteristic time of $T_{\mathrm{FD}} = 1/\beta$, and pitch rotations are also damped over a time-scale of $T_{\mathrm{PD}} = 1/\epsilon$. The insect body will have an inherent pendulum-like oscillation time of $T_{\mathrm{P}} = \sqrt{\beta/\alpha\gamma} = \sqrt{I/Mg|h|}$. The Laplace transform of the simplified system now becomes

$$\frac{\tilde{\theta}}{\tilde{\tau}} = \frac{T_{\mathrm{FD}}s + 1}{T_{\mathrm{FD}}s^3 + (1 + \frac{T_{\mathrm{FD}}}{T_{\mathrm{PD}}})s^2 + \frac{1}{T_{\mathrm{PD}}}s \pm \frac{1}{T_{\mathrm{P}}^2}}. \tag{6.8}$$

The distinction of ± correspond to the cases $h > 0$ (high center-of-drag)and $h < 0$ (low center-of-drag), respectively. The corresponding system of differential equations is given by:

$$\dot{u} = g \cdot \theta - \frac{1}{T_{\mathrm{FD}}} \cdot u \tag{6.9}$$

$$\dot{\theta} = \omega \tag{6.10}$$

$$\dot{\omega} = -\frac{1}{T_{\mathrm{PD}}} \cdot \omega \mp \frac{1}{g T_{\mathrm{FD}} T_{\mathrm{P}}^2} \cdot u + \tau \tag{6.11}$$

Algebraic elimination of u and ω for θ, yields a single differential equation that applies in the absence of external torques $\tau = 0$:

$$T_{\mathrm{FD}} \dddot{\theta} + (1 + T_{\mathrm{FD}}/T_{\mathrm{PD}})\ddot{\theta} + (1/T_{\mathrm{PD}})\dot{\theta} \pm (1/T_{\mathrm{P}}^2)\theta = 0. \tag{6.12}$$

This equation is similar to a damped rotational oscillator but the presence of forward damping leads to two modifications. First, the effective moment of inertia is enhanced by the ratio $T_{\mathrm{FD}}/T_{\mathrm{PD}}$. Second and more importantly, the presence of the third-derivative term acts as a driving source that injects energy into the oscillator and can destabilize it.

Assessing intrinsic stability of body pitch. The inherent stability of body pitch during flight can be formally evaluated by assessing the mathematical stability of Eq. 6.12. This procedure considers solutions of the form $\theta \sim \mathrm{e}^{(\lambda t)}$, where λ is a complex eigenvalue of the system. This leads to the characteristic equation:

$$T_{\mathrm{FD}}\lambda^3 + (1 + T_{\mathrm{FD}}/T_{\mathrm{PD}})\lambda^2 + (1/T_{\mathrm{PD}})\lambda \pm (1/T_{\mathrm{P}}^2) = 0. \tag{6.13}$$

The equation has three roots which correspond to three eigenvalues. If the real part of any root greater than zero, then deviations grow exponentially and the system is unstable. Although analytical solutions for the roots of Eq. 6.13 can be obtained, their mathematical forms offer little insight since they are generally complicated functions of the time-scales (T_{P}, T_{PD}, T_{FD}). For values of these time-scales for most insects, there exist a pair of complex conjugate eigenvalues with positive real parts. In control theory terms, the system is said to have a pair of right-half-plane (rhp) poles. Physically, this indicates that body pitch during flight exhibits an oscillating, diverging instability.

The Routh criterion provides a general relationship among the physical time-scales necessary to furnish inherent stability. If the center-of-drag is low, then we are dealing with the negative form of Eq. 6.13 and this criterion indicates that flight is unstable for all values of the physical time-scales. If the center-of-drag is high, then we are dealing with the positive form of Eq. 6.13 and the Routh criterion for stability is:

$$\left(\frac{1}{T_{\mathrm{FD}}}+\frac{1}{T_{\mathrm{PD}}}\right)\frac{1}{T_{\mathrm{PD}}}>\frac{1}{T_{\mathrm{P}}^{2}}. \tag{6.14}$$

This result confirms some physical intuition: generally, more damping (smaller T_{PD} or smaller T_{FD}) and larger body sizes (larger T_{P}) tend to offer more stability. As shown the paper, however, the physical time-scales for most insects are such that flight is intrinsically unstable.

Reaction time needed to suppress the instability. Unstable processes are inherently difficult to control, especially in cases in which this control response is delayed in time [39]. Control theory provides a quantitative assessment of control performance in such a scenario [21, 4, 5]. The key idea is that performance suffers when there is a phase shift, or phase loss, for a disturbance signal that propagates through a controller and physical process. Intuitively, this can be seen by considering how sinusoidal disturbances are affected by different phase losses under the action of negative feedback. A phase loss of 0, for example, results in exact cancelation of a disturbance signal. A phase loss of π, on the other hand, reinforces the disturbance and leads to instability of the combined controller-process system. Thus, controllers and physical processes that induce phase loss are generally undesirable. The phase loss due to both instabilities (poles in the physics) and time delays can be rigorously evaluated and then compared to standards for acceptable control performance.

The qualitative reasoning given above has been formalized into the so-called *design inequality* [5]:

$$-\arg L_{nmp}(i\omega_{gc}) \leq \pi - \phi_m + n_{gc}\frac{\pi}{2} \equiv \phi_l, \tag{6.15}$$

with good rules-of-thumb requiring that the constants $\phi_m \approx \pi/4$ and $n_{gc} \approx -0.5$ and thus $\phi_l \approx \pi/2$. Here, $L = PC$ is the open-loop transfer function for a physical process P and controller C, and L_{nmp} is its so-called non-minimum phase portion, which includes the effects of poles and delays. The gain-crossover frequency ω_{gc} is the frequency for which $|L| = 1$.

A pure delay of Δt corresponds to $L_{nmp}(s) = \exp(-s \cdot \Delta t)$ which then gives $-\arg L_{nmp}(s = i\omega_{gc}) = \omega_{gc} \cdot \Delta t$ [4]. Thus, long delays are troublesome since they correspond to a pure loss of phase. For a pure real pole (or eigenvalue) of $\lambda = \sigma > 0$, $L_{nmp}(s) = (s + \sigma)/(s - \sigma)$ which then gives $-\arg L_{nmp}(s = i\omega_{gc}) = 2\arctan(\sigma/\omega_{gc})$ [4]. Thus, fast instabilities (large σ) are also troublesome because of the large phase loss.

For the case of insect flight, we have a pair of complex conjugate poles, $\lambda = \sigma \pm i\rho$, with $\sigma > 0$ signifying instability of the pitch dynamics. In this case, the phase loss each pole can be shown to be: $-\arg L_{nmp}(s = i\omega_{gc}) = 2\arctan(\sigma/(\omega_{gc} \mp \rho))$. Combining the two poles and delay together gives the following design inequality:

$$\omega_{gc} \cdot \Delta t + 2\arctan\frac{\sigma}{\omega_{gc} - \rho} + 2\arctan\frac{\sigma}{\omega_{gc} + \rho} \leq \pi/2. \tag{6.16}$$

For typical values of σ and ρ, very large values of the reaction time Δt render the inequality untrue for *all* gain-crossover frequencies $\omega_{gc} > 0$. If Δt is then decreased, at some point the relation becomes exactly equal for a single value of ω_{gc}. The value of Δt for which this occurs is the slowest delay time that confers the desired control performance. To compute this slowest permissible reaction

time, we wrote a program in MATLAB that first computes σ and ρ from the values of the physical time-scales. The program then finds the value of Δt that satisfies the equality of the above equation for at least one value of the frequency ω_{gc}. Thus, the permissible Δt is computed as a function of T_{P}, T_{PD}, and T_{FD}.

Estimating values for the physical time-scales. To assess stability of many insects, hummingbirds, and robots, we must estimate the physical time-scales T_{P}, T_{PD}, and T_{FD}. To provide an estimate of the pendular time $T_{\mathrm{P}} = \sqrt{I/Mgh}$, we need to know the morphological parameters M, I, and h. Body mass M is taken from the literature directly and moment of inertia is estimated as $I = M(L^2 + 3/4D^2)/12$ by approximating an insect's body as a cylinder of length L and diameter D. The center-of-drag distance h is taken to be the distance from the center-of-mass to the wing attachment point. This approximation is valid if the wings dominate other drag sources [32], such as the body itself or legs, or if these other sources are distributed nearly symmetrically about the wings. These morphological distances L, D, and h are available in the literature for some insects and can be estimated visually from photographs for others.

The forward damping time-scale T_{FD} is largely determined by wing drag [32]. To evaluate the resistance to forward motion, we approximate the instantaneous drag on the two wings by the high Reynolds number law $D = 2 \times \rho S C_D v^2/2$, where ρ is the fluid density, S is the wing area, C_D is the coefficient of drag, and v is the wing-speed relative to air. For forward flight, the resistive damping force arises from the faster wing-speed and thus greater drag on the forward sweep than on the backward sweep. For wings that beat at speed w relative to the body and a body moving with speed u, the forward dynamics

can be determined by averaging the drag for the two half-strokes:

$$\begin{aligned} D &= 2 \times \frac{1}{2}\rho S C_D \times \frac{1}{2}\left[-(w+u)^2 + (w-u)^2\right] \\ &\approx -2\rho S C_D w \cdot u = M\dot{u}. \end{aligned} \tag{6.17}$$

The approximation considers small body speeds and thus drops second-order terms, $(u/w)^2$. Thus, the wings act as a source of drag that is linear in body velocity. The forward damping time represents the characteristic time that motion is slowed and is given by:

$$T_{\mathrm{FD}} = \frac{u}{\dot{u}} = \frac{M}{2\rho S C_D w} = \frac{w}{2g} \cdot \frac{C_L}{C_D}. \tag{6.18}$$

Here, the final equality is a simplification that makes use of the hovering condition that body weight is balanced by lift: $Mg = L = 2 \times \rho S C_L w^2/2$, with a lift coefficient of C_L. Thus, we estimate the forward damping time-scale for different animals by determining the typical wing-speed w and lift-to-drag ratio C_L/C_D from the literature.

Finally, we must provide an estimate of the pitch damping time T_{PD}. Pitch rotational damping stems from different sources for different flyers. Most insects lack conspicuous damping sources, and the body itself thus provides weak damping due to viscous resistance [22]. Approximating the body as a cylinder of length L and diameter D, the torque τ is is linearly related to angular velocity ω,

$$\tau = \frac{\pi\mu L^3}{3\ln(L/2D)} \cdot \omega = I\dot{\omega}, \tag{6.19}$$

where $\mu = 1.8 \times 10^{-5}$ kg/m·s is the viscosity of air [22]. This formula applies to a slender cylinder rotated about its center, perpendicular to its long axis. The pitch damping time is thus given by

$$T_{\mathrm{PD}} = \frac{\omega}{\dot{\omega}} = \frac{I}{\frac{\pi\mu L^3}{3\ln(L/2D)}}, \tag{6.20}$$

where the moment of inertia can be estimated using the cylindrical-body approximation, $I = M(L^2 + 3/4D^2)/12$. Thus, pitch damping time can be estimated from the body dimensions.

In some cases there are additional, more conspicuous sources of pitch damping, such as the legs of some insects and the sail-like plates of flapping-wing robots. For long-legged insects, these sources generally dominate the rotational damping. To simplify the calculation of viscous drag on the 6 legs, we consider the drag on 3 legs that are twice as long and rotated about their centers. This allows us to make use of Eq. 6.19 to arrive at

$$T_{\mathrm{PD}} = \frac{I}{\frac{8\pi\mu L^3}{\ln(L/D)}}, \tag{6.21}$$

where I is the total body and leg inertia. Here, L and D now refer to the characteristic leg length and diameter.

For robots with large sails that damp body rotations, it is likely that the aerodynamic force on these structures is dominated by high Reynolds number, or quadratic, drag. To obtain a linear estimate of drag, we assume that the sails vibrate slightly in flight. In this case, the drag will be linear in velocity, just as is this case for flapping wings. By considering a sail as a point source of drag located a distance r from the center-of-mass, we find that

$$T_{\mathrm{PD}} = \frac{I}{r^3 \rho S C_D \omega}, \tag{6.22}$$

where I is the total body and sail moment, S is the sail area, $C_D \approx 1$ is the drag coefficient for a flat plate, ω is the angular vibration speed of the sail, and $\rho = 1.2$ kg·m^{-3} is the density of air.

Morphological and aerodynamic data for insects, hummingbirds, and robots. The calculations above allow us to estimate the relevant physical time-

scales given relatively few parameters for hovering insects, birds, and flapping-wing robots. This information is compiled in Tables 6.8 and 6.8. Table 6.8 includes all insects that lack clear damping surfaces, and Table 6.8 includes high-drag insects, hummingbirds, and robots.

As outlined above, the body length L and diameter D are needed to estimate T_{P}. T_{FD} can be estimated from the body mass M, the lift-to-drag ratio $C_{\mathrm{L}}/C_{\mathrm{D}}$, and rms wing speed at approximately two-thirds span: $w \approx \phi_0(2\pi f)R/2$, where ϕ_0 is the stroke amplitude, f the wing-beat frequency, and R the wing span length. Finally, for most flyers, T_{PD} can be calculated from the body morphological parameters M, L, and D. For some insects and robots, there are additional damping surfaces that must be included in the calculation of T_{PD}. These flyers are marked with a note in Table 6.8.

For the compact insects of Table 6.8, we note that $T_{\mathrm{P}} \sim \sqrt{L}$ while $T_{\mathrm{PD}} \sim L^2$ for isometrically-scaled insects of body length-scale L. Thus, we expect $T_{\mathrm{P}} \sim T_{\mathrm{PD}}^{1/4}$, which is consistent with our observations presented in the paper.

To our knowledge, reliable $C_{\mathrm{L}}/C_{\mathrm{D}}$ measurements have only been performed recently and are available for the fruit fly, hawkmoth, honeybee, and Rufous hummingbird. For each of the other animals and robots, we assume a value that corresponds to one of these animals that is closest in size. Body dimensions were not measured in the studies of orchid bees and hummingbirds, and these values have thus been estimated from photographs. Kinematic data is not available for the woolly aphid, so fruit fly parameters have been used. The elytra of ladybirds [37] and the hindlegs of bees [9] may serve to stabilize forward flight, but our calculations show that these structures contribute little to pitch damping during hovering.

Due primarily to estimates of morphological parameters, the forward damping and pendulum time-scales are expected to be accurate to better than a factor of 2 for most of these flyers. Pitch damping calculations are order-of-magnitude estimates because of the approximate drag laws used. The computation of reaction time, however, is rather insensitive to these errors.

Table 6.1: Morphological and aerodynamic parameters for compact insects.

	M (mg)	L (mm)	D (mm)	h (mm)	ϕ_0 (deg)	f (Hz)	R (mm)	C_L/C_D	I (kg·m^2)	T_{FD} (s)	T_{PD} (s)	T_{P} (s)
Ladybird, *Coccinella 7-punctata* [16, 17] □	34.4	8.2	2.1	1.1	89	54	11.2		2.0×10^{-10}	0.153	8.74	0.023
Honeybee, *Apis mellifera* [16, 17] □	101.9	15.9	2.7	3.3	66	197	9.8	1.8/2.3 [2]	2.2×10^{-9}	0.332	17.2	0.026
Bumblebee, *Bombus terrestris* [15] □	595	22.3	5.6	6.0	65	167	15.4		2.6×10^{-8}	0.436	57.3	0.027
Bumblebee, *Bombus hortorum* [16, 17] □	226	20.7	3.7	3.9	60	152	14.1		8.3×10^{-9}	0.343	28.5	0.031
Bumblebee, *Bombus lucorum* [16, 17] □	231	20.7	3.7	3.9	66	140	14.1		8.4×10^{-9}	0.348	28.8	0.031
Hoverfly, *Episyrphus balteatus* [28] □	21.8	11.3	2.8	1.3	37	166	9.0		2.4×10^{-10}	0.129	4.1	0.029
Dronefly, *Eristaltis tenax* [29] □	165.9	14.7	4.5	1.2	55	209	11.2		3.2×10^{-9}	0.329	21.1	0.041
Plume moth, *Emmelina monodactylus* [16, 17] □	8.4	8.7	1.0	2.1	84	33	11.1		5.4×10^{-11}	0.086	3.14	0.018
Hawkmoth, *Manduca sexta* male [52, 53] □	1199	45.6	7.3 [16]	8.7 [16]	57	26.1	47.3	1.2/0.6 [46]	2.1×10^{-7}	0.469	71.8	0.045
Hawkmoth, *Manduca sexta* female [52, 53] □	1833	43.5	7.0 [16]	8.3 [16]	59	25.9	51.0	1.2/0.6 [46]	2.9×10^{-7}	0.519	114	0.044
Fruit fly, *Drosophila melanogaster* [23] □	1.0	2.8	1.0	0.3	70	225	2.4	1.4/1.5 [12]	7.2×10^{-13}	0.120	0.597	0.015
Parasitic wasp, *Encarsia formosa* [51] □	0.025	0.60	0.22	0.08	65	385	0.66		8.3×10^{-16}	0.051	0.068	0.007
Orchid bee, *Euglossa dissimula* [13] □	91.0	10	3	1.5	52	214	8.8		8.1×10^{-10}	0.244	17.2	0.025
Orchid bee, *Euglossa imperialis* [13] □	151.7	13	5	2.5	53	189	10.9		2.4×10^{-9}	0.275	18.5	0.025
Orchid bee, *Eulaema meriana* [13] □	819.6	25	6	4.0	53	105	21.1		4.5×10^{-8}	0.289	72.7	0.037
March fly, *Bibio marci* female [18] □	65.4	15	3	0.7	70	100	11.2		1.3×10^{-9}	0.209	11.0	0.054
March fly, *Bibio marci* male [18] □	26.6	15	3	1.2	69	130	9.4		5.1×10^{-10}	0.225	4.30	0.040
Conopid fly, *Conops strigatus* [18] □	27.1	10.5	2	0.8	72	144	7.7		2.6×10^{-10}	0.216	6.59	0.035
Bluebottle fly, *Calliphora vicina* [18] □	62	10	4	0.6	69	135	9.2		5.8×10^{-10}	0.226	9.40	0.040
Black fly, *Simulium* Latreille [18] □	0.80	3.5	1.5	0.4	75	183	3.3		9.3×10^{-13}	0.148	0.325	0.017

Table 6.2: Morphological and aerodynamic parameters for high-drag insects, hummingbirds, and flapping-wing flying robots.

	M (mg)	L (mm)	D (mm)	h (mm)	ϕ_0 (deg)	f (Hz)	R (mm)	C_L/C_D	Drag	I (kg·m^2)	T_{FD} (s)	T_{PD} (s)	T_P (s)
Crane-fly, *Tipula obsoleta* [16, 17] ⋄	11.4	10.8	1.2	2.1	62	46	12.7		Legs	1.1×10^{-10}	0.093	0.249	0.022
Crane-fly, *Tipula paludosa* [16, 17] ⋄	49.8	18.1	1.8	3.9	60	58	17.4		Legs	1.4×10^{-9}	0.160	0.387	0.027
Mosquito, *Aedes aegypti* ⋄	3.5	4.4	0.6	0.3	25	470	3.2		Legs	5.7×10^{-12}	0.100	0.049	0.024
Woolly aphid, *Eriosomatina* ⋄	1.2	3.2	1.2	0.4			2.8		Coat	1.1×10^{-13}	0.140	0.003	0.015
Blue-throated hummingbird, *Lampornis clemenciae* [7] ∘	8400	120	20	14	76	23	85			1.0×10^{-5}	3.117	183	0.093
Magnificent hummingbird, *Eugenes fulgens* [7] ∘	7400	130	30	11	75	24	79			1.1×10^{-5}	2.984	130	0.117
Black-chinned hummingbird, *Archilochus alexandri* [7] ∘	3000	83	20	11	63	51	47			1.8×10^{-6}	2.982	79.2	0.075
Rufous hummingbird, *Selasphorus rufus* [6, 45] ∘	3300	80	15	7	82	52	42	1.2/0.2 [3]		1.8×10^{-6}	3.854	104	0.089
Mentor SF-2.5 [56] ⋆	580×10^3	344	86	88	90	30	180			6.0×10^{-3}	2.9	800	0.110
DelFly II [10, 11]⋆	16×10^3	210	10	20	48	13	140		Tail	5.9×10^{-5}	0.526	0.044	0.137
Cornell micro-air vehicle I [48, 47] ⋆	21.8×10^3	250	40	40	90	24	220		No sails	1.2×10^{-4}	3.2	249	0.119
	21.8×10^3	250	40	40	90	24	220		Sails	1.2×10^{-4}	3.2	0.010	0.112
Cornell micro-air vehicle II [31] ⋆	3.31×10^3	40	40	10	90	30	80		No sails	7.7×10^{-7}	1.5	213	0.049
	3.31×10^3	40	40	10	90	30	80		Sails	2.4×10^{-6}	1.5	0.005	0.079
Harvard micro-robotic insect [54] ⋆	60	15	5	5	50	110	15			1.3×10^{-9}	0.354	6.9	0.020

BIBLIOGRAPHY

[1] M. J. Abzug and E. E. Larrabee. *Airplane Stability and Control: A History of the Technologies That Made Aviation Possible*. Cambridge University Press, Cambridge UK, 2002.

[2] D. L. Altshuler, W. B. Dickson, J. T. Vance, S. P. Roberts, and M. H. Dickinson. Short-amplitude high-frequency wing strokes determine the aerodynamics of honeybee flight. *PNAS*, 102:18213–18218, 2005.

[3] D. L. Altshuler, R. Dudley, and C. P. Ellington. Aerodynamic forces of revolving hummingbird wings and wing models. *J. Zool. Lond.*, 264:327–332, 2004.

[4] K. J. Astrom. Limitations on control system performance. *Euro. J. Control*, 6:2–20, 2000.

[5] K. J. Astrom and R. M. Murray. *Feedback systems: An introduction for scientists and engineers*. Princeton University Press, Princeton, 2008.

[6] P. Chai, J. S. C. Chen, and D. Millard. Transient hovering performance of hummingbirds under conditions of maximal loading. *J. Exp. Biol.*, 200:921–929, 1997.

[7] P. Chai and D. Millard. Flight and size constraints: Hovering performance of large hummingbirds under maximal loading. *J. Exp. Biol.*, 200:2757–2763, 1997.

[8] H. Collewijn and J. B. J. Smeets. Early components of the human vestibulo-ocular response to head rotation: latency and gain. *J. Neurophysiol.*, 84:376–389, 2000.

[9] S. A. Combes and R. Dudley. Turbulence-driven instabilities limit insect flight performance. *PNAS*, 106:9111–9114, 2009.

[10] G. C. H. E. de Croon, K. M. E. de Clercq, R. Ruijsink, B. Remes, and C. de Wagter. Design, aerodynamics, and vision-based control of the delfly. *Int. J. Micro Air Vehicles*, 1:71–97, 2009.

[11] G. C. H. E. de Croon, K. M. E. de Clercq, R. Ruijsink, B. Remes, and C. de Wagter. Improving flight performance of the flapping wing mav delfly ii. *Int. Micro Air Vehicle Conf.*, 2010.

[12] M. H. Dickinson, F.-O. Lehmann, and S. Sane. Wing rotation and the aerodynamic basis of insect flight. *Science*, 284:1954–1960, 1999.

[13] R. Dudley. Extraordinary flight performance of orchid bees (apidae: Euglossini) hovering in heliox (80 he/20 o_2). *J. Exp. Biol.*, 198:1065–1070, 1995.

[14] R. Dudley. *The Biomechanics of Insect Flight: Form, Function, Evolution*. Princeton University Press, Princeton, 2000.

[15] R. B. Dudley and C. P. Ellington. Mechanics of forward flight in bumblebees. *J. Exp. Biol.*, 148:19–52, 1990.

[16] C. P. Ellington. The aerodynamics of hovering insect flight. ii. morphological parameters. *Phil. Trans. R. Soc. Ser. B*, 305:17–40, 1984.

[17] C. P. Ellington. The aerodynamics of hovering insect flight. iii. kinematics. *Phil. Trans. R. Soc. Ser. B*, 305:41–78, 1984.

[18] A. R. Ennos. The kinematics and aerodynamics of the free flight of some diptera. *J. Exp. Biol.*, 142:49–85, 1989.

[19] I. Faruque and J. S. Humbert. Dipteran insect flight dynamics. part 1: Longitudinal motion about hover. *J. Theor. Biol.*, 264:538–552, 2010.

[20] G. Fraenkel and J. W. S. Pringle. Halteres of flies as gyroscopic organs of equilibrium. *Nature*, 141:919–920, 1938.

[21] J. S. Freudenberg and D. P. Looze. Right half plane poles and zeroes and design tradeoffs in feedback systems. *IEEE Trans. Auto. Control*, 30:555–565, 1985.

[22] S. N. Fry, R. Sayaman, and M. H. Dickinson. The aerodynamics of free-flight maneuvers in drosophila. *Science*, 300:495–498, 2003.

[23] S. N. Fry, R. Sayaman, and M. H. Dickinson. The aerodynamics of hovering flight in drosophila. *J. Exp. Biol.*, 208:2303–2318, 2005.

[24] T. L. Hedrick and T. L. Daniel. Inverse problems in the flight control of the hawkmoth manduca sexta. *J. Exp. Biol.*, 209:3114–3130, 2006.

[25] M. Heisenberg and R. Wolf. The sensory-motor link in motion-dependent

flight control of flies. In *Visual Motion and its Role in the Stabilization of Gaze*, pages 265–283, Amsterdam, 1993. Elsevier.

[26] E. R. Kandel, J. H. Schwartz, and T. M. Jessell. *Principles of Neural Science*. McGraw-Hill, New York, USA, 2000.

[27] J. Kukalova-Peck. Origin and evolution of insect wings and their relation to metamorphosis, as documented by the fossil record. *J. Morph.*, 156:53, 1978.

[28] Y. Liu and M. Sun. Wing kinematics measurement and aerodynamic force and moment computation of hovering hoverfly. *Conf. Bioinform. Biomed. Eng.*, 2007.

[29] Y. Liu and M. Sun. Wing kinematics measurement and aerodynamics of hovering droneflies. *J. Exp. Biol.*, 211:2014–2025, 2008.

[30] J. W. S. Pringle. The gyroscopic mechanism of the halteres of diptera. *Phil. Trans. R. Soc. Lond. B*, 233:347–384, 1948.

[31] C. Richter and H. Lipson. Untethered hovering flapping flight of a 3d-printed mechanical insect. *12th International Conference on Artificial Life*, 2010.

[32] L. Ristroph, A. J. Bergou, J. Guckenheimer, Z. J. Wang, and I. Cohen. Paddling mode of forward flight in insects. *Phys. Rev. Lett.*, 2011.

[33] L. Ristroph, A. J. Bergou, G. Ristroph, K. Coumes, G. J. Berman, J. Guckenheimer, Z. J. Wang, and I. Cohen. Discovering the flight autostabilizer of fruit flies by inducing aerial stumbles. *PNAS*, 107:4820, 2010.

[34] L. Ristroph, G. J. Berman, A. J. Bergou, Z. J. Wang, and I. Cohen. Automated hull reconstruction motion tracking (hrmt) applied to sideways maneuvers of free-flying insects. *J. Exp. Biol.*, 212:1324–1335, 2009.

[35] J. Maynard Smith. The importance of the nervous system in the evolution of animal flight. *Evolution*, 6:127–129, 1952.

[36] A. Sourakov. Extraordinarily quick visual startle reflexes of the skipper butterflies (lepidoptera: Hesperiidae) are among the fastest recorded in the animal kingdom. *Florida Entomol.*, 92:653–655, 2009.

[37] M. M. De Souza and D. E. Alexander. Passive aerodynamic stabilization by beetle elytra (wing covers). *Physiol. Entomol.*, 22:109–115, 1997.

[38] A. K. Starosciak, R. P. Kalola, K. P. Perkins, J. A. Riley, and W. M. Saidel. Fast and singular muscle responses initiate the startle repsonse of pantodon buchholzi (osteoglossomorhpa). *Brain Behav. Evol.*, 71:100–114, 2008.

[39] G. Stein. Respect the unstable. *IEEE Control Systems Magazine*, 23:12–25, 2003.

[40] R. F. Stengel. *Flight dynamics*. Princeton University Press, Princeton, 2004.

[41] M. Sun, J. Wang, and Y. Xiong. Dynamic flight stability of hovering insects. *Acta Mech. Sin.*, 23:231246, 2007.

[42] M. Sun and Y. Xiong. Dynamic flight stability of a hovering bumblebee. *J. Exp. Biol.*, 208:447459, 2005.

[43] G. K. Taylor. Mechanics and aerodynamics of insect flight control. *Biol. Rev.*, 76:449–471, 2001.

[44] G. K. Taylor and A. L. R. Thomas. Dynamic flight stability in the desert locust schistocerca gregaria. *J. Exp. Biol.*, 206:28032829, 2003.

[45] B. W. Tobalske, D. R. Warrick, C. J. Clark, D. R. Powers, T. L. Hedrick, G. A. Hyder, and A. A. Biewener. Three-dimensional kinematics of hummingbird flight. *J. Exp. Biol.*, 210:2368–2382, 2007.

[46] J. R. Usherwood and C. P. Ellington. The aerodynamics of revolving wings i. model hawkmoth wings. *J. Exp. Biol.*, 205:1547–1564, 2002.

[47] F. van Breugel, W. Regan, and H. Lipson. From insects to machines: A passively stable, untethered flapping-hovering micro air vehicle. *IEEE Robotics and Automation Magazine*, 15:68–74, 2008.

[48] F. van Breugel, Z. E. Teoh, and H. Lipson. *A passively stable hovering flapping micro-air vehicle. In D. Floreano et al. (Eds.), Flying Insects and Robots*. Springer, 2007.

[49] J. T. Vance and J. S. Humbert. Mechanisms of gust rejection in the honey bee, apis mellifera. *Soc. Integ. and Comp. Biol.*, 2010.

[50] W. G. Vincenti. How did it become 'obvious' that an airplane should be inherently stable? *Invention and Technology*, pages 51–56, 1988.

[51] T. Weis-Fogh. Quick estimates of flight fitness in hovering animals, including novel mechanisms of lift production. *J. Exp. Biol.*, 59:169–230, 1973.

[52] A. P. Willmott and C. P. Ellington. The mechanics of flight in the hawkmoth manduca sexta i. kinematics of hovering and forward flight. *J. Exp. Biol.*, 200:2705–2722, 1997.

[53] A. P. Willmott and C. P. Ellington. The mechanics of flight in the hawkmoth manduca sexta ii. aerodynamic consequences of kinematic and morphological variation. *J. Exp. Biol.*, 200:2723–2745, 1997.

[54] R. J. Wood. First take-off of a biologically-inspired at-scale robotic insect. *IEEE Trans. on Robotics*, 24:341–347, 2008.

[55] Zanker. Wingbeat of drosophila melanogaster i. kinematics. *Phil. Trans. R. Soc. Lond. B*, 327:1–18, 1990.

[56] P. Zdunich, D. Bilyk, M. MacMaster, D. Loewen, J. DeLaurier, R. Kornbluh, T. Low, S. Stanford, and D. Holeman. Development and testing of the mentor flapping-wing micro air vehicle. *J. Aircraft*, 44:1701–1711, 2007.

CHAPTER 7

INVERTED DRAFTING OF INTERACTING FLAPPING FLAGS

7.1 Summary

In aggregates of objects moving through a fluid, bodies downstream of a leader generally experience reduced drag force[1]. This conventional drafting holds for objects of fixed shape, but interactions of deformable bodies in a flow are poorly understood, as in schools of fish. In our experiments on "schooling" flapping flags we find that it is the leader of a group who enjoys a significant drag reduction (of up to 50%), while the downstream flag suffers a drag increase. This counterintuitive inverted drag relationship is rationalized by dissecting the mutual influence of shape and flow in determining drag. Inverted drafting has never been observed with rigid bodies, apparently due to the inability to deform in response to the altered flow field of neighbors.

7.2 Aero- and Hydro-Dynamic Interactions Between Moving Bodies

Groupings of bodies moving through a fluid often exhibit collective behavior. Locomotion provides well-known examples including the maneuvering and clustering of racing automobiles [15] and bicyclists [12] and the queuing of lobsters during ocean floor migrations [7]. These phenomena are explained

[1]The work presented in this chapter is modified with permission from Ristroph and Zhang, *Phys. Rev. Lett.*, **101**, 194502 (2008).

by conventional hydrodynamic drafting, for which rigid bodies enjoy drag reduction when situated behind a leader in a flow [22]. Though the flow field around drafting bodies is complicated, the effect is qualitatively understood by considering that the downstream body sits in the lower velocity wake of the leader. The resulting force arrangement leads to passive aggregation and offers net drag reduction for locomotors.

Does this rationalization of interactions among rigid objects extend to aggregates of flexible, shape-changing bodies? Schooling fish [21] and flocking birds [9] are striking examples in which fluid and dynamic structures conspire to support long length-scale coherent motion [18]. Understanding such phenomena is challenging because of the mutual influence of deformability and unsteady fluid flow [20, 4, 23]. The flapping of a flag is an everyday example that serves as an archetype of interactions between flow and deformable structure [23]. Certainly, the changing shape of a flexible body affects the resistive force it must overcome when moving through a fluid [4]. Moreover, when deformable bodies condense into an aggregate state, fluid-mediated interactions may lead to modifications of shape and, hence, modifications in force. Here, we reveal an instance of the dramatic effect of deformability in the interaction of flapping flags in a fast flow.

7.3 "Schooling" of Flapping Flags

To experimentally model the interaction of shape-changing bodies, we insert thin flexible filaments into a flowing soap film [1]. Each filament is fixed at its upstream end to a thin wire, a flagpole that extends out of the film, while the rest of the thread hangs free in the film. Because the filaments are suffi-

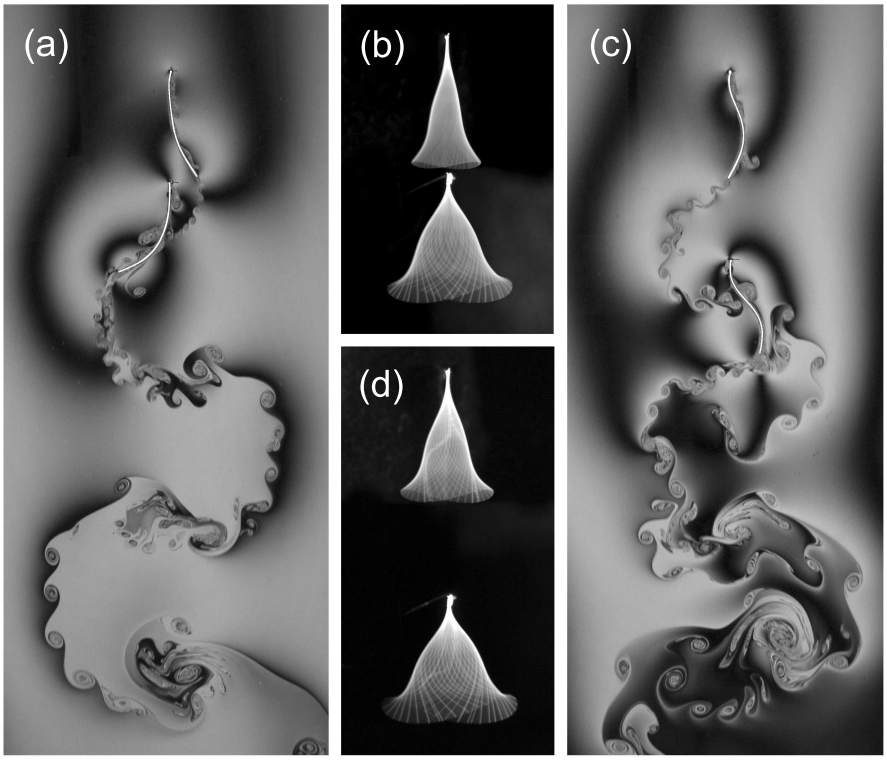

Figure 7.1: A pair of tandem flags undulate in a downward, flowing soap film. (a), (c) At different separations G, instantaneous flow patterns around the flapping flags are visualized by thin-film interferometry. (b), (d) The periodic motion is captured by long time exposure photographs. When the separation gap is zero ($G/L = 0$), the wakes of the two flapping bodies are united into a coherent structure (a) which is similar to the wake of a single flag [23]. The flags take on different lateral amplitudes (b), small for the leading flag and large for the trailing one. At a larger separation ($G/L = 0.6$), the flag wakes disentangle (c) and both amplitudes increase (d).

ciently flexible and inertial, they spontaneously flap under the fluid forcing, as one-dimensional flags fluttering in a two-dimensional breeze [23, 17, 6]. These threads have diameter 0.03 cm, length $L = 2.0$ cm, bending modulus 0.34 $\mathrm{g \cdot cm^3/s^2}$, and mass per unit length 4.8×10^{-4} g/cm; they flap in a flow of far-field speed $U = 200$ cm/s. First, consider the undulations of a lone flag. In a uniform flow, the flapping motion is well-described by a traveling wave of increasing spatial envelope [23]. For the above material properties and flow speed, the undulatory motion of a flag exhibits maximum amplitude $A_0 = 1.36$ cm (the to-

tal excursion of the free end) and flapping frequency f_0 = 35.8 Hz. In addition to these kinematic quantities, we measure the time-averaged stream-wise fluid force, $D_0 = 5.2\ \mathrm{g \cdot cm/s^2}$, the drag on an isolated flag [2].

We then insert a second flag into the flow. Depending on the relative location of the bodies, each may be presented with a modified flow field. Hydrodynamic interactions will, in general, alter both the form of the flapping motion [23, 8, 11], captured as amplitude A and frequency f on each body, as well as the fluid force, D. At the high Reynolds number (Re $\sim 10^4$) studied here, the primary influence of an object on a flow is downstream, yielding the complex wake of the body [19]. Thus, the queuing of bodies in the direction of flow is the simplest arrangement that is likely to lead to strong fluid-mediated interactions.

7.4 Interactions Between Tandem Flapping Flags

To study these interactions, we arrange a tandem pair of identical flags and vary the gap between the two. The gap G is the stream-wise distance between the tail end of the leading flag and the flagpole of the following flag, or, equivalently, the distance between flagpoles less one body length L. The instantaneous form of the two filaments for non-dimensional gap $G/L = 0$ and the corresponding wake structure are captured in the photograph of Fig. 7.1(a). The two bodies assume the same frequency of flapping but take on different amplitudes, as revealed in the long time exposure photograph of Fig. 7.1(b). For $G/L = 0$, the flags flap out-of-phase. At a greater separation of $G/L = 0.6$, flapping amplitudes increase [Fig. 7.1(d)], the phase difference is nearly zero, and the wake structure [Fig. 7.1(c)] becomes more complex. We found that the tandem flags

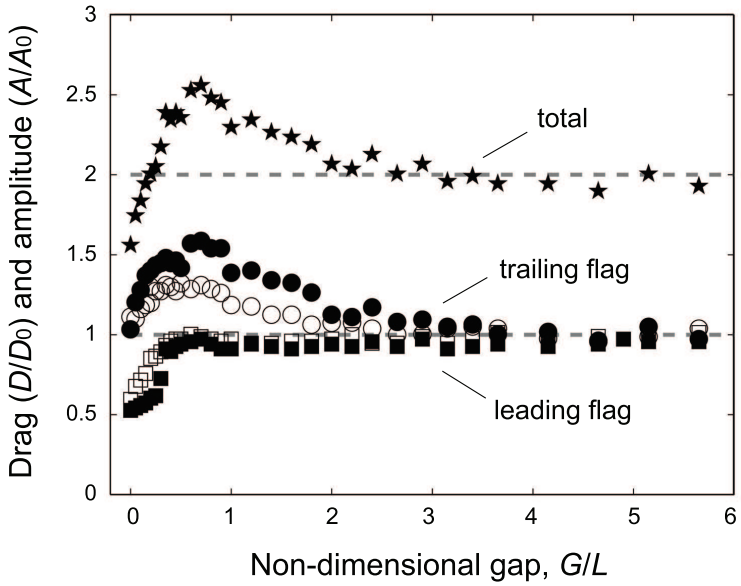

Figure 7.2: Stream-wise fluid force D for two tandem flags as a function of non-dimensional separation G/L. At all separations investigated, the leading flag (open triangles) experiences a lower drag than the follower (solid triangles). In particular, at small separations, the drag on the leader is significantly lower than that of a single, isolated flag (D_0, as indicated by the lower dashed line). In contrast, the follower experiences a higher than usual drag. Compared to the total drag of two independent flags (the upper dashed line), the total drag for our tandem flags (solid circles), which is the sum of the data from two lower curves, is reduced for small gaps and amplified at larger separations.

synchronize even when separated by several body lengths. This correlated motion suggests that the fluid-coupled interactions may also lead to altered forces that persist over long lengths.

We first compare the drag force for each member of the pair. The individual flag forces as a function of gap are shown in Fig. 7.2. In surprising opposition to static objects, we find that the leader always suffers *less* drag than the downstream body. In particular, the leading body experiences less drag than that of an isolated flag, D_0, including a reduction to half at $G/L = 0$. The downstream body has drag greater than D_0. Defying intuition based on fixed bodies, flexible flags experience *inverted drafting*, in which flapping in front reduces fluid forces.

How does this anomalous allotment of drag arise? One might conceive of a scenario in which each flag modifies its surrounding flow *and also* in turn induces changes in the form of motion of the other flag. The latter effect is not possible for rigid objects and is thus a good candidate to explain our new results. Indeed, the flags do have altered dynamics in the aggregate, as is clear from Fig. 7.1. In particular, detailed measurements of frequency and amplitude reveal two consistent observations. First, the frequency, though somewhat different from the value for the lone flag, is the same for each flag as long as the two were placed within a few body lengths of one another. Second, we find that amplitude is strongly dependent on position and is smaller for the leader than the follower, as is evident in Fig. 7.1(b) and (d).

For this two-flag interaction problem, drag might assume a complicated form that is dependent on the undulatory flag motion and the unsteady near-body flow. We decouple shape and flow by considering the drag on an object of fixed shape and then estimate how this force depends on the ever-changing shape. For high Reynolds number steady flows, the form drag [19] on a static body is $C_D \rho U^2 S/2$. Here, ρ is the fluid density, S the area the object presents to the flow, and C_D the drag coefficient, a shape-dependent parameter of order unity. Thus, shape appears both through the area S and the coefficient C_D. A scaling approximation for S can be obtained by taking the area presented to the flow to be the product of the film thickness d and flapping amplitude A, so that $S \sim dA$. If the drag coefficient is relatively constant, then Drag ~ Amplitude.

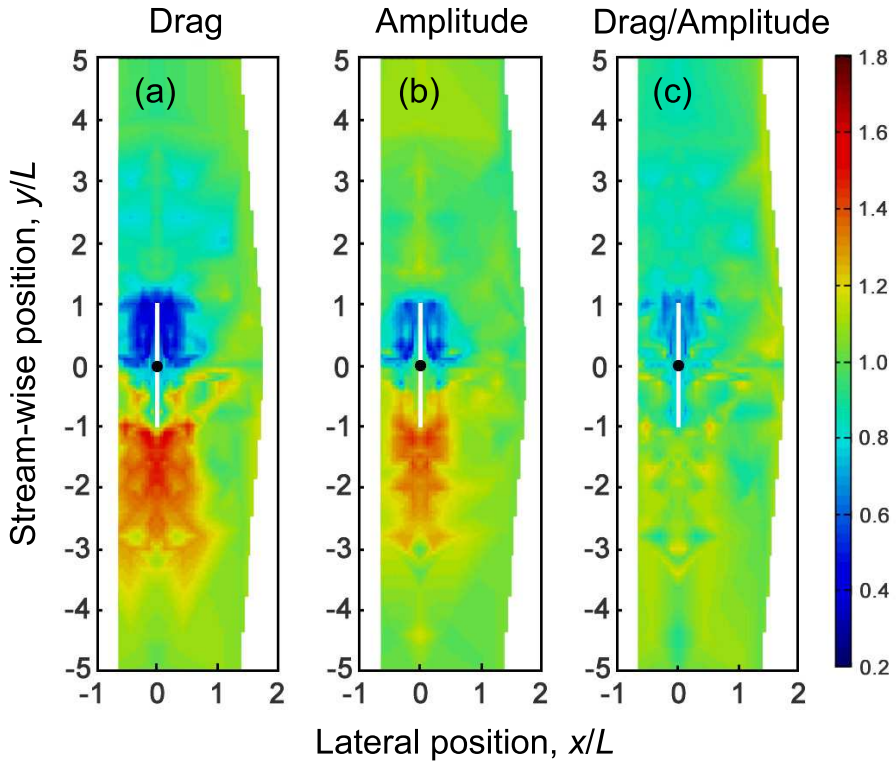

Figure 7.3: Two-dimensional maps of the drag and amplitude for two flapping flags. Here, the flagpole of one flag is fixed at the origin (black dot) while the second flag is displaced laterally and stream-wise. The stream-wise drag (a) and the flapping amplitude (b) are measured for the second flag. The force map (a) shows a robust drag reduction for the second flag when placed upstream of the first. The second flag experiences, over a greater area, an increased drag when downstream of another flag. There is a strong correlation of the lateral flapping amplitude (b) with the drag (a), as indicated by the more uniform map of drag normalized by amplitude (c). (All maps are normalized by the corresponding values for an isolated flag at the same flow conditions.)

7.5 Generalization to Arbitrary Locations

We verify that drag and amplitude are correlated for two flags of both stream-wise and lateral displacement. To demonstrate this, we fix a flag at the origin and measure the drag on a second, nearby flag at varying relative locations. Here, position indicates the displacement between flagpoles. Fig. 7.3(a) shows the map of drag on the flag that is displaced laterally and stream-wise, and

Fig. 7.3(b) shows the amplitude map. By comparison, the amplitude of flapping is seen to correlate quite well with the fluid force experienced. In fact, the quantity Drag/Amplitude yields the nearly uniform map of Fig. 7.3(c). Amplitude alone seems to capture the essential shape-dependence of drag. Thus, for tandem flags, inverted drafting reveals itself in the small amplitude for the leading body and considerably broader envelope for the downstream flag, as in Fig. 7.1(b) and (d).

Notice also that the inverted drafting of tandem flags is robust to moderate lateral displacement of the flags. Specifically, significant drag reduction for the leader extends upstream over one body length from the origin and more than a half body length to each side [Fig. 7.3(a)]. The region of higher drag persists four flag lengths downstream and nearly one body length laterally. Taken together, these results indicate that inverted drafting is not sensitive to the exact alignment of the flags but is a result of a broad change in the near-body flow field of the flags.

7.6 Inverted Drafting as a Fluid-Structure Resonance

We then ask how the flow field induces changes in the amplitude of flapping. We first address how the amplitude of the leading flag is reduced, considering the introduction of its downstream neighbor and the flow-flag interaction. Because the downstream flag is held fixed by a flagpole, this follower serves to suppress lateral flow near the trailing end of the leading flag. The free end of the leading flag can be viewed as part of the overall flow structure, namely a concentrated vortex sheet [17, 6], and is thus indirectly confined in the lateral

direction. As a result, the leading flag presents a smaller cross-sectional area to the oncoming flow, which in turn yields a drag that is less than that on an isolated flag. Here, the role played by the downstream flag is similar to that of a wake-splitter, a longitudinal plate that reduces drag on an upstream cylinder [5].

Next, consider the flow field near the downstream flag. This follower undulates in the oscillating wake of the leader. Because the flags beat in synchrony, the following flag flaps at the same frequency at which its oncoming flow oscillates. The resonance effect thus drives the lateral amplitude to increase. The broad amplitude presented to the flow thus yields higher drag for the follower.

Though the follower bears the greater drag burden, the pair as a whole can have a drag reduction or increase. This again differs from rigid objects: studies on tandem cylinders reveal that the total drag is always less than that of two independent bodies [22]. For interacting flags, the pair drag (Fig. 7.2) shows an unusual dependence on gap. For gaps $G/L < 0.2$, the total force on the pair is less than that of two independent flags, but at greater separations ($0.2 < G/L < 3$) drag is considerably amplified. The flow visualization of Fig. 7.1(a) and (c) offers additional clues to the underpinning of the drag reduction for the aggregate. When tandem flags are close enough to yield drag reduction, the wake of the pair is united into a sinuous, narrow ribbon of vortices that resembles the wake of a single flag [23]. For larger separations, the wake disentangles and widens, and the drag reduction for the pair vanishes. Here the wake width serves as an indicator of drag, which is equal to the rate of removal of fluid momentum.

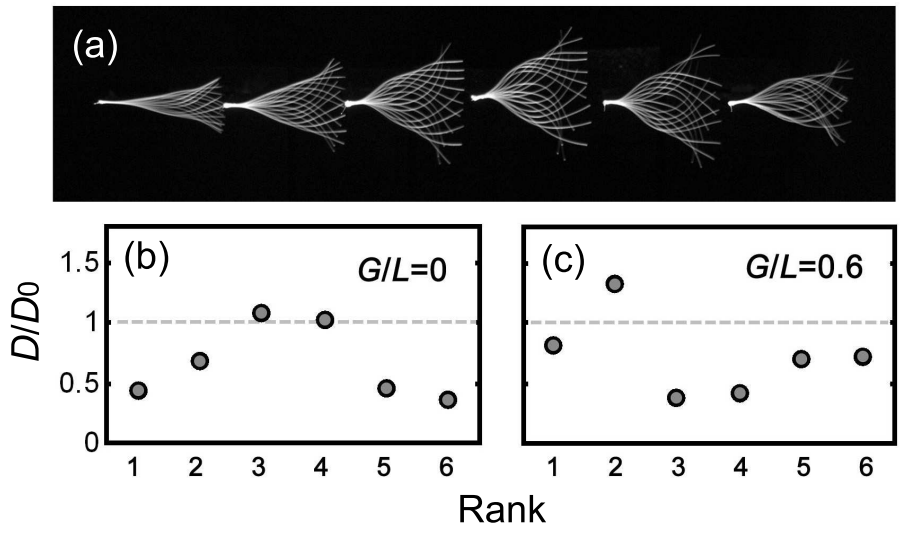

Figure 7.4: Drag measurements of six tandem flags at different separations. (a), Photograph of flapping motion for $G/L = 0$, where flow is from left to right. (b), (c) Drag for each individual flag is shown for two separations. The first flag enjoys a drag reduction compared to the second, meaning inverted drafting persists in these larger aggregates. The group experiences a drag reduction as a whole, as most individuals have drag less than D_0.

7.7 Generalization to Many Flags

Having investigated pairs of flags, we generalize to larger tandem aggregates. In Fig. 7.4(a), we show six serial flags at $G/L = 0$ photographed under strobe lighting. In this larger aggregate, all bodies flap at the same frequency but assume different phases and amplitudes. Across different separation distances, the leading flag enjoys a lower drag than its downstream neighbor, as is detailed in Fig. 7.4(b) and (c). However, we find that flapping amplitude no longer gives a clear indication of force, perhaps because the local flow speed deviates considerably from the far-field value of U. Nevertheless, that inverted drafting persists in these larger groupings suggests that our rationalization of the two-flag problem offers general insight into the forces on interacting, passively deformable bodies.

7.8 Implications

It is unknown whether inverted drafting appears in interactions of *actively* flapping bodies, as schooling fish. Though a flag flaps passively and a swimming fish undulates by muscular activation, both motions involve the interplay of fluid forcing, elasticity, and inertia [23, 10, 14]. In fact, fish do make use of passive hydrodynamics in unsteady flows for energetic advantage [13]. Presently, nearly all rationalizations of grouping energetics of flapping animals assume no advantage for leading members [21, 9]. Such models do not consider any modified dynamics in an aggregate; the motion of a fish, for example, is assumed to be the same in a school as it is during isolated swimming. However, it is known that the form of flapping motion varies according to position in a school and flock [9]. In light of our findings, the altered collective dynamics may lead to dramatic deviations from these models that simply superpose isolated locomotors.

Another class of models describe collective behavior of living organisms by considering forces of interactions between individuals [3]. Often without explicit reference to an underlying mechanism, some models combine a short-range repulsive force and longer-range attraction, yielding an equilibrium separating distance between members of an aggregate. For tandem flags, inverted drafting directly suggests hydrodynamic repulsion between flags. Because the follower has higher drag, the pair will tend to separate further. This is unlike rigid objects, for which conventional drafting implies attraction in the tandem arrangement. Thus, the individual forces on tandem flags are such that aggregation is unstable. Notice also that these forces are so arranged as to hinder a flapping "predator" flag in its pursuit of "prey", the leader. If racecars had

flexible spoilers, for example, then the leading car might make use of inverted aerodynamic drafting to maintain its position. In this case, it is better to be chased than to chase.

BIBLIOGRAPHY

[1] The flowing soap film is used a planar water tunnel [23, 4] and is well-described by two-dimensional hydrodynamics. (See [16] and references therein.) Driven by gravity, soapy water descends between two lines spaced 9.5 cm apart. Due to air drag on the film, the flow reaches a terminal velocity, $U = 200$ cm/s, and a nearly constant velocity profile (within 95% over test section). The film thickness is $d = 4.7$ μm. For filaments of length $L = 2.0$ cm, we operate at Reynolds number $\mathrm{Re} = UL/\nu \sim 10^4$, where $\nu \sim 0.04$ cm^2/s is the kinematic viscosity of the fluid.

[2] The flagpole is fixed to a cantilever which bows slightly (< 0.5 mm) under the fluid forcing of the flag. The deflection is measured optically [4]. The flat cantilever suppresses lateral motion, and stream-wise force fluctuations are damped by a viscous dashpot attached to the beam.

[3] Fish: C. M. Breder, Ecology **35**, 361 (1954); generalized self-propelled particles: T. Vicsek, A. Czirik, E. Ben Jacob, I. Cohen, and O. Shochet, Phys. Rev. Lett. **75**, 1226 (1995) and I. D. Couzin, J. Krause, N. R. Franks, and S. A. Levin, Nature **433**, 513 (2005); sperm: I. H. Riedel, K. Kruse, and J. Howard, Science **309**, 300 (2005).

[4] S. Alben, M. Shelley, and J. Zhang. Drag reduction through self-similar bending of a flexible body. *Nature*, 420:479, 2002.

[5] C. J. Apelt, G. S. West, and A. A. Szewczyk. *J. Fluid Mech.*, 61:187, 1973.

[6] M. Argentina and L. Mahadevan. Fluid-flow-induced flutter of a flag. *Proc. Natl. Acad. Sci. U.S.A.*, 102:1829, 2005.

[7] R. G. Bill and W. F. Herrnkind. Drag reduction by formation movement in spiny lobsters. *Science*, 193:1146–1148, 1973.

[8] D. J. J. Farnell, T. David, and D. C. Barton. Coupled states of flapping flags. *J. Fluid Structs.*, 19:29, 2004.

[9] F. E. Fish. Energetics of swimming and flying in formation. *Comments Theor. Biol.*, 5:283, 1999.

[10] G. Huber. Swimming in flatsea. *Nature*, 408:777, 2000.

[11] L.-B. Jia, F. Li, X.-Z. Yin, and X.-Y. Yin. Coupling modes between two flapping filaments. *J. Fluid Mech.*, 581:199, 2007.

[12] C. R. Kyle. Reduction of wind resistance and power output of racing cyclists and runners travelling in groups. *Ergonomics*, 22:387, 1979.

[13] J. C. Liao, D. N. Beal, G. V. Lauder, and M. S. Triantafyllou. Fish exploiting vortices decrease muscle activity. *Science*, 302:1566, 2003.

[14] U. K. Muller. Fish 'n flag. *Science*, 302:1511, 2003.

[15] C. F. Romberg, Jr. F. Chianese, and R. G. Lajoie. Aerodynamics of race cars in drafting and passing situations. *Soc. Auto Eng.*, page 710213, 1971.

[16] M. A. Rutgers, X. L. Wu, and W. B. Daniel. Conducting fluid dynamics experiments with vertically falling soap films. *Rev. Sci. Inst.*, 72:3025, 2001.

[17] M. Shelley, N. Vandenberghe, and J. Zhang. Heavy flags undergo spontaneous oscillations in flowing water. *Phys. Rev. Lett.*, 94:094302, 2005.

[18] R. A. Simha and S. Ramaswamy. Hydrodynamic fluctuations and instabilities in ordered suspensions of self-propelled particles. *Phys. Rev. Lett.*, 89:058101, 2002.

[19] D. J. Tritton. *Physical Fluid Dynamics*. Oxford University Press, New York, 1988.

[20] S. Vogel. *Life in Moving Fluids*. Princeton University Press, Princeton, 1994.

[21] D. Weihs. Hydromechanics of fish schooling. *Nature*, 218:918, 1973.

[22] M. M. Zdravkovich. Review of flow interference between two circular cylinders in various arrangements. *J. Fluids Eng.*, 99:618, 1977.

[23] J. Zhang, S. Childress, A. Libchaber, and M. Shelley. Flexible filaments in a flowing soap film as a model for one-dimensional flags in a two-dimensional wind. *Nature*, 408:835, 2000.

CHAPTER 8

CONCLUSIONS AND OUTLOOK

8.1 Synthesis

Collectively, these investigations provide a template for dissecting the problems involved in maneuvering and stabilization of flight in insects. We have put together experimental and analytical techniques that quantify the nature of these remarkable flight behaviors and reveal some of the solutions that insects have evolved in interacting with their aerial environment. Having dissected the many levels involved, the next step is to put these elements back together. Here, I will outline how this synthesis is done for the specific case of yaw stabilization in fruit flies.

A description of yaw stabilization must include the roles of several key players: the mechanosensory halteres, neural circuits, wing muscles and hinge, motion of the wings, aerodynamic forces, and the resulting body rotational dynamics. The interaction of these elements forms a closed loop of information flow. At each step in the loop, a given process can be viewed as a transfer function that converts one quantity into another. In the context of our simplest reduced-order models, these transfer functions are linear operators, and the entire feedback loop can be written as a system of linear differential equations.

The individual transfer functions will take on simple forms. For the halteres, we model their complex dynamics as faithfully recording yaw rate, $\dot{\psi}$ [5]. This signal feeds into a neural circuit that drives a time-delayed position and rate muscular response [6]: $\Delta\eta_0 \sim \psi(t - \Delta t) + \dot{\psi}(t - \Delta t)$. Here, $\Delta\eta_0$ is the difference

in spring rest angles in the biomechanical wing hinge model and Δt is a neural-sensory delay time. The actuation bias leads to paddling motions [1]: $\Delta\alpha = \Delta\eta = \mu \cdot \Delta\eta_0$ with $\mu \approx 0.6$. These wing motions give rise to a torque on the insect body which then must overcome the damped, inertial dynamics [6, 1]. Finally, the yaw rate is again sensed by the halteres and the information flow continues in this loop.

Combining these elements into a single differential equation, we arrive at

$$I\ddot{\psi} = -\beta\dot{\psi} + N_{\text{fly}} + N_{\text{ext}} \tag{8.1}$$

where N_{ext} is the externally-imposed torque and

$$N_{\text{fly}}(t) = \gamma \cdot \Delta\alpha(t) = \gamma\mu \cdot \Delta\eta_0(t) = K_{\text{P}}\psi(t - \Delta t) + K_{\text{D}}\dot{\psi}(t - \Delta t) \tag{8.2}$$

is the response torque. Here, we have written the fly's response torque in several equivalent ways to emphasize the roles of the different systems that generate it. At the level of the wing motions, the torque is proportional to the paddling angle $\Delta\alpha$. At the actuation level, the torque is also proportional to the bias angle $\Delta\eta_0$. At the sensory and neural levels, the response is proportional to the time-delayed yaw plus yaw-rate.

This stabilization model could also be implemented in the more-inclusive computational simulations. In this case, the physical processes would be determined by the simulation instead of modeled with reduced-order equations. With regard to the neural controller and muscular strain, there are different ways to implement these elements in simulation. For example, the instantaneous yaw might be used directly or the stroke-averaged value might serve as the input to the neural controller. At this time, this full simulation is in progress and may be presented in complete form elsewhere.

More generally, the general structure to this problem of yaw control in fruit flies may be shared by many complex behaviors of animals. Our approach should provide a template for understanding this rich class of problems.

8.2 Extensions and Expansions

Within the insect flight field of research, this work naturally leads in several directions. One avenue would be to extend the analyses presented here to other degrees-of-freedom in the motion of the insect. A second avenue would be to conduct similar studies on other insects. Finally, I believe some of the most powerful results will come from experimental manipulation of the body plans, wings, and sensors of actual insects.

It is natural to build on the yaw control and stabilization work in order to investigate the pitch and roll response of fruit flies. For body pitch, we have shown preliminary evidence that the insects respond by shifting the point about which they beat their wings [12]. Beating in front, for example, causes the lift on the wings to generate a nose-up pitch torque. However, we still do not know what type of controller is used nor the actuation mechanism during pitch stabilization. These features are of particular interest given that body pitch is intrinsically unstable. On-going work in the group involves the use of free-flight data as well as magnetic perturbation experiments to extract these mechanisms.

For body roll, it is suspected that flies use differential stroke amplitudes to generate torque [8]. As for pitch, work has now begun on magnetically perturbing flies about their roll axis to confirm this idea and also to extract the roll control strategy. Theoretical work from other groups suggests that roll is weakly

damped and intrinsically stable with regard to angle itself [3]. This makes roll dynamics inherently different from yaw, in which motion quickly damps out but angle itself is not restored. Roll is also different from pitch, which is unstable. Thus, no active response would be needed to control roll, and in this sense, it is expected to be the easiest degree-of-freedom to maintain.

One may also extend the work on maneuvering flight to evaluate how flies change their translational degrees-of-freedom. In this thesis, we presented results on specific modes of sideways flight, forward flight, and turning all of which involve paddling wing motions. However, these are not the only modes exhibited by flies. In particular, flies often tilt their body in pitch during forward flight and in roll during sideways flight. These qualitative observations lead to many questions. What are the maneuvering dynamics for other modes of translation? When do insects use different modes and why? What control schemes are used for translation? In particular, what sensors are used to maintain flight speed? Some of these questions might be addressed by devising an experimental procedure for exerting forces to flying insects.

With regard to ascending flight, work is nearing completion that clearly shows that fruit flies increase stroke amplitude on both wings to ascend at higher speeds.

Another challenge involves the coordination of all of these degrees-of-freedom. How are different body orientation angles controlled simultaneously? To address this question, I have constructed a set-up that is capable of applying two torque perturbations offset by a delay. This could be used, for example, to rapidly follow a yaw perturbation with a pitch perturbation. This would determine if the two responses are simply linearly superposed, for example, or if the

insect chooses a more complex route through the three Euler angles in order to regain its posture.

It also remains open as to how well the findings for fruit flies carry over to other insects. Certainly, all of the maneuvering dynamics and stabilization work could be carried out for different insects. In this respect, I find the exploration of flight control for insects of varying body plans to be the most interesting pursuit.

Perhaps one of the most appealing frontiers involves the study of very small insects, those less than a millimeter in size [10]. First, the Reynolds numbers are quite low for these insects, on the order of tens, and there may be interesting aerodynamics at these scales. Second, the wings of very small insects have unusual features, such as a bristle-like structure connected to a central stalk. Finally, the work on pitch stability presented here predicts extremely fast neural reaction times would be needed to stabilize these small body plans. Perturbation experiments on such insects may well discover some of the fastest behavioral response times in the animal kingdom.

I also believe that manipulation of actual insects is a powerful though technically difficult way to explore aspects of flight behavior. In the pitch stability work, we began efforts in this spirit by disabling sensors and restoring flight stability passively by adding draggy fibers onto the bodies of these insects. Work in progress involves altering the center of mass location by adding weights on the top of fruit flies. Preliminary results indicate that physical stability is sensitive to the location of the center of mass relative to wing location. However, it appears that actual insects compensate for this change quite well using their active control schemes.

Many other manipulation experiments await exploration. At the beginning of my insect flight work, I tried mechanically manipulating the actual halteres of insects with the hope of being able to "steer" them in flight. I managed to glue magnetic pins onto the halteres of a crane-fly – fruit flies are far too small for this work – but the fly never took to flight after the operation. I also conducted wing-clipping experiments in which parts of one or both wings were removed. Fruit flies take symmetric and asymmetric clipping in stride. A fly with both wings cut to nearly half area can still ascend. A fly with half of one wing removed hovers and turns with remarkable control.

We have also carried out preliminary work that is in this spirit with mosquitoes. Mosquitoes fly with all six legs extended and preliminary calculations indicate that the drag on the legs may enhance passive stability. Indeed, when the legs are removed our videos show body oscillations that are eventually either damped out or overcome with an active response. These oscillations occur in roll, and ongoing work is aimed at investigating their origin and ultimate stabilization.

8.3 Experimental Methods: Where Are We Now?

The simplest way to improve the experimental apparatus is to simply add more cameras to the current three. Fortunately, the price of high-speed cameras are quickly dropping in price, so this strategy is becoming increasingly feasible. The more views would greatly improve the reconstruction of posture during flight. In addition, the camera calibration procedure should be automated. There already exist standard packages – available for Matlab, for example – for calibrat-

ing a set of cameras. This would eliminate the need to manually position each camera to great precision.

The Hull Reconstruction Motion Tracking (HRMT) technique could be greatly improved upon [7]. Probably, the most fruitful direction would involve a thorough examination of current computer vision techniques. Certainly, there is information in the videos that is not being used in the HRMT method. For one, HRMT treats each frame individually and makes no use of time information. This could be exploited, for example, by using previous positions and orientations to estimate the current values. Also, the wings are somewhat distinguishable from the opaque body because they are translucent. This might be exploited in the image processing step in which the wings are dissected from the body.

Additionally, one might consider tracking algorithms that are conceptually very different from HRMT. The most promising is perhaps a model-based tracker. In this algorithm, a model is formed and given certain degrees-of-freedom. The model is then oriented and positioned until it best matches the video observations according to some metric. Currently, our collaborator Attila Bergou is pursuing this approach for bat flight using an approach that should generalize to insect flight.

Once flight data is collected, one may want to formalize the discovery procedures presented here. I have largely made discoveries by careful and repeated observations of the movies and by trying different types of models (PID controllers, for example) to match the observations. For many problems, this could be formalized in a rigorous way. For example, controller types might be found by using system identification techniques that are common in control theory or

dynamical systems research.

8.4 Aerodynamic Modeling: Where Are We Now?

With respect to aerodynamic modeling, it seems that many of the major mechanisms have been outlined and included in models. There are, of course, other interesting effects not included in current models. Wing flexibility would appear to be the next frontier, though it is unclear how important it is in insect flight aerodynamics. In addition, issues of wing-wake and wing-wing interference have not been incorporated in reduced-order models, though the importance of these effects is also unclear. If wing shape, and not just wing area, is important, this would also have to be investigated.

In pursuing the next generation of aerodynamic models, it is important to bear in mind the lesson from the last generation: do not start by calibrating or validating models with animal experiments. First use dynamically-scaled experiments or computational simulations to isolate major effects and build models. Then test the models against observations of actual animals.

It is also unfortunate that there is not an infrastructure for comparing different aerodynamic simulations and models. The quality of new codes could be tested by having a benchmark set of high-precision wing kinematics taken from animal experiments. How well does a code predict the forces and torques or the resulting body motion?

Once an aerodynamic model is validated, the next step is to incorporate this into a comprehensive, modular, accessible code for insect flight simulations.

There are currently several versions of such codes, and work in the Wang group is aimed at formulating such a computational tool. The immediate power of these simulators will be in testing reduced-order physical and behavioral models. Less obviously, these simulations could generate new hypotheses if different aspects of flight are explored in simulation. The aerodynamic effect of beetle elytra (the hardened wing covers), for example, could be quickly investigated in such a framework.

8.5 What Good are Reduced-Order Models?

Given that comprehensive flight simulators are emerging, what is the use of reduced-order mathematical models of flight dynamics and behavior?

First, simple models are powerful. They strip away details and allow the modeler to include only factors that are believed to be relevant. In this way, we are forced to isolate only the most important effects and are thus able to see how broadly our results apply. Comprehensive simulations include many effects and thus do not allow us to readily distinguish important ones from details. Of course, simulations do afford this capability, though the user has to systematically turn on or off different effects and evaluate their influences.

It may also be that simple models work well because they reflect a deeper truth about how animals actually operate. It is difficult to believe that the fly has evolved a sophisticated optimal nonlinear controller to stabilize flight. It seems reasonable that it has evolved a simple, fast controller that is good enough to get the job done.

Perhaps more importantly, I do not think simulations and experiments are yet accurate enough to make discoveries directly from data taken from animal studies. The basic problem is that the difference between hovering in place and turning rapidly, for example, amounts to less than 10% differences in wing forces. Now, consider all the sources of error. Even the best kinematic data typically has errors of a few percent in wing orientation angles, say. Morphological parameters are fraught with error. Wing area might be estimated to a few percent. Body mass estimates, however, cannot be made to better than 10%. (I have found that mass decreases by 5-10% over the course of an hour-long experiment!) Simulation errors are also expected to be about 10%. These are some known errors, and in light of the many unknown errors such as wing flexibility, the problem appears daunting.

The technique we have subconsciously developed to sidestep these issues involves forming simple models. We observe actual data and try to map the complicated events onto simplified or idealized pictures that capture much of the essence of what's going on. Complex wing motions can be mapped onto paddling during turns, for example. The idealized picture then must be shown to capture some important and general features of the behavior. For turns, we made a general prediction that connected body turn angle to paddling wing motions and showed that many instances could be united by this picture.

We note that other researchers interested in quantitative descriptions of animal behavior have independently converged to this same approach. In particular, Robert Full calls the approach "templates and anchors" in his work on walking and running of insects [4]. Templates are the idealized simple models of physical or biological aspects of locomotion, and such templates are anchored

in actual observation of animal behavior. From my personal experience in insect flight, I believe this approach will continue to be the driving force for discovery in the foreseeable future.

8.6 Can We Build It?

Do we know enough about insect flight to build a flapping-wing robot? Yes. There are currently many efforts into building such devices, including one being carried out in Hod Lipson's group here at Cornell [9]. This robot has four wings that flap back-and-forth, and stability is ensured by adding damping sails onto the robot body. Another notable effort is being conducted by Rob Wood's group at Harvard [11]. Their micro-robotic insect uses an external power source and is not yet capable of free-flight due to stability issues.

Perhaps the most successful work is being conducted as a classified DARPA-funded project by AeroVironment, Inc. I had the pleasure of visiting this company in the summer of 2010 and giving a talk on much of the work presented here. To my surprise, the team of engineers had stumbled upon many of our findings while building their flapping-wing robot. They had not quantified their findings or explained them, but they had discovered aspects such as the pitch instability by trial and error. In many ways, this was a crowning moment in my work. I was especially pleased to have found a group of people who shared my approach in terms of simple mechanisms. It was all the better that this group is the one leading the effort to realize flapping-wing flying robots.

The practical hurdles in constructing such robots are not in the subtle aerodynamic differences between fixed and flapping wings. The first hurdle is suffi-

cient force generation. This involves actuation mechanisms capable generating the wing motions, materials that are strong but light, and high-power motors that do not weigh much. For small-scale robots, the motors used to vibrate pagers and cellular phones make for a cheap and accessible option. The second hurdle is stability. Many groups are implementing passive stability by adding sails or dampers onto their aircraft. The AV robot may be the exception: it appears to use active stabilization using sensors and feedback control. The next hurdle is actuation schemes for maneuvering. How can we make light-weight actuators that modulate the wing motions?

The next question is, Should we build it? Will these small robots be good for anything? Will they be better than currently-available small helicopters? The impressive maneuvering capabilities of radio-controlled helicopters certainly set the bar high for flapping-wing robots. But it is difficult to assess whether efforts to make insect-like robots are worthwhile. The main problem is that we do not know if flapping-wing flight is better than fixed-wing flight in any sense. This brings us to the next big issue: To what problem exactly is flight the solution? What are the principles that underlie insect flight? We will address these challenging issues in the following section.

But there are reasons to build robots beyond possible uses for their flight itself. First, the lesson from AV is that trying to build the thing can lead to understanding just as trying to observe actual insects does. Second, the endeavor of conducting such an ambitious project is certain to lead to innovations even if flight is never realized. For example, small-scale actuators, light-weight sensors, and novel material processing is likely to emerge from this effort. Finally, I would like to see robots used to make scientific discoveries. For example, the

dependence of the pitch instability on damping could be tested by adding sails of varying sizes onto robots.

8.7 What Are the Principles?

As I consider this body of work all together, it is difficult to see the broad, unifying principles that have been distilled. I think this is largely because this work represents many initial forays into a complex and difficult subject. The field is simply not mature enough to have led to major guiding themes. Nonetheless, clues have emerged from this work, and I believe the next generation should approach the subject with an eye toward distilling principles.

A possible unifying theme for animal locomotion is optimality. The optimality principle says that animals have evolved the best ways to move according to some criterion or metric and subject to constraints. It is a natural principle routed in the clear fact that life adapts to its environment and better adaptations tend to stick around longer. What might insects be optimizing?

One idea we have pursued is whether insects use wing-strokes that conserve power while generating sufficient force to keep aloft. A primary difficulty is measuring or estimating the power consumed. We can certainly calculate aerodynamic power, but we do not know whether this is the primary loss for actual insects. Another difficulty is in the optimization routine itself. How do we optimize over all possible wing-strokes? The work of Berman and Wang made great strides in circumventing this issue by considering a rather broad family of strokes that could nonetheless be captured by relatively few parameters [2]. However, we note that the optimal stroke that was obtained for the fruit fly em-

ployed a significantly lower angle of attack than what is observed. But given the many modeling assumptions, it is difficult to say that this is a failure of the power optimality principle.

That flies employ a high angle of attack suggests that they may be optimizing for force production. In fact, the lift force is a maximum for angles of attack near 45 degrees, which is quite near the attack angle near mid-stroke. However, it is difficult to see how this idea would lead to further predictions, since the other basic way to increase force is to increase wing speed. Clearly, biological and physical constraints would limit this speed, though it is not clear how to quantitatively predict the nature of this constraint.

Perhaps instead flies are maximizing the change in forces that are induced by changes in wing motions. For example, by operating at an attack angle near 45 degrees, small changes in this angle lead to large changes in drag that is used to maneuver. Might this idea be generalized by considering strokes and modulations that maximize gradients in forces?

The above discussion touches on a great unknown in animal locomotion: What does maneuverability mean? Animals may be optimally maneuverable, but we do not have a solid mathematical framework for maneuverability as we do for stability, so we cannot begin to evaluate this quantitatively. Perhaps one idea is something like the concept of manipulability used in assessing the dexterity of robots. Do insects seek to attain a large variety of flight states using a small set of actuation mechanisms?

Another alternative would be to ask if insect flight is robust to the unpredictable changes that are likely to occur. Such changes might be flight distur-

bances, in which case the robustness of a control scheme would have to be evaluated. Other changes might be made to the wing morphology. For example, my preliminary results show that flies can handle large amounts of wing trauma, and indeed wing tearing and partial loss are common as flies age. Perhaps insects are robust to changes in body morphology, for example, the changes in mass distribution associated with laying eggs or feeding.

In all of these cases, it would appear one must define a metric that captures the sensitivity of some flight metric to changes in given parameters. A central difficulty in assessing whether one strategy is better than another is that such gradients will generally have different dimensions or units. For example, one might ask if big and slow wings are better than small and fast wings that generate the same lift. But size and speed have different units, so it is difficult to compare these two variables.

Another important concept may be minimality. While optimality seeks the best of possible solutions, minimality seeks solutions that are good enough. The work on neural response times needed to control the pitch instability illustrates this principle. We formulated the principle by seeking reaction times that were just fast enough to confer a good degree of stability. Minimality is probably a good guiding theme when animals are placed in extremely demanding situations by physical effects. Maintaining balance is demanding, and sensory-neural systems appear to be so strained as to drive solutions that are just fast enough to handle the physical instability.

Finally, in the end, flying insects must be solving many problems all at once. Perhaps ideas of multivariate optimization can be used to assess the importance of different criteria that are being considered.

These many challenges make the search for principles in animal locomotion an exciting one, and I eagerly await the discoveries on the horizon.

BIBLIOGRAPHY

[1] A. J. Bergou, L. Ristroph, J. Guckenheimer, Z. J. Wang, and I. Cohen. Fruit flies modulate passive wing pitching to generate in-flight turns. *Phys. Rev. Lett.*, 104:148101, 2010.

[2] G. J. Berman and Z. J. Wang. Energy minimizing kinematics in hovering insect flight. *J. Fluid. Mech.*, 582:153 –168, 2007.

[3] I. Faruque and J. S. Humbert. Dipteran insect flight dynamics. part 2: Lateral-directional motion about hover. *J. Theor. Biol.*, 265:306–313, 2010.

[4] R. J. Full and D. E. Koditschek. Templates and anchors: neuromechanical hypotheses of legged locomotion on land. *J. Exp. Biol.*, 202:3325–3332, 1999.

[5] J. W. S. Pringle. The gyroscopic mechanism of the halteres of diptera. *Phil. Trans. R. Soc. Lond. B*, 233:347–384, 1948.

[6] L. Ristroph, A. J. Bergou, G. Ristroph, K. Coumes, G. J. Berman, J. Guckenheimer, Z. J. Wang, and I. Cohen. Discovering the flight autostabilizer of fruit flies by inducing aerial stumbles. *PNAS*, 107:4820, 2010.

[7] L. Ristroph, G. J. Berman, A. J. Bergou, Z. J. Wang, and I. Cohen. Automated hull reconstruction motion tracking (hrmt) applied to sideways maneuvers of free-flying insects. *J. Exp. Biol.*, 212:1324–1335, 2009.

[8] G. K. Taylor. Mechanics and aerodynamics of insect flight control. *Biol. Rev.*, 76:449–471, 2001.

[9] F. van Breugel, W. Regan, and H. Lipson. From insects to machines: A passively stable, untethered flapping-hovering micro air vehicle. *IEEE Robotics and Automation Magazine*, 15:68–74, 2008.

[10] T. Weis-Fogh. Quick estimates of flight fitness in hovering animals, including novel mechanisms for lift production. *J. Exp. Biol.*, 59:169–230, 1975.

[11] R. J. Wood. First take-off of a biologically-inspired at-scale robotic insect. *IEEE Trans. on Robotics*, 24:341–347, 2008.

[12] J. M. Zanker and K. G. Goetz. The wingbeat of drosophila ii. dynamics. *Phil. Trans. R. Soc. Lond. B*, 327:19–44, 1990.